Advances in Fast MRI Experiments

Dissertation zur Erlangung des
naturwissenschaftlichen Doktorgrades
der Julius-Maximilians-Universität Würzburg

vorgelegt von
Daniel Neumann
aus Freiburg im Breisgau

Würzburg, 2014

EINGEREICHT AM: 12. Februar 2014

BEI DER FAKULTÄT FÜR PHYSIK UND ASTRONOMIE

1. GUTACHTER: Prof. Dr. Peter M. Jakob

2. GUTACHTER: Prof. Dr. Jens Pflaum

3. GUTACHTER:

DER DISSERTATION

VORSITZENDE(R):

1. PRÜFER: Prof. Dr. Peter M. Jakob

2. PRÜFER: Prof. Dr. Jens Pflaum

3. PRÜFER:

IM PROMOTIONSKOLLOQUIUM

TAG DES PROMOTIONSKOLLOQUIUMS:

DOKTORURKUNDE AUSGEHÄNDIGT AM:

ADVANCES IN FAST MRI EXPERIMENTS

Contents

CHAPTER 1

Introduction

Since its introduction in the 1970s by Lauterbur and Mansfield [1], Magnetic Resonance Imaging (MRI) has become a central diagnostic tool in clinical practice across the globe. MRI is a highly flexible technology, that can be used for a large variety of different applications. A list of prominent examples includes the location and classification of tumors, diagnosis after sports injuries, MR angiography, MR flow and diffusion experiments and functional neurological scans. In clinical routine, a number of other imaging methods such as Computer Tomography, X-rays and Ultrasound are used. A major advantage of MRI is the lack of ionizing radiation, which makes it very safe even for repeated use. Furthermore, MRI exhibits an excellent soft-tissue contrast. For some applications, such as for example the quantification of flow and diffusion, MRI provides the only option to obtain diagnostic information. A drawback of MRI however are a long duration of experiments and high costs.

Therefore, acquisition time has played and still plays one of the most important roles for the routinely application of MRI. For patients, especially when suffering from claustrophobia, it is uncomfortable if not impossible to keep still for a prolonged duration in the limited space provided by the MRI magnets. Therefore, a significant reduction of measurement time can lead to a likewise significant increase in patient comfort. Moreover, due to the high cost of both MRI machines and equipment, scan time itself is valuable. Accelerating acquisitions leads to a better time-efficiency and hence to reduced costs of MRI exams. This may allow the use of MRI exams in cases where today the cost is still prohibitively high and other methods using ionizing radiation are used instead. Last, reducing acquisition time makes new applications accessible with MRI, that require a certain temporal resolution (such as for example dynamic processes).

After the introduction of MRI, a reduction of measurement time has for a long time been achieved by mainly improving the acquisition itself with developments in both software and hardware. A major breakthrough were the introduction of fast gradient-echo based (FLASH, [2]) and spin-echo based (TSE, [3]) sequences, that acquire fully sampled images in a fraction of the time previously needed and hence first allowed routine clinical in vivo acquisitions.

Further progress could be accomplished through the development of stronger and faster gradients. In conventional Cartesian acquisitions, they can be employed to decrease acquisition time and/or improve resolution. Additionally, improved gradients paved the way to the development of fast non-Cartesian sampling schemes, where data samples are not acquired on a Cartesian grid but at arbitrary locations. Prominent examples include spiral sampling, which is highly efficient, and radial sampling, which is especially useful in dynamic imaging.

However, there are different obstacles prohibiting or at least slowing down further advances in this direction. First, improved gradients are difficult to engineer, they need more electric power and different components and consequently increase the cost of scanners overall. Second, and more importantly, physiological limits concerning stimulations of the nervous system by the use of fast switching gradients are already reached today when applying fast sequences on clinical scanners.

An alternative approach for reduced measurement time is to acquire less data than conventionally necessary for a fully sampled image and to compute missing samples in a post-processing step. In general, there are two fundamentally different ways to achieve this. One possibility known as parallel imaging is to use additional spatial information provided by receiver arrays consisting of multiple coils that are arranged around the object and independently and simultaneously acquire the signal. Parallel imaging experienced its breakthrough in the late 1990s with the introduction of SMASH [4]. Today, the two most prominent parallel imaging methods that are used on a daily basis in clinical routine are GRAPPA [5] and SENSE [6]. A second approach to reconstructing missing data in a post-processing step is to exploit prior knowledge about the data. This prior knowledge can be either extracted from (usually low-resolution) training data or consists of known properties of the object to be measured. An important constrained reconstruction method that was introduced to MRI in 2007 and since then has enjoyed an ever growing popularity is compressed sensing [7]. In contrast to parallel imaging, the success of a compressed sensing reconstruction greatly depends on the properties of the object to be measured. Compressed sensing allows the reconstruction of aliasing-free images from incomplete data sets only for objects, that exhibit a high level of sparsity. An image is sparse, when only a small subset of all available image pixels exhibit values other than zero. For CS, sparsity doesn't have to be fulfilled directly in image space but in any space that can be reached via an invertible transform. As many MR images exhibit sparsity in some domain, CS is very promising to achieve further acceleration of acquisitions.

In this work, new opportunities were investigated to increase the effectiveness of MRI acquisitions by both improving and developing new reconstruction methods. Chapter 2 and 3 provide a short review of magnetic resonance imaging and introduce the most important methods and principles used in this thesis. In Chapter 4, a new combined radial TSE acquisition and reconstruction method is introduced, that generates several images exhibiting different contrast from a single data set. To reduce unwanted contrast contributions, that are usually present in Cartesian and radial TSE images, data sharing between contrasts is restricted to a small temporal window and parallel imaging is employed to remove resulting aliasing artifacts. Besides the generation of images with a specific contrast, fast spin-echo sequences are used in clinical routine for the quantification of the important tissue parameters T_2 and proton density, since the more accurate single spin-echo method is not feasible due to long acquisition times. Because of technical imperfections, in most cases significant deviations of T_2 from its accurate value occur. In Chapter 5, an auto-calibrating method is introduced to obtain accurate T_2 estimates from multi spin-echo experiments. In Chapter 6, a new parallel imaging method called iterative GROG is presented. Iterative GROG allows the reconstruction of non-Cartesian data without calibration data, which is necessary in many conventional parallel imaging methods. Finally, Chapter 7 introduces a new efficient and incoherent 2D sampling scheme that promises improved compressed sensing reconstructions. In conventional 2D sampling techniques the incoherency recquired for successful CS reconstructions is difficult to achieve.

CHAPTER 2

Basic Principles of MRI

In this chapter some of the basic principles of Magnetic Resonance Imaging (MRI) are discussed. Starting at the generation of a measurable signal, it introduces the important k-space formulation and some selected data acquisition strategies. It is by no means complete and is merely supposed to give a quick introduction to the most important principles used in this work. Comprehensive treatments of MRI can for example be found in text books by Haacke [8] or Bernstein [9].

2.1 Origin of the MR signal

Magnetic Resonance manipulates the nuclear spin of particles to generate a signal, that can be measured to extract information about either the composition (MR spectroscopy) or the spatial distribution (MR Imaging) of a substance. The spin $\hat{\boldsymbol{S}}$ is an intrinsic angular momentum of elementary particles. Its origin can only be explained in the framework of a relativistic quantum field theory. However, the properties of spins necessary for the understanding of MRI can be fully explained by non-relativistic quantum mechanics. A comprehensive treatment can be found in most standard textbooks about quantum mechanics, e.g. [10].

Each spin has a corresponding magnetic moment $\hat{\boldsymbol{\mu}} = \gamma\hat{\boldsymbol{S}}$. The gyromagnetic ratio γ assumes different values which depend on the element at hand. In MRI, the most commonly used nuclei is ${}^{1}H$ due to its abundance in the human body. While other nuclei such as carbon ${}^{13}C$ and sodium have been investigated in MR Imaging, in this work images are obtained from protons exclusively and the following discussion accordingly disregards other particles. For protons, the value of the gyromagnetic ratio is $\gamma = 2,68 \cdot 10^8 \,/(\mathrm{sT})$. In an external magnetic field $\boldsymbol{B}$, the Hamiltonian is given by

$$\hat{H} = -\hat{\boldsymbol{\mu}} \cdot \boldsymbol{B} = -\gamma\, \hat{\boldsymbol{S}} \cdot \boldsymbol{B}. \tag{2.1}$$

Typically, the coordinate system is chosen such that $\boldsymbol{B} = B_0 \cdot \boldsymbol{e}_z$ is aligned with the z-axis. The system of eigenvectors for this equation is characterized by the quantum numbers (s, m_s) with values for protons of $s = 1/2$ and $m_s = \pm 1/2$. The associated eigenvalues are $E_\pm = \pm\gamma\frac{\hbar}{2}B_0$. Any arbitrary spin state can be expressed as a linear superposition of the eigenstates to the Hamiltonian. The stationary Schrödinger equation yields the temporal evolution of the expectation values of the transversal spin components

$$\begin{aligned} \langle \hat{S}_x \rangle &= \frac{\hbar}{2}\cos(\omega_L t + \varphi) \\ \langle \hat{S}_y \rangle &= \frac{\hbar}{2}\sin(\omega_L t + \varphi). \end{aligned} \tag{2.2}$$

Hence, the transversal expectation value of the spin precesses with the Larmor-frequency $\omega_L = \omega_0 = \gamma B_0$ around the external magnetic field. This effect is known as Larmor precession and forms the basis for all MR experiments.

To this date, it is not possible to track the temporal evolution of single spins using MR. Instead, information is obtained about large numbers of spins simultaneously. In a large pool of spins in thermal equilibrium without the presence of an external magnetic field, an isotropic distribution of all possible spin states can be observed. Looking at the direction of the spins in three dimensions, the tips of all spins are isotropically distributed on the surface of a sphere. Therefore, no resulting net magnetization emerges. Introducing an external magnetic field marks a preferred direction with a lower energy for the system of spins. While the difference in energy is small compared to the thermal energy, it does result in a small change of the distribution with more spins pointing towards the direction of the magnetic field. The resulting net magnetization at the temperature T is given by

$$M_0 = \frac{\rho_0 \gamma^2 \hbar^2}{4kT} B_0, \tag{2.3}$$

where ρ_0 is the spin density and k the Boltzmann constant. The typically large value ρ_0 for protons in the human body yields a macroscopic net magnetization that can be manipulated and measured in MR experiments. Furthermore, the linear dependence of the net magnetization M_0 on the strength of the magnetic field B_0 combined with the small value for the gyromagnetic ratio explains the need for strong magnets in MRI.

2.1.1 Magnetic Resonance

Due to the underlying spin dynamics, in an external magnetic field the magnetization $\boldsymbol{M} = \sum \boldsymbol{\mu}$ also experiences a Larmor precession according to

$$\frac{\mathrm{d}\boldsymbol{M}}{\mathrm{d}t} = \gamma \boldsymbol{M} \times \boldsymbol{B}_0. \tag{2.4}$$

This is exploited by MR experiments to generate a measurable signal. The combined magnetization of a large number of spins precessing in an external magnetic field can be detected via induction in a receiver coil. In thermal equilibrium however, the magnetization is aligned along $\boldsymbol{B}_0$ and no precession takes place. To obtain a signal, $\boldsymbol{M}$ therefore has to be rotated (at least partially) into the transversal plane. In order to describe this process and for the following considerations it is helpful to introduce a reference frame rotating with the Larmor frequency $\omega_0 = \gamma B_0$ around the axis given by $\boldsymbol{B}_0$. Without the presence of additional magnetic fields (besides $\boldsymbol{B}_0$), in this frame the magnetization remains constant over time as the frame rotates with the same angular velocity as the magnetization.

In the rotating frame, adding a magnetic field $\boldsymbol{B}_1 = B_1 \boldsymbol{e}_T$ along a fixed direction in the transversal plane leads to an additional precession of $\boldsymbol{M}$ around $\boldsymbol{e}_T$ with the angular frequency $\omega = \gamma B_1$. If $\boldsymbol{B}_1$ is applied for a specific duration, this precession rotates $\boldsymbol{M}$ into the transversal plane. In the standard reference frame

$$\boldsymbol{B}_1(t) = B_1 \left(\cos(\omega_0 t)\, \boldsymbol{e}_x + \sin(\omega_0 t)\, \boldsymbol{e}_y\right) \tag{2.5}$$

corresponds to an electro-magnetic pulse with frequency ω_0. At typical values for the main magnetic field, ω_0 is situated in the radio frequency (RF) range. The angle

$$\alpha = \int_{t_0}^{t_1} \mathrm{d}t\, \gamma \cdot |\boldsymbol{B}_1|. \tag{2.6}$$

by which the magnetization is rotated by the RF-pulse is known as flip angle. To simplify calculations, in the following the transversal magnetization $\boldsymbol{M}_T = M_x \boldsymbol{e}_x + M_y \boldsymbol{e}_y$ is described by the complex value

$$M_T = M_x + iM_y, \tag{2.7}$$

so that the direction of the magnetization is given by the phase of M_T.

2.1.2 Relaxation and Bloch equation

For a full understanding of MR, relaxation effects have to be taken into account. Relaxation describes the temporal evolution of the magnetization to its thermal equilibrium after its displacement by one or several RF-pulses. Two different mechanisms contribute to relaxation.

> The recovery of longitudinal magnetization is known as **spin-lattice–relaxation** and characterized by the time constant T_1. A RF-pulse that rotates $\boldsymbol{M}$ away from the z-axis adds energy to the system of spins. By exchanging energy with the surrounding lattice, the spins relax to the equilibrium until the full longitudinal magnetization is recovered. The rate is hereby proportional to the difference between $M_z(t)$ and M_0.
>
> $$\frac{\mathrm{d}M_z(t)}{\mathrm{d}t} = \frac{1}{T_1}(M_0 - M_z(t)). \tag{2.8}$$

A solution to this equation is given by

$$M_z(t) = M_0 - (M_0 - M_z(0))\exp(\frac{t}{T_1}) \tag{2.9}$$

The time constant T_1 depends on the element and the properties of the surrounding matter and assumes different values depending on the tissue type in the human body.

The **spin-spin–relaxation** is the main reason for the decay of the transversal magnetization after excitation by the RF pulse. It is caused by local inhomogeneities of the main magnetic field B_0. In general, $B_0(\boldsymbol{x})$ is a superposition of both the field generated by the magnet and a magnetic field component connected to the magnetic moment of surrounding spin. The contributions by neighbouring spins leads to a spatial (and temporal due to Brownian motion) variation of B_0, so that the magnetization at different locations precesses with different angular velocities. This causes a growing phase decoherence of the spin ensemble and therefore a decrease of the transversal component of the net magnetization:

$$\frac{\mathrm{d}M_T}{\mathrm{d}t} = \frac{1}{T_2}M_T. \tag{2.10}$$

The temporal evolution of M_T is consequently given by the exponential decay

$$M_T(t) = M_T(0)\exp(-t/T_2) \tag{2.11}$$

with the time constant T_2.

Additionally, the main magnetic field itself exhibits inherent imperfections and contributions from tissues with different susceptibilities χ. This leads to an accelerated decoherence, which reduces the time constant in Eq. (2.10) to a smaller value $T_2^* < T_2$. This distinction is necessary, because some acquisition schemes manage to correct for the inherent inhomogeneities of $B_0(\boldsymbol{x})$ so that the signal decays with T_2.

Incorporating all different aspects, the temporal evolution of magnetization can be described by the Bloch equation, the central equation of MRI

$$\frac{\mathrm{d}\boldsymbol{M}}{\mathrm{d}t} = \gamma\boldsymbol{M}\times\boldsymbol{B} + \frac{1}{T_1}(M_0 - M_z)\boldsymbol{e}_z - \frac{1}{T_2}\boldsymbol{M}_T \tag{2.12}$$

with $\boldsymbol{B}(t) = \boldsymbol{B}_0 + \boldsymbol{B}_1(t)$.

2.2 MR Imaging

After excitation, an oscillating signal can be detected that drops off exponentially with the time constant T_2^* as discussed above. This so-called Free Induction Decay (FID) yields information about the total number of protons present in the whole sample.

For an intuitive understanding of MR Imaging, consider a linear distribution of protons as shown in Fig. 2.1. A Fourier transform of the temporal signal after excitation shows a single central peak at the Larmor frequency. To obtain information about the distribution of protons, a spatial dependency $\omega(x)$ of the Larmor frequency is required. This can be achieved by introducing a gradient field

$$G(x) = \frac{\partial |B(x)\boldsymbol{e}_z|}{\partial x} \neq 0. \tag{2.13}$$

Very common in MR are constant gradient fields $G(x) = G$, that modify the magnetic field to

$$\boldsymbol{B}(x) = \boldsymbol{B}_0 + G \cdot x \; \boldsymbol{e}_z \tag{2.14}$$

The impact of a constant gradient on the spectrum is shown on the right hand side of Fig. 2.1. The Larmor frequency of the magnetization depends on their location and a Fourier transform of the temporal signal yields the spatial distribution.

This concept can easily be extended to a multi-dimensional space. In general, the gradient vector is given by $\boldsymbol{G} = \nabla |B(\boldsymbol{x})|$. The corresponding spatially dependent magnetic field then computes to

$$\boldsymbol{B}(\boldsymbol{r}) = \boldsymbol{B}_0 + \int \boldsymbol{G}(\boldsymbol{r}) \cdot \mathrm{d}\boldsymbol{r} = \boldsymbol{B}_0 + \boldsymbol{G}(\boldsymbol{r}) \cdot \boldsymbol{r} \tag{2.15}$$

for constant gradients. After acquiring a full set of data as discussed below, a multi-dimensional Fourier transform yields an image. The connection between the gradient vector and the temporal signal can be explained in an elegant way using the k-space formulation.

2.2.1 k-Space formulation

Solving the Bloch equations (2.12) in the presence of constant magnetic field gradients and neglecting the influence of relaxation yields the signal evolution

$$S(t) = \int \mathrm{d}^N\boldsymbol{r} \; m(\boldsymbol{r}) \exp\left(-i\gamma \int dt' \boldsymbol{G}(t') \cdot \boldsymbol{r}\right) \tag{2.16}$$

for the transversal component of the magnetization. Hereby, $m(\boldsymbol{r})$ is the distribution of transversal magnetization in the N-dimensional space, which is directly proportional to the spin density. The gradient field causes a spatially varying Larmor frequency. This in turn leads to a phase offset of magnetization at different locations that depends linearly on the total magnetic moment. Introducing $\boldsymbol{k} = \gamma \int dt \; \boldsymbol{G}(t)$, the signal

$$S(\boldsymbol{k}) = \int \mathrm{d}^N\boldsymbol{r} \; m(\boldsymbol{r}) e^{-i\boldsymbol{k}\cdot\boldsymbol{r}} \tag{2.17}$$

is the Fourier transform of the spin density. The inverse operation yields the desired information about the spatial distribution of the spin density:

$$m(\boldsymbol{r}) = \frac{1}{2\pi} \int \mathrm{d}^N\boldsymbol{k} \; S(\boldsymbol{k}) e^{i\boldsymbol{k}\cdot\boldsymbol{r}} \tag{2.18}$$

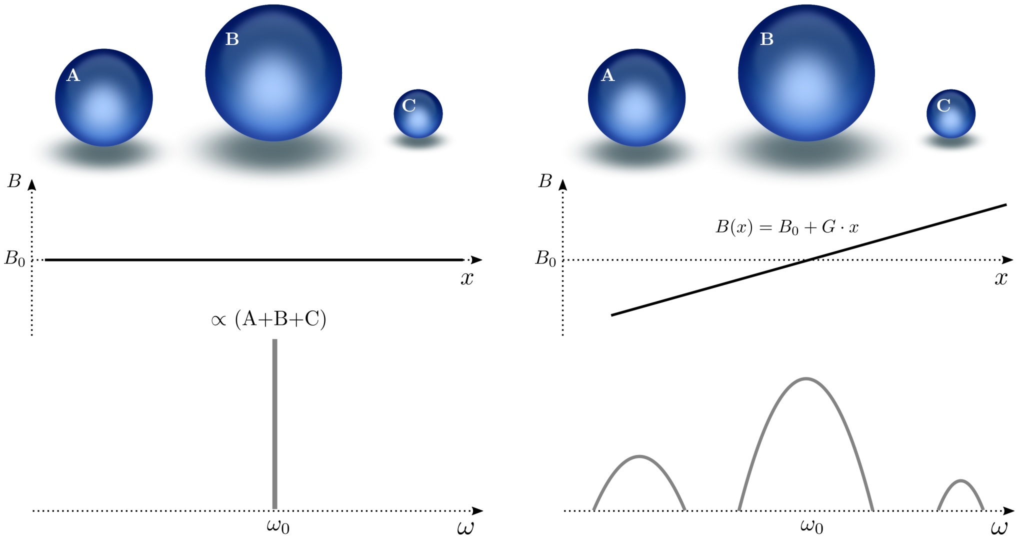

Figure 2.1: Imaging of three spin pools of different net magnetization. Left: Since the magnetic field is constant, after excitation all spins precess at the same frequency ω_0. The Fourier transform of the temporal signal shown at the bottom exhibits a peak at the central frequency proportional to the sum of all magnetization. Right: A linear gradient introduces a spatially varying magnetic field. As consequence, the spins precess at different Larmor frequencies. Now, a Fourier transform yields spatially resolved information.

Therefore, to obtain spatial information about an object, data at all necessary values of the coordinate $\boldsymbol{k}$ have to be acquired. The vector $\boldsymbol{k}$ has the same physical units as a wave number and gives k-space its name. Due to hardware restrictions, the signal can be sampled neither continuously nor at arbitrarily high values of $|\boldsymbol{k}|$. Instead, data at discrete locations $\boldsymbol{k}$ are acquired. This restricts the possible values for the resolution and the field of view (FOV) of the resulting image, which is discussed in detail in the next section.

In clinical routine, most often the absolute value of $m(\boldsymbol{r})$ is depicted. However, in some methods the phase of the signal carries important information, for example in flow MRI [11].

2.2.2 Spatial resolution and field of view

The desired spatial resolution and the FOV of a measurement determines the specific discretization of k-space and which points need to be acquired in a measurement. The mathematical relations can be deduced from the properties of the discrete Fourier transform. To facilitate notation, the following observations are restricted to one dimension.

Considering a set of complex data points $\{d_K\}$ of size N, the discrete Fourier transform DFT is defined as

$$\mathrm{DFT}[\{d\}]_J = D_J = \sum_{K=0}^{N-1} d_K \exp\left(-i \cdot \frac{JK}{N}\right), \quad J = 0, 1, \cdots, N-1 \tag{2.19}$$

The inverse operation is then given by

$$\mathrm{DFT}^{-1}[\{D\}]_K = d_K = \frac{1}{2\pi N} \sum_{J=0}^{N-1} D_J \exp\left(i \cdot \frac{JK}{N}\right) \tag{2.20}$$

Introducing the quantized physical quantities $x_K = K \cdot \Delta x$ and $k_J = J \cdot \Delta k$ with finite values for both x and k, Eq. (2.18) can be rewritten as

$$m(K \cdot \Delta x) = \frac{1}{2\pi N} \sum_{J=0}^{N-1} S(J \cdot \Delta k) \exp(i \cdot JK(\Delta x \Delta k)) \tag{2.21}$$

Comparing this to the definition of the discrete Fourier transform yields

$$\Delta x \cdot \Delta k = \frac{1}{N}. \tag{2.22}$$

From this equation, two important conclusions can be made. Looking at the smallest distance between two points in image space

$$\Delta x = \frac{1}{N \cdot \Delta k} = \frac{1}{k_{\text{max}}}, \tag{2.23}$$

it follows, that the resolution is inverse the maximum value of k. In order to achieve higher resolution (= smaller Δx), larger values for k and accordingly larger gradient moments $\int \mathrm{d}t\, G(t)$ are required. Hence, the achievable resolution is mainly restricted by the gradient strength provided by the scanner and the desired total acquisition time. Secondly, the size of the field of view

$$\mathrm{FOV} = N \cdot \Delta x = \frac{1}{\Delta k} \tag{2.24}$$

in turn is defined by the value for the increment of k. This means that Δk has to be reduced in order to increase the field of view. In summary, increasing both the spatial resolution and the field of view results in more required data points and therefore lead to longer acquisition times.

2.2.3 Image contrast

The discussed relations allow a few important conclusions, that are illustrated in Figure 2.2. Consider the k-space of a high-resolution image shown on top. Thanks to the linearity of the Fourier Transform, the whole image is the sum of a low-resolution image containing the contrast information (corresponding to the information in the k-space center) and the high-resolution details (outer k-space). Which data to chose for the center and the edges of k-space is an important considerations in a large number of MRI experiments and reconstruction algorithms and is discussed later in this work.

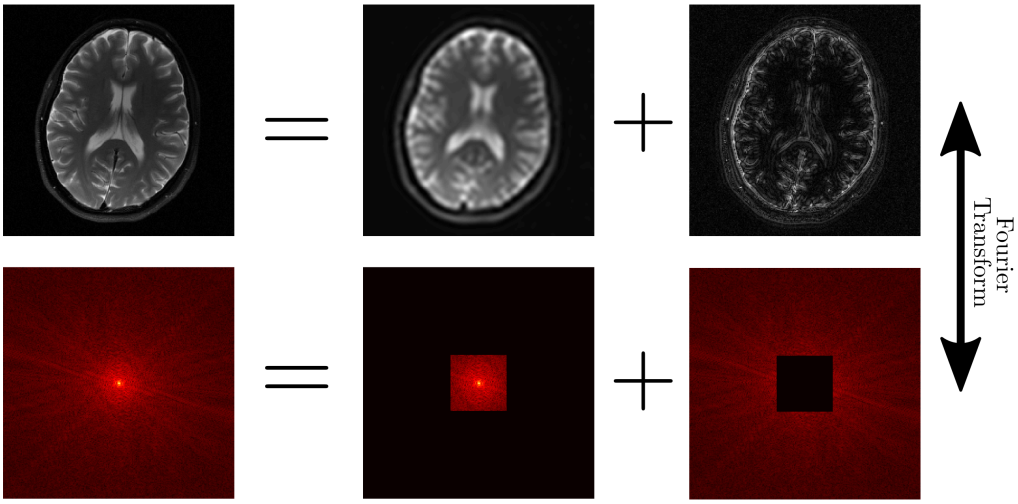

Figure 2.2: Information content of low and high frequency data in k-space. While the contrast of an image mainly depends on the data located in the center of k-space, the resolution is defined by outer k-space.

2.2.4 RF-pulses and slice selection

In MRI, the excitation of the magnetization from the thermodynamic equilibrium to the transversal plane can be achieved by the irradiation of RF-pulses at the Larmor frequency

$$B_1(t) = \hat{B}_1 e^{i\omega_0 t}. \tag{2.25}$$

To achieve a homogeneous excitation across the whole sample, a pulse with a constant amplitude $\hat{B}_1$ over a short duration T_p can be applied. With a corresponding Larmor frequency $\omega_{RF} = \gamma \hat{B}_1$, the total flip angle of this rectangular pulse computes to

$$\alpha = \int_0^{T_p} \mathrm{d}t\, \gamma \hat{B}_1 = \gamma \hat{B}_1 \cdot T_p. \tag{2.26}$$

In many cases in clinical practice, information about a two-dimensional slice in a specific orientation and location is needed. To prevent signal contributions from unwanted locations, the excitation of the RF-pulse therefore has to be localized. This can be achieved by two main steps:

1. Introduction of a field gradient in slice direction. This leads to a spatially varying precession frequency of magnetization depending on their location on the z-axis.
2. When the gradient is active, excitation of a specific slice can be obtained by a pulse with a rectangular profile $\alpha(\omega)$ in frequency space. Now, only magnetization with Larmor frequencies equal to $\omega \mid \alpha(\omega) \neq 0$ are affected by the pulse. The frequency profile of a RF-pulse can be adjusted by manipulating its temporal envelope (left of Fig. 2.2).

For the derivation of the required temporal pulse profile, relaxation effects will be neglected. This approach is accurate due to the short duration of the RF-pulses compared to the typical relaxation times T_1 and T_2. A comprehensive description can be found in [12]. In the rotating reference frame, the combined magnetic field from both constant gradient- and the RF-pulse aligned with an arbitrary axis in the transversal plane is given by

$$\boldsymbol{B}(t) = G_z z \cdot \boldsymbol{e}_z + \hat{B}_1(t) \cdot \boldsymbol{e}_T \tag{2.27}$$

Now, the Bloch equation in complex notation for the transversal part of the magnetization reads

$$\frac{\mathrm{d}M_T}{\mathrm{d}t} = -i\gamma G_z z M_T + i\gamma \hat{B}_1(t) M_z, \tag{2.28}$$

which corresponds to a Larmor precession of the transversal magnetization due to the gradient field and a rotation of longitudinal magnetization into the transversal plane due to B_1. A simple solution can be obtained for small values of the flip angle α, where the relation $M_z = M_0 \cdot \cos(\alpha) \approx M_0$ holds. Assuming a constant gradient G_z for the duration of the pulse and with the initial condition $M_T = 0$ at $t = 0$, the solution of the differential equation 2.28 is given by [13]

$$M_T(T_p, z) = i\gamma M_0 e^{i\gamma G_z z T_p/2} \int_0^{T_p} \mathrm{d}t \, \hat{B}_1(t) e^{i\gamma G_z z t}. \tag{2.29}$$

Hence, the slice profile in z of the RF-pulse is given by the Fourier transform of $\hat{B}_1(t)$. The additional phase $e^{i\gamma G_z z T/2}$ imposed on the magnetization depends on its location along z and can be removed by applying a second gradient after the excitation with an opposite polarity and half the moment of the slice selection gradient. Using the inverse operation, the envelope of the RF-pulse can be determined for a given desired slice profile. For ideal excitation of a slice with a rectangular profile in frequency space, the envelope computes to

$$B_1(t) = iG_z d \cdot \mathrm{sinc}(\frac{kd}{2}) \sin\alpha. \tag{2.30}$$

Despite the approximation of a constant longitudinal component, this formula yields acceptable results even up to flip angles of $\pi/2$. For higher flip angles, the approximation fails and the differential equation can only be solved numerically. This can for example be done using the Shinnar-Le-Roux algorithm [14]. Figure 2.3 depicts the selection of a particular slice with the help of a slice selection gradient.

2.3 MR sequences

The succession of the RF-pulses and gradients necessary for the acquisition of specific data points in k-space are known as MR Sequences. There are many different acquisition techniques based on a large variety of physical principles. The choice of a specific sequence has a huge influence on many important properties of the resulting image. Depending on the sequence, different tissues in the object can be highlighted as a function of their particular values of proton density and the relaxation parameters T_1 and T_2 (or T_2^*). This is known as image contrast, which is explained in more detail below. Another important example is the signal to noise ratio (SNR). Therefore, a se-

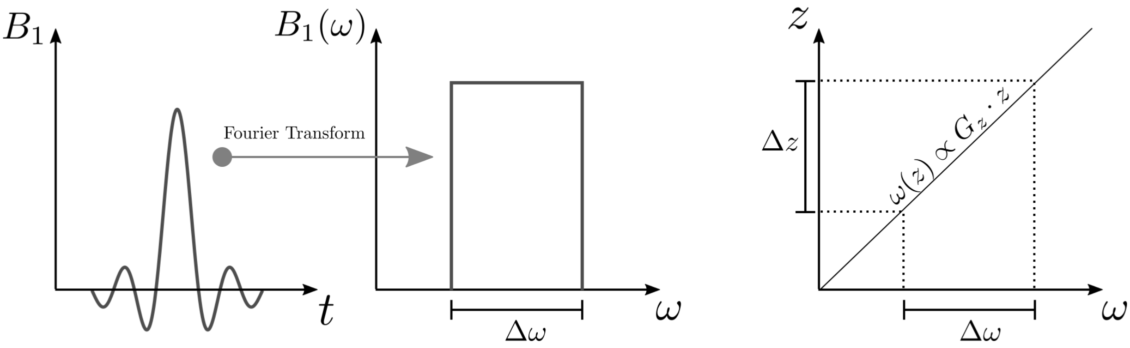

Figure 2.3: Slice selection. A RF-pulse with a temporal sinc-shaped envelope has a rectangular profile in frequency space. Applying this RF-pulse while a slice-selection gradient is active, leads to the excitation of spins located in only a small spatial region along the z-axis.

quence has to be chosen for each desired outcome keeping restrictions such as measurement time in mind. Important parameters common to all MRI sequences are the echo time TE, which is the duration between the excitation pulse and the echo, the duration between subsequent excitations (repetition time TR), the base resolution of the image and the bandwidth of the analog-to-digital converter ADC.

Today, sequences can be divided in mainly two classes according to how they generate echoes and acquire data. Figure 2.4 shows the sequence diagram of both a basic gradient echo (GRE) and a spin-echo (SE) sequence. In the gradient echo sequence (a), an excitation pulse is followed by a gradient in both read-out and phase direction, that is applied to reach the desired position in k-space. Data along a continuous line in k-space is then acquired with help of a constant gradient in read-out direction. After the repetition time TR, in which the longitudinal magnetization recovers, the next excitation follows. In GRE sequences, field inhomogeneities of B_0 due to imperfect manufacturing are not compensated for and the signal decays with T_2^*.

The spin-echo sequence [15] uses an additional RF-pulse to refocus the magnetization. With a flip angle of $180°$, this refocussing pulse inverts the direction of all magnetization with respect to the axis defined by the pulse. Compared to the gradient echo, this has the advantage of compensating for intrinsic field inhomogeneities. As result, the signal intensity decays with T_2 instead of T_2^*. Due to this compensation, SE-based sequences also deliver better results in cases with additional local inhomogeneities, caused for example by the presence of certain implants made of metal and other materials that distort the magnetic field. In both cases, a flip angle of $90°$ for the excitation pulse maximizes SNR. However, both sequences as shown in Figure 2.4 then require long repetition times TR between subsequent excitations to allow a complete recovery of the longitudinal magnetization M_0. To acquire a fully sampled dataset, this leads to infeasibly long acquisition times especially for high resolution scans.

Many different acquisition methods based on both the gradient- and the spin echo technique were proposed that mostly provide a higher efficiency and reduce measurement time significantly. A scheme first introduced by Frahm and Haase in their method called Fast Low Angle Shot (FLASH) [2] uses lower flip angles for the excitation pulse and greatly reduces the dead-time

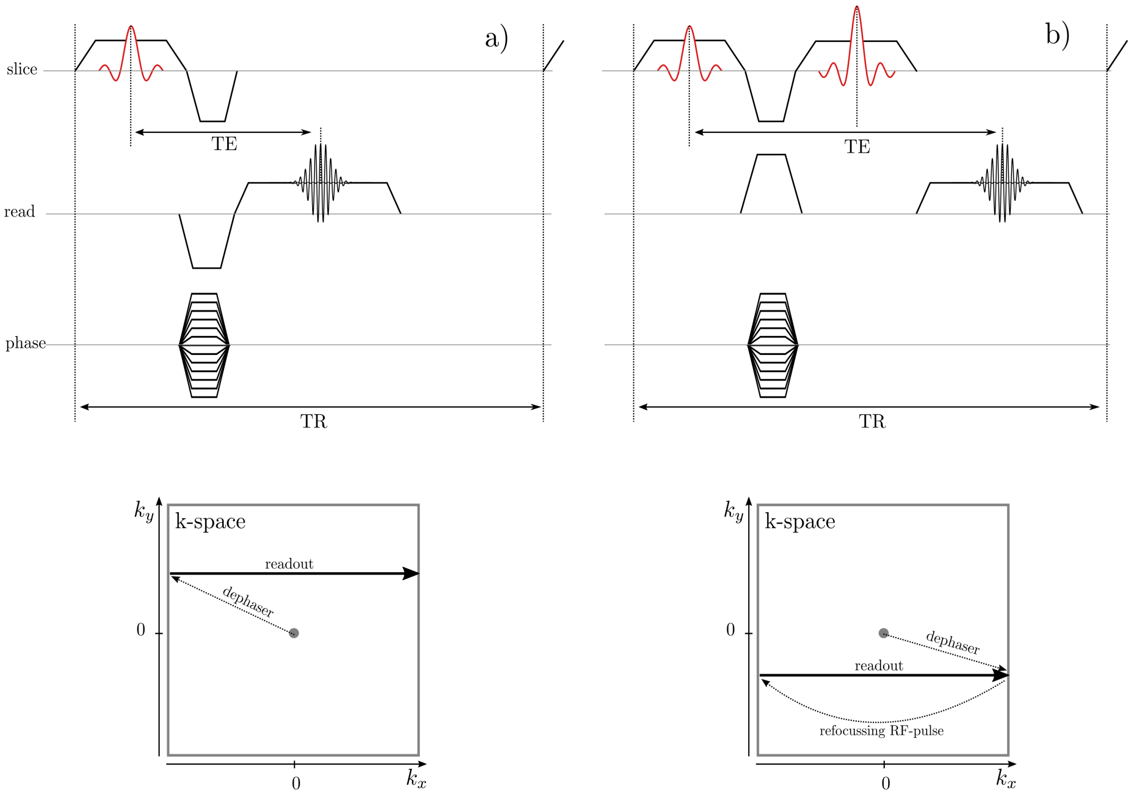

Figure 2.4: Sequence diagrams of both a basic gradient echo sequence (a) and a spin-echo sequence (b). The corresponding trajectories in k-space are depicted below.

between subsequent excitations. This results in a steady state of the longitudinal magnetization, as explained in more detail below. Similar concepts are used by balanced steady state free precession (bSSFP) sequences [16, 17]. A different approach is to utilize the dead time between excitations by generating multiple echoes from a single excitation. Echo-planar imaging (EPI, [18]) uses several read-out gradients with alternating polarities after each excitation to achieve this. The spin-echo based sequence RARE [3], also known as turbo spin-echo (TSE) or fast spin-echo (FSE) follows a similar strategy. Here, a train of refocussing RF-pulses is applied after each excitation to generate multiple echoes.

In this section, a few important basic MR-sequences, namely FLASH, bSSFP and TSE, are briefly introduced. A very comprehensive treatment of MR sequences can be found in [9].

2.3.1 Fast Low Angle SHot (FLASH)

After its introduction, FLASH quickly became a widely used sequence in clinical practice. Only few modifications to the basic GRE sequence shown in Figure 2.4 are required in order to obtain a simple FLASH sequence:

- Reduction of the flip angle α of the excitation pulse. This simple change has important implications. For small flip angles, only a small part $\sin\alpha$ of the total available magnetization aligned with the z-axis is rotated into the transversal plane. Therefore, less time is needed for full recovery of M_0 and the repetition time TR can be reduced. This comes with a price however, as less transversal magnetization leads to a lower SNR of acquired data.

- Further reduction of TR to much shorter values than necessary for a complete relaxation of the longitudinal magnetization. A steady state emerges for the longitudinal magnetization with a value $M_0^* < M_0$ that depends on the values for flip angle and TR (typically in the range of a few milliseconds) used in the experiment as well as the relaxation time T_1.

- As small values TR are used, the transversal magnetization usually is not completely decoherent at the end of each interval and has to be destroyed in order to prevent artifacts in the images. This is known as spoiling and can be achieved by two different mechanisms: Gradients spoiling uses gradients with large moments to dephase the magnetization after each readout. RF-spoiling [19–21] changes the phase (i.e. the axis in the transversal plane) of subsequent excitation pulses to prevent a unwanted coherent superposition of remaining transverse magnetization. In FLASH, both methods are usually combined.

The steady-state magnetization M_0^* on the longitudinal axis can be calculated for a FLASH sequence taking the flip angle and relaxation effects into account. Let M_z^i be the magnetization at the end of the ith readout. Using the Bloch equations, the next iteration is given by

$$M_z^{i+1} = M_z^i \cos(\alpha) e^{-\frac{TR}{T_1}} + M_0 (1 - e^{-\frac{TR}{T_1}}) \tag{2.31}$$

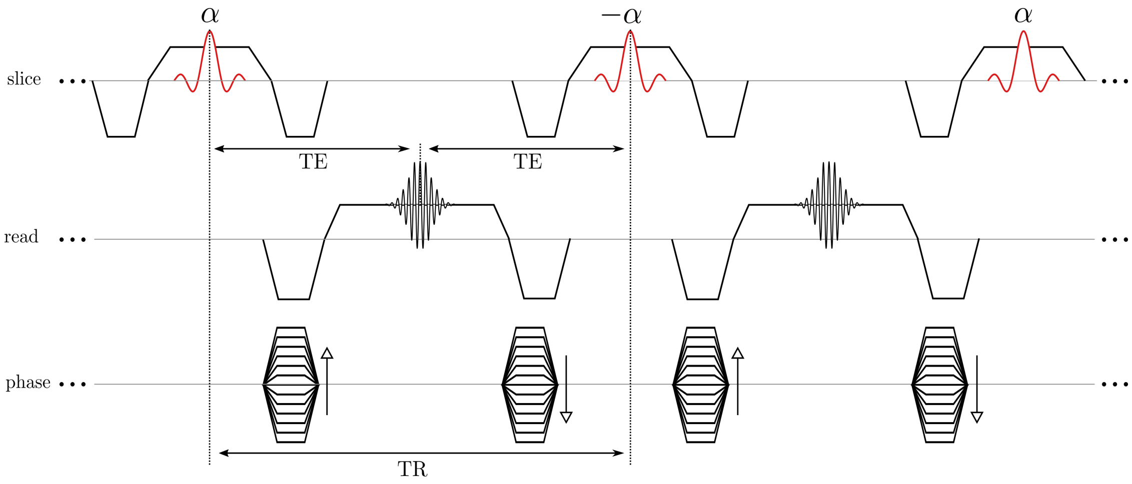

Figure 2.5: Sequence diagram of a balanced SSFP sequence. A train of RF-pulses is applied. The gradient moments are balanced in each interval between excitations. Echoes occur at TE=TR/2.

In steady state, the magnetization remains unchanged ($M_z^{i+1} == M_z^i$) and it follows

$$M_0^* = M_0 \cdot \frac{1 - e^{-\frac{TR}{T_1}}}{1 - \cos\alpha\, e^{-\frac{TR}{T_1}}}. \tag{2.32}$$

Based on this consideration, the signal intensity of a single echo in a FLASH sequence computes to

$$S_{FLASH} = M_0^* \sin\alpha\, e^{\frac{-TE}{T_2^*}}\,. \tag{2.33}$$

The flip angle maximizing this term is know as the Ernst angle and given by

$$\alpha_E = \arccos(e^{\frac{-TR}{T_1}}). \tag{2.34}$$

Similar to a simple gradient echo, the signal in a FLASH sequence decays with the time constant T_2^*. At the beginning of each measurement with $M_z(0) = M_0$, the steady state is only reached after a number of pulses, depending on both T_1 and the sequence parameters used. Therefore, in some cases so-called dummy pulses are used without data acquisition before the actual experiment.

2.3.2 balanced Steady-State Free Precession (bSSFP)

Similar to FLASH, in balanced SSPF (also known as True FISP), a series of equidistantly spaced RF-pulses is applied. The diagram of a bSSFP sequence is shown in Figure 2.5. The most important distinction of this sequence is, that all gradient moments are compensated at the end of each readout interval (i.e. $\int_0^{TR} \mathrm{d}t\, G(t) = 0$). This makes the transversal magnetization, which is used in one TR for signal acquisition, available for the next echo as well. Echoes in bSSFP

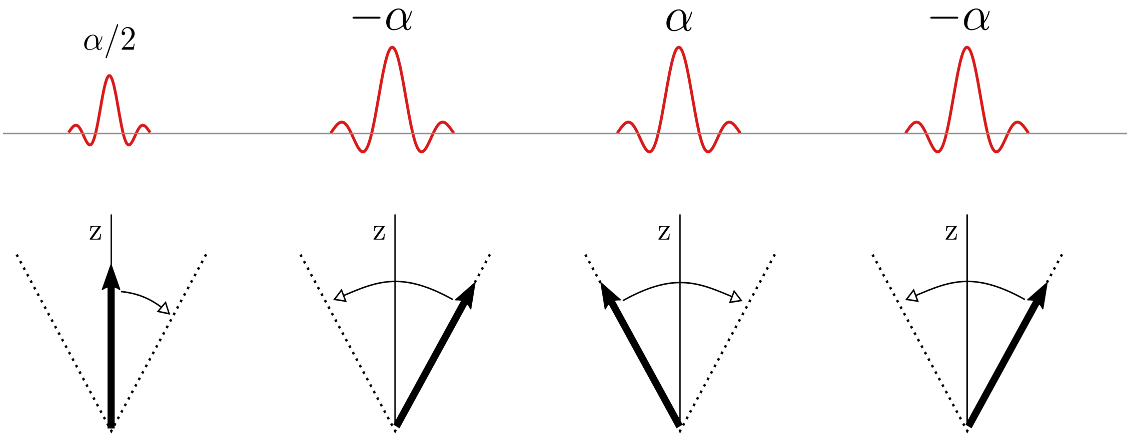

Figure 2.6: Evolution of the magnetization in a bSSFP sequence with a $\alpha/2$-preparation pulse. A 2D projection of a 3D cone with an apex angle of α is shown. The first pulse moves the preparation onto the cone. Now, each excitation pulse with a flip angle of α flips the magnetization to the opposite side of the cone. Signal encoding and data acquisition takes place in between pulses.

are typically acquired at TE = TR/2 in between excitations. In order to maintain a steady state with a high signal intensity for on-resonant spins, the phase of the RF-pulses is increased by 180° for subsequent excitations. At the beginning of the acquisition, when the steady state is not yet reached, significant oscillations of the signal intensity may occur. The fastest way to prevent those oscillations is to apply a preparation pulse with a flip angle of $\alpha/2$ before data acquisition. The corresponding evolution of the magnetization is shown in Figure 2.6.

In contrast to spoiled GRE sequences, transversal magnetization is refocussed after each echo and can be used for the generation of the subsequent echo, which results in images with a high SNR. In combination with the small required repetition times, bSSPF sequences are very efficient and are widely used in clinical practice, especially in cardiac imaging. Typically, TR is chosen as short as possible and lies in the millisecond range. In this case, TR $\ll T_2 < T_1$ holds true and the signal level is given by

$$S_{bSSPF} \approx \frac{M_0 \sin\alpha}{(T_1/T_2)(1-\cos\alpha)+1+\cos\alpha} e^{-\frac{TE}{T_2}} \tag{2.35}$$

Hence, for high flip angles close to 90°, the image contrast is approximately proportional to the ratio T_2/T_1. Consequently, water or liquids and tissues like fat with a T_1 relaxation time of the same order as T_2 often appear bright in bSSPF images.

Thanks to the balanced gradients and the short TR, bSSFP has the highest SNR per unit time of all MRI sequences. A drawback of bSSFP is its sensitivity to off-resonance, that destroys coherence of the magnetization before each RF-pulse and may lead to signal cancellation in the images. A comprehensive review of balanced SSFP is given for example in [22].

2.3.3 Turbo Spin-Echo (TSE)

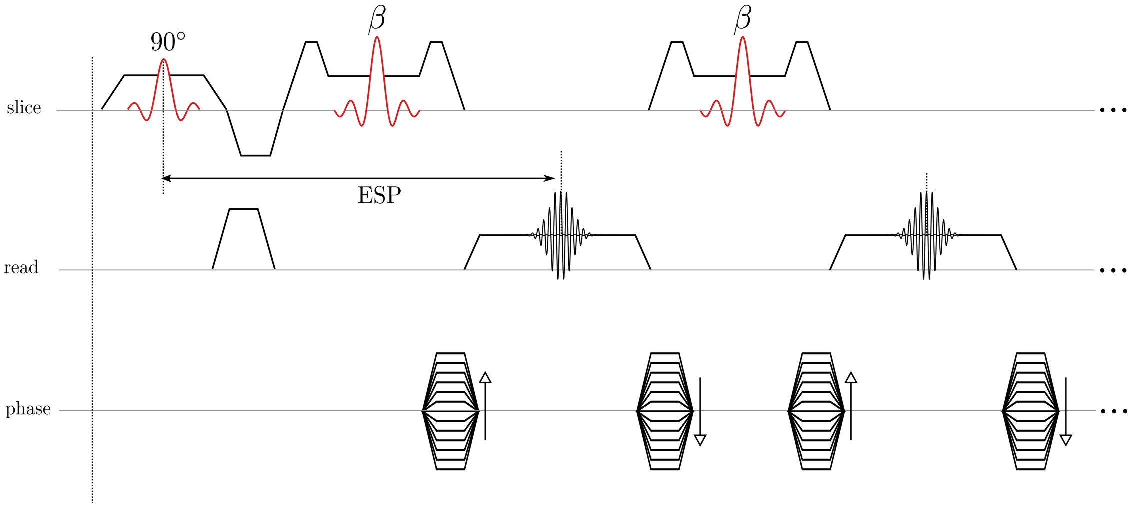

Figure 2.7: Diagram of a turbo spin-echo sequence. After a 90° excitation pulse, the magnetization is refocussed multiple times using ETL RF-pulses with flip angles β, leading to the same number of different echoes.

Using a RF-pulse to refocus magnetization and to generate an echo, spin-echo sequences are insensitive to off-resonance effects and produce images with a T_2 weighted contrast. To obtain a fully sampled image using a conventional spin-echo sequence, a large number of excitations have to be performed depending on the desired resolution. Between excitations, long dead-times are required for the complete T_1 relaxation of the magnetization, leading to long repetition times TR. While the necessary time for gradients and RF-pulses for the acquisition of a single spin-echo lies in the range of < 10 ms, the transversal magnetization generated by one excitation exists for at least 100 ms for some tissue types before it has completely decayed due to T_2 relaxation. Thus, a spin-echo experiment only makes use of a small fraction of the complete signal and is very inefficient. As for all sequences with a long TR, efficiency can be increased for multi-slice experiments by an interleaved acquisition, where data for different slices are acquired in a single TR.

Turbo spin-echo acquisition techniques, first introduced by Hennig et. al. under the name Rapid Acquisition with Relaxation Enhancement (RARE, [3]), employ additional RF-pulses to refocus a single spin-echo several times. Figure 2.7 shows a typical diagram of a TSE sequence. A slice-selective excitation pulse with a flip angle of $\alpha = 90°$ is followed by a train of ETL pulses with flip angles β. Each pulse β refocuses the magnetization and leads to ETL echoes at different echo times $\mathrm{TE}_n = n \cdot \mathrm{ESP}$, where ESP is the temporal spacing between subsequent echoes.

In practice, it is very difficult to obtain a perfectly homogeneous excitation profile across the whole slice. Instead, some parts experience a flip angle lower than 180°. To dephase unwanted transversal magnetization generated by the imperfect refocussing pulses, the slice selection gradients are surrounded by identical crusher gradients. Furthermore, all echoes $n \geqslant 2$ are no pure spin-echoes but exhibit contributions from other echo paths, namely from stimulated echoes [23, 24].

Nonetheless, the spin-echoes are dominant and an approximately exponential decay of the signal intensity can be observed for a given tissue. To guarantee a coherent superposition of all possible echo paths (e.g. stimulated echoes and spin-echoes always have the same phase in the transversal plane), a few requirements have to be met by a TSE sequence, known as CPMG (Carr-Purcell-Meiboom-Gill) conditions [25, 26]:

- Refocussing pulses are spaced equidistantly from each other and symmetric to the echoes.
- The phase of the refocussing pulses is chosen with an offset of $\pi/2$ compared to the excitation pulse. This leads to a constant location of the echoes in the rotating reference frame.
- The total gradient moment $\int \mathrm{d}t\ G(t)$ in each interval between RF-pulses is constant for each gradient axis.

In a TSE sequence, individual echoes in an echo train are acquired at different time points after the excitation. Due to T_2 relaxation, they therefore carry different contrast information. Typically, the contrast evolves from a proton density contrast (with T_1 weighting in the case of short TRs) for the first echo to a strongly T_2 weighted contrast for the last echo. In order to reconstruct a single image with a specific contrast from a TSE data set, the data have to be carefully arranged in k-space. Following the considerations in section 2.2.3, data acquired at the desired echo time are placed in the center part of k-space, while other regions are filled with remaining acquired data. To obtain artifact-free images, large jumps in signal intensity (= large ΔTE) between adjacent phase encoding lines have to be avoided. Possible reordering schemes for a Cartesian TSE sequence with ETL = 11 for a proton density and a T_2 weighted image are shown in Figure 2.8. A TSE acquisition reduces measurement time by a factor of ETL when compared to a spin-echo while preserving a similar contrast. However, some unwanted contrast contributions may appear especially in PD weighted images, which is investigated in Chapter 4 in more detail .

2.4 Non-Cartesian sampling strategies

So far, only the Cartesian acquisition scheme has been discussed, that acquires a data sample at each Cartesian k-space point. Images can then be reconstructed using a simple fast Fourier Transform. Mostly due to their straightforward and very quick reconstruction as well as high robustness, Cartesian MRI scans account for the overwhelming majority of all clinical exams.

Non-Cartesian sampling schemes do not restrict themselves to points on a rectangular grid but acquire data at all arbitrary k-space locations that can be reached by gradient encoding. This provides a high degree of freedom for the trajectory, with a main limitation set by gradient performance. A large variety of non-Cartesian sampling schemes have been proposed, that exhibit unique properties.

Radial sampling, which was employed in the first MRI experiment in 1973 [1] and lead to the Nobel prize for Lauterbur and Mansfield, is the most widely used non-Cartesian strategy today. Here, straight lines are acquired across k-space at different angles. This is advantageous particularly for dynamic imaging and discussed in more detail below. Spiral trajectories start in k-space

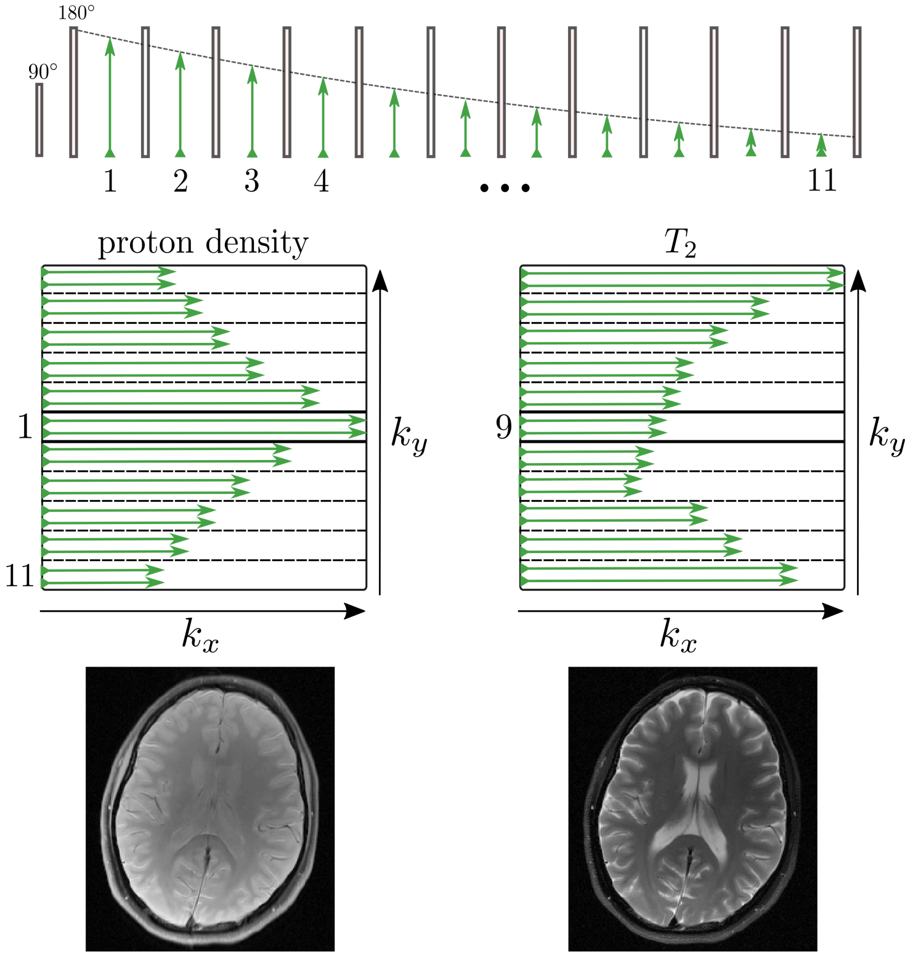

Figure 2.8: Two reordering schemes yielding different contrasts for a TSE sequence with a train length of 11. Echoes in one echo train decay exponentially according to T_2. Assembling the k-space center from the first echo leads to a proton density weighted image (left). Using a later echo instead leads to a T_2 weighted image (right).

center [27, 28] and allow a fast data acquisition due to the typically high number of samples acquired per readout gradient. A different example is PROPELLER [29], that combines radial and Cartesian sampling by acquiring a set of parallel lines at different angles in k-space and allows for retrospective motion correction.

Non-Cartesian sampling schemes can be combined with many different sequences. In contrast to Cartesian imaging, they often require time-varying gradients, which poses technological challenges.

2.4.1 Radial sampling

In radial sampling, a straight line (= projection) crossing the k-space center is acquired at a different angle for each echo. This is implemented by two simultaneous constant gradients on both axis in the transversal plane. For different projection angles, the gradient amplitudes are varied according to the trigonometric relations. With each echo, radial sampling provides information about both contrast (k-space center) and fine structures (k-space periphery) of the object. This is very useful for dynamic imaging. Additional advantages inherent to radial sampling strategies are a high robustness with regard to patient motion and flow [30, 31].

For a given number of projections, there are different ways to reorder the corresponding angles in the transversal plane. Depending on the particular application, a specific reordering scheme has to be chosen. An uneven distribution of data with (larger) gaps in k-space can lead to stronger aliasing artifacts and so negatively affect image quality. The two most important reordering schemes are linear and golden-ratio sampling, as depicted in Figure 2.9:

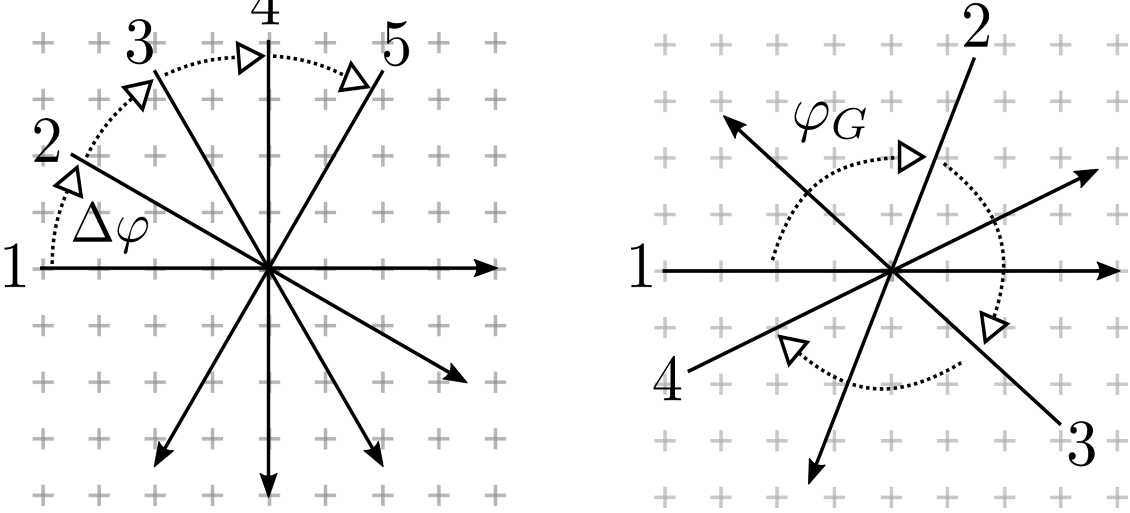

Figure 2.9: Linear (left) and golden angle (right) reordering scheme for radial sampling.

- In **linear sampling**, the projection angle is raised by a linear increment $\Delta\varphi = \pi/N_P$ for subsequent projections, where N_P is the total number of projections. This leads to a very uniformly sampled k-space and consequently to the least prominent artifacts for undersampled data. A drawback is the inflexibility of this approach, where the total number of projections for each image has to be specified before the acquisition.

- **Golden-ratio sampling** [32] increases the projection angle for subsequent projections by the golden angle increment $\varphi_G = 180°/\gamma \approx 111.25°$ with $\gamma = 0.5 \cdot (\sqrt{5} + 1)$. The angle for the nth projection then is given by $\varphi_n = \operatorname{mod}(n \cdot \varphi_G, 180°)$. The big advantage of the golden-angle approach is its high flexibility. For radial data acquired with golden-ratio sampling, it is possible to freely choose the number of projections for the reconstruction of an image even after data acquisition, as subsets of the full data set also cover the whole k-space plane. This makes the golden-angle reordering especially useful for dynamic imaging. Due to the non-linear modulus operation, in contrast to linear sampling this does not result in an exact evenly distributed k-space. However, a good uniformity is still achieved for an arbitrary number of projections. This is true especially if N_P is chosen to be a Fibonacci-number.

2.4.2 Reconstruction of non-Cartesian data

Non-Cartesian sampling strategies have both some inherent advantages and drawbacks when compared to Cartesian acquisitions. One drawback of non-Cartesian imaging is its more complicated and more time-consuming reconstruction. Mostly, in a step called gridding the non-Cartesian data points are moved onto a Cartesian grid. Afterwards, a simple inverse FFT yields the corresponding image. In this section, the most common procedure to generate images from fully sampled non-Cartesian data sets is described, called non-uniform Fourier Transform (NUFFT, [33]). In another method with the name GRAPPA operator gridding (GROG [34]), parallel imaging is utilized to obtain points on a Cartesian grid. This method is explained in more detail in section 6.2.2.

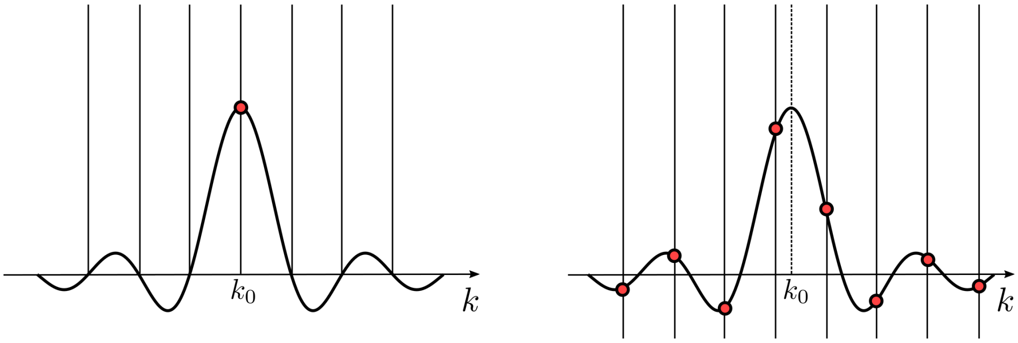

Figure 2.10: Point spread function induced by a limited field of view. Left: Cartesian Sampling. Off all discrete locations, the PSF only has a value other than zero at the location k_0 of the sampled point. Right: Non-Cartesian sampling. Sampling a point at the non-Cartesian location k_0 leads also to a shift of the central peak of the PSF to this location. Now, the PSF has a non-vanishing value at all Cartesian grid points.

To motivate the NUFFT, consider the impact of a finite field of view on the point spread function

(PSF) of a single k-space point. To keep description simple, this is done in a singular dimension, but the concept can be easily extended to a multidimensional space. A single k-space sample at the location k_0 in a continuous base is given by

$$S(k) = a \cdot \delta(k - k_0), \tag{2.36}$$

where $a \in \mathbb{C}$. The corresponding inverse FT therefore leads to $a \cdot e^{-ik_0 x}$. Introducing a limited field of view of extent $2d$ corresponds to

$$I(x) = a \cdot e^{-ik_0 x} \cdot \Theta(d + x)\Theta(d - x), \tag{2.37}$$

where $\Theta(x)$ is the Heaviside function. The back-transformation into k-space yields the point spread function (PSF)

$$PSF(k) = FT(I(x)) = \int_{-d}^{d} \mathrm{d}x \; a \cdot e^{-ix(k-k_0)} \propto \frac{\sin(d(k - k_0))}{d(k - k_0)}, \tag{2.38}$$

which is the sinc-function $\mathrm{sinc}(x) = \sin(x)/x$. Hence, a limited FOV leads to a distribution of one single point across k-space. However, as shown in Figure 2.10 for Cartesian sampling, the PSF at all discrete locations other than $k = k_0$ are zero and the limited FOV does not have an impact. For points at non-Cartesian locations however, the central peak of the PSF does not coincide with a Cartesian grid point and to obtain a Cartesian k-space, every non-Cartesian point has to be convoluted with a sinc-function, providing values at each Cartesian grid point. As this is computationally expensive and the sinc-function drops off quickly, convolution kernels with a more localized support such as Kaiser-Bessel-functions are usually applied in NUFFT reconstructions as an accurate approximation [33, 35]. By performing the inverse operation, the same approach can be used to simulate non-Cartesian data from a Cartesian data set. Besides image reconstruction from fully sampled non-Cartesian data sets, convolution (de-)gridding is routinely applied in many iterative algorithms that reconstruct unaliased images from undersampled data sets.

Density Compensation

To obtain artifact-free images using convolution gridding, one more important point has to be considered. Through convolution with the gridding kernel, every measured point is distributed over several Cartesian grid points independently and the final k-space is obtained by summing over the result for every non-Cartesian point. However, unlike for Cartesian sampling, points are in most cases not sampled at equidistant locations in k-space. Not taking this into account results in an effective k-space filter with too high values of locations with a high sampling density. Figure 2.11 illustrates the related artifacts for radial sampling.

To prevent this k-space filter, all non-Cartesian points have to be multiplied by a set of real-valued positive weights before performing the convolution. This process is called density compensation. Several methods have been proposed to calculate an optimal set of weights, that is called density compensation function (dcf). Voronoi diagrams [36] can be used to estimate the area occupied by each point. Weights are then generated by dividing by the inverse of that value and are therefore based explicitely on the point density. Other methods such as [37, 38] retrieve an optimal dcf by applying the convolution gridding itself, which is explained in more detail in the following paragraph.

Very generally, the sampling process in MRI can be represented by

$$y = E \cdot x, \tag{2.39}$$

where y and x are the vectors of the k-space and the object respectively. The encoding matrix E incorporates all necessary information such as type of trajectory and k-space locations of sampled data. An image can be calculated from a set of data points y by applying the operator E^H, which represents a simple inverse Fourier transform (Cartesian sampling) or a combined gridding and Fourier transform operation (non-Cartesian sampling).

Using an optimal dcf for a particular set of fully sampled non-Cartesian data, a gridding (E^H) and a subsequent degridding (=sampling) operation

$$y' = E(E^H(y)) \tag{2.40}$$

applied to a set of data points y should have no effect and $y' = y$ holds. When the dcf is not known, this equation can be used to obtain a good approximation of the dcf by applying it to a data set of points equal to one with a first estimate of dcf=1. The result of degridding is then used to calculate an updated dcf $dcf' = 1/y'$ for each point. Then the whole process is repeated and iterated until convergence.

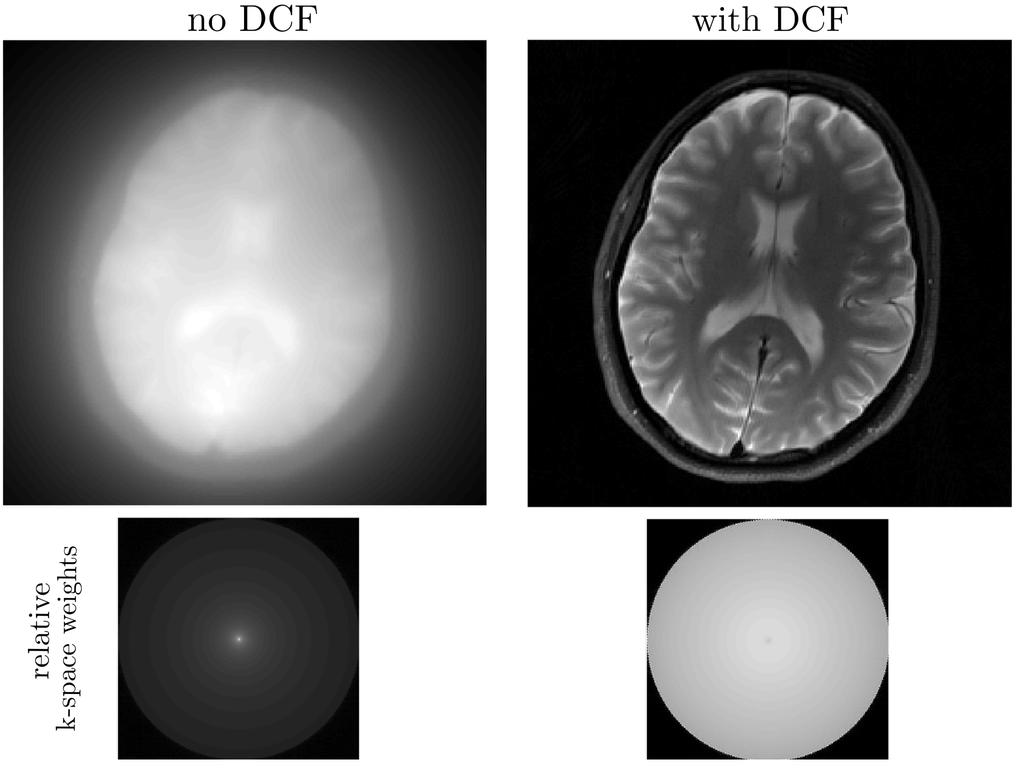

Figure 2.11: Radial brain images reconstructed with convolution gridding without (left) and with (right) density compensation function. The corresponding relative weighting of Cartesian k-space points after gridding is shown below. As every radial line crosses the k-space center, using no dcf in the gridding reconstruction leads to a k-space filter with a peak in the center and in turn to artifacts in the reconstructed image.

CHAPTER 3

Image reconstruction from incomplete data sets

Over the last decade, image reconstruction from undersampled data has become one of the most important topics in MRI research. Due to physiological constraints, it is very difficult to further accelerate data acquisition by any significant amount using stronger gradients. Instead, further reduction of measurement time is possible by acquiring only part of the conventionally required information in k-space. This results in artifacts in the images, which then have to be removed in a post-processing step. As introduced in the last section, the sampling process in MRI can be described by

$$y = E \cdot x, \tag{3.1}$$

where y are the x-space data and x represents the object. To obtain an image, this equation has to be solved for x. In the case of a Cartesian acquisition, E = FT is equal to the Fourier operation and for fully sampled data the solution $x = \mathrm{FT}^{-1} \cdot y$ is easily obtained. However, if too little data y are acquired, the system of equations is underdetermined and many solutions x are possible that agree with the data. The extent of the scan time reduction is represented in the acceleration factor, which is defined as

$$R = \frac{\textbf{total number of k} - \textbf{space points}}{\textbf{number of acquired points}}, \tag{3.2}$$

so for example acquiring only every third point results in $R = 3$. In this work, two fundamentally different mechanics are used to retrieve the correct solution from an undersampled data set:

- Instead of only one homogeneous receiver coil, multiple surface receiver coils are nowadays typically used to independently and simultaneously acquire the data. As the coils are placed at different locations on the surface of the object, each is sensitive to a different region of the object. Therefore, the number of independent linear equations is raised by the number of independent sensitivity profiles present in the coil array and equation 3.1 can be solved even in the presence of undersampling. Methods exploiting the additional spatial information provided by multi-coil receiver arrays are known as parallel imaging.

- Prior knowledge about the object can be used to pick the correct solution from all possible x that solve equation 3.1 for undersampled data. These methods are known as constrained reconstructions for obvious reasons. A popular constrained reconstruction method is compressed sensing, that chooses the solution with the highest sparsity (=smallest support) in some domain.

This chapter reviews the basics of both parallel imaging and compressed sensing and presents the most important reconstruction algorithms used in this work.

3.1 Parallel Imaging

The introduction of phased receiver arrays [39] of multiple surface coils for the acquisition of the MRI signal paved the way for the development of parallel imaging (pMRI). While receiver arrays are a requirement for parallel imaging, they were developed roughly 10 years before the breakthrough of pMRI. The main motivation of receiver arrays are images with an improved SNR. The spatially varying information provided by a receiver array is shown in Figure 3.1. Each coil independently acquires an image, that is equal to the whole image modified by the coil sensitivity profile. Each coil therefore has a different 'view' of the object. This provides additional spatial information, which can be exploited for the reconstruction of aliasing-free images from undersampled data sets.

Early proposals of parallel imaging were already made near the end of the 1980s ([40, 41]) and concerned themselves with not only reducing the number of acquired phase encoding lines but with completely replacing spatial phase encoding. Consequently, they required a large number of receiver coils, which is not feasible for a number of different reasons. At that time, production of receiver arrays with such a high number of coils was technically not possible. Only in recent years, coil arrays with many channels emerged. Furthermore, even if both the acquisition and reconstruction could be achieved, it would come with a significant decrease in SNR because only a single k-space line is acquired.

It took nearly another decade, until Sodickson et al. proposed a method called Simultaneous Acquisition of Spatial Harmonics (SMASH, [4]) using parallel imaging as a complement rather than a replacement for Fourier encoding. SMASH reconstructs missing points in k-space by approximating the Fourier encoding directly with the coil sensitivity information and can be considered the breakthrough of pMRI. A next major step was made by Pruessmann et al two years later, who formulated the reconstruction in image- rather than k-space. Their method called sensitivity encoding (SENSE, [6]) is still one of the most important pMRI methods today. In 2001, an adaptation of this method for the reconstruction of arbitrary trajectories followed [42]. Further improvements on the original SMASH method were the implementation of auto-calibration [43, 44] and also the adaptation to irregular sampling schemes [45]. Generalized auto-calibrating partially parallel acquisition (GRAPPA, [5]) was introduced by Griswold et al in 2002, replacing SMASH. While also a pure k-space based technique, in contrast to existing methods it allowed reconstruction at small computational cost and yielded separate images for each individual coil.

In clinical practice today, SENSE and GRAPPA are the two most important reconstruction methods that are used on a daily basis in MRI experiments. Both methods reduce acquisition times while retaining diagnostic image quality and are introduced in detail below. Many more pMRI reconstruction methods have been introduced over the last decade. More complete reviews of parallel imaging can for example be found in [46–48]

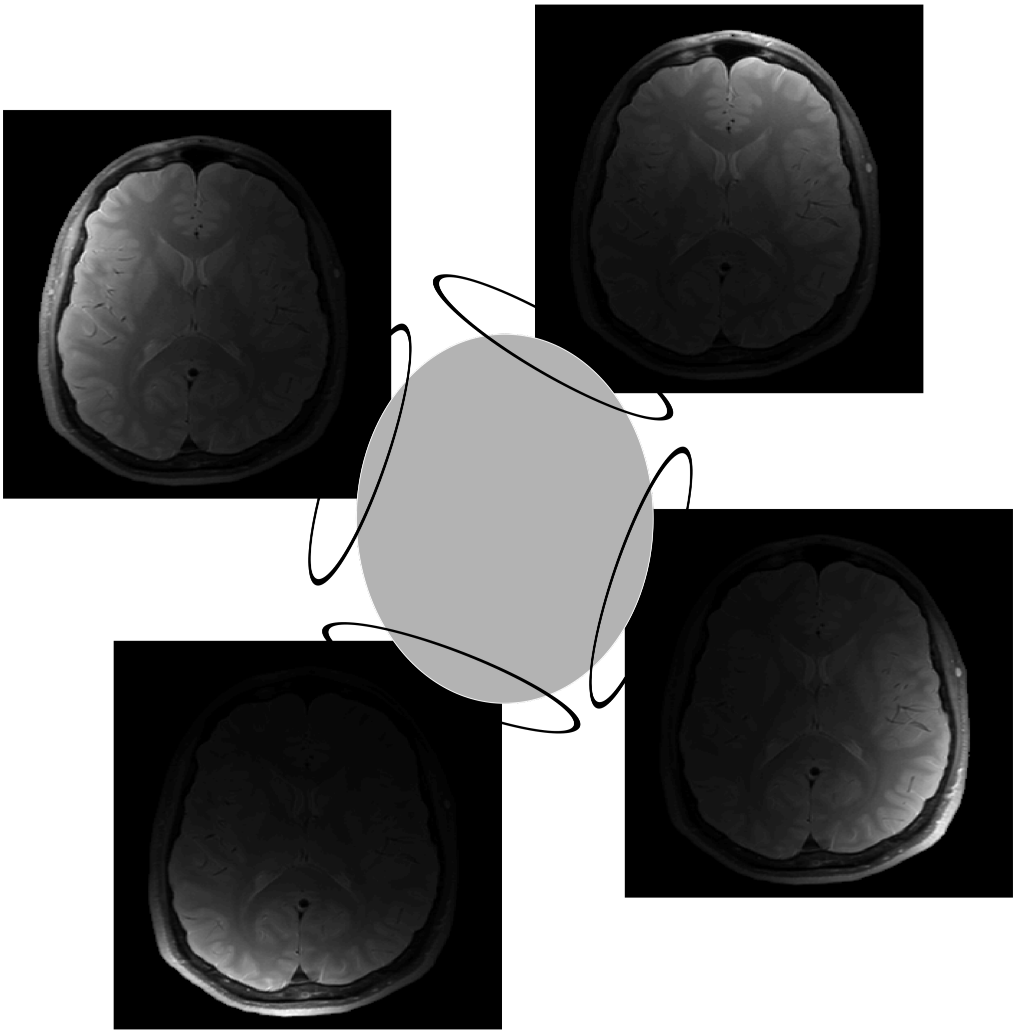

Figure 3.1: Brain images detected by an array of receiver coils. The resulting image 'seen' by each coil is equal to the object multiplied by the coil's sensitivity function.

3.1.1 Sensitivity Encoding (SENSE)

As mentioned before, parallel imaging speeds up MRI by acquiring only a subset of all k-space points and retrospectively reconstructing the missing data. In the Cartesian case, this is achieved by omitting a certain number of phase encoding lines. For reasons that will become clear later on, a regular sampling pattern with a fixed distance Δk between acquired phase encoding lines is profitable for established 2D Cartesian parallel imaging methods.

Fig. 3.2 shows a typical sampling pattern for $R = 2$ and the corresponding aliasing artifacts. Acquiring every other line in k-space doubles Δk and therefore leads to a reduction of field of view by half, so that every point of the aliased image is a combination of two points of the fully sampled image. The same observation holds true for a acceleration factor R, where now R pixel of the unaliased image are combined into a single pixel in the aliased image.

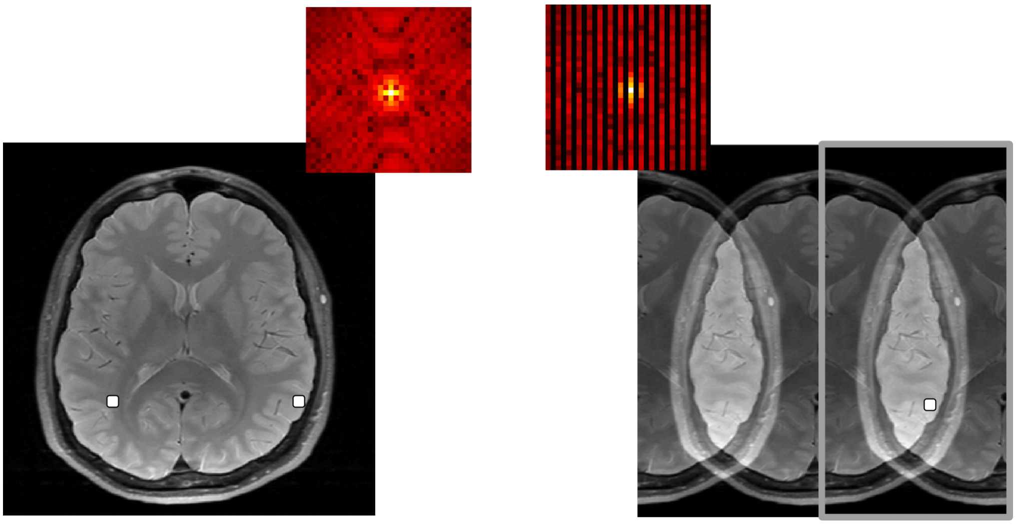

Figure 3.2: Fully sampled image (left) and R=2 undersampled image (right), where every second k-space line is omitted. This leads to a superposition of two replicas of the image, shifted by FOV/2, also known as aliasing or folding artifacts.

SENSE [6] is possibly the most direct approach to removing the aliasing artifacts in the accelerated image making explicit use of the coil sensitivity profiles. The sensitivity encoding by a receiver array as shown in Fig. 3.1 can be summarized in a single expression

$$\boldsymbol{I} = C\boldsymbol{\rho}, \tag{3.3}$$

where $\boldsymbol{\rho}$ is the image of the object, $\boldsymbol{I} = (\boldsymbol{I}_1, \boldsymbol{I}_2, \dots, \boldsymbol{I}_{nc})$ is the signal of all nc coils in image space and C is a matrix incorporating the coil sensitivity information. The image $\boldsymbol{\rho}$ has only $N_x \times N_y$ entries, while for a fully sampled 2D MRI exam $\boldsymbol{I}$ has nc times that number.

Acceleration of the MRI scan leads to a reduction of the field of view by R, so that now every coil exhibits R folding artifacts. This can be described by considering a single pixel in the aliased image as depicted in Fig. 3.2. The pixel at location A in the image of the ith coil is the combination of R pixels of the unaliased image, weighted by the sensitivity profile at the corresponding locations, each shifted by an additional FOV/R in the accelerated dimension.

$$I_i(A) = \sum_{n=0}^{R-1} C_i(A_n) \cdot \boldsymbol{\rho}(A_n), \tag{3.4}$$

where $A_n = A + n \cdot FOV/R$. This equation for the pixel at location A can be rewritten using matrix formulation considering all coils:

$$\boldsymbol{I}(A) = \begin{pmatrix} C_1(A_0) & \dots & C_1(A_{R-1}) \\ \dots & \dots & \dots \\ C_{nc}(A_0) & \dots & C_{nc}(A_{R-1}) \end{pmatrix} \begin{pmatrix} \boldsymbol{\rho}(A_0) \\ \dots \\ \boldsymbol{\rho}(A_{R-1}) \end{pmatrix} = \hat{C} \cdot \hat{\boldsymbol{\rho}} \tag{3.5}$$

To obtain the values ρ of the unaliased image, this system of equation has to be solved. One possible way to do this is by simply performing the pseudo-inverse of the coil sensitivity matrix $\hat{C}$ so that

$$\hat{\boldsymbol{\rho}} = \text{pinv}(\hat{C}) \cdot \boldsymbol{I}(A). \tag{3.6}$$

Here, the pinv represents the Moore-Penrose pseudo-inverse, that is typically used instead of a true inversion as C is usually no square matrix. It is given by

$$\text{pinv}(\hat{C}) = (\hat{C}^H \hat{C})^{-1} \hat{C}^H. \tag{3.7}$$

The matrix $\hat{C}$ has to be assembled and the pseudo-inverse operation performed for each aliased pixel in order to retrieve the whole image. To be able to perform the reconstruction, explicit knowledge about the sensitivity information C_i for each coil is required. It can be obtained with a separate calibration scan before or after the actual measurement. As coil sensitivities are usually slow-changing over the field of view, sensitivity information can be extracted from low-resolution data sets.

SENSE for non-Cartesian trajectories

A Cartesian regular subsampling, as presented above, leads to aliased images where each image pixel is the superposition of R pixels of the unaliased image. As this leads to a system of equations with a rather limited number of unknowns, it is possible to solve it directly.

In contrast, the situation is very different in the case of non-Cartesian undersampled data. Figure 3.3 shows the point spread funcion (PSF) of an accelerated radial acquisition. For radial sampling, as well as for other non-Cartesian trajectories, each point is aliased onto a large number of other pixels all over image space. Therefore, using the same procedure as for the Cartesian case would result in a very large number of intertwined equations, that cannot be solved in a reasonable amount of time and with limited computer memory. Instead, the idea presented by Pruessmann et al in 2001 is to solve the equations numerically and iteratively using a conjugate gradient (CG) algorithm [42]. A good introduction to conjugate gradient is given in [49]. The main advantage of the CG algorithm over other existing methods is its fast convergence. Performing a gridding

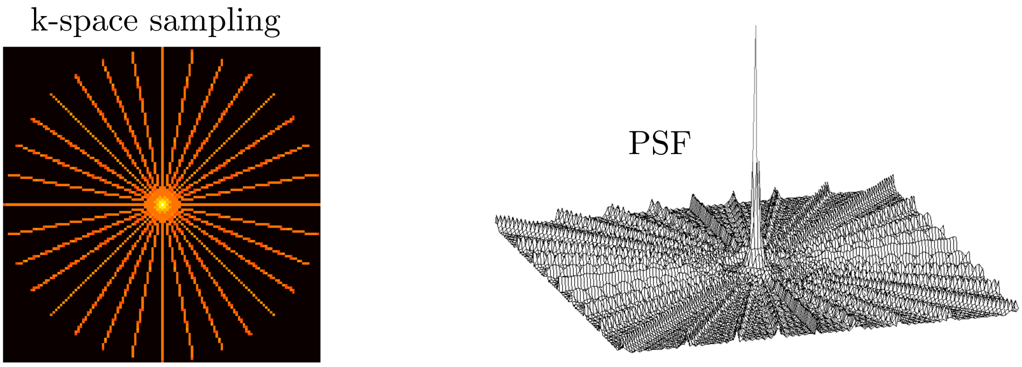

Figure 3.3: Undersampled radial k-space (left) and the point spread function corresponding to this sampling scheme. In radial data, undersampling leads to streaking artifacts in the images, where a single point is distributed radially across the whole image.

operation described in detail in chapter 2.4 takes both sides of equation 3.1 into image space

$$E^t\, y = E^t E\, x, \tag{3.8}$$

which is the central equation that can then be solved with using CG. Hereby, y is multi-coil data sampled according to an arbitrary scheme and x is the single-channel image. Hence, the encoding matrix E contains information about the sampled k-space locations as well as the coil sensitivities. The gridding operator E^t additionally includes the density compensation function, which is not necessarily needed but leads to a faster convergence due to a better first estimate.

To obtain the exact solution, many iterations of CG-SENSE would be needed, which is not feasible due to noise enhancement and the long reconstruction times. However, due to the beneficial convergence properties of the conjugate gradient algorithm, even for a much smaller number of iterations the deviations are small enough to provide satisfying results.

3.1.2 GRAPPA

Like its predecessor SMASH, GRAPPA [5] operates completely in k-space by calculating missing data points directly. During reconstruction, for each individual coil a fully sampled data set is generated. In contrast to other methods that yield a single combined channel, this has the advantage of leaving the freedom to subsequently apply an optimal channel combination algorithm. Additionally, methods such as SMASH that use a simple complex sum for channel combination can lead to phase cancellations in the image.

To understand how GRAPPA works, it is necessary to revisit the data sampling process, taking coil sensitivity profiles into account. Following equation 2.17, the value of a single k-space point at the phase encoding location $\boldsymbol{k}_0$ for the ith coil is given by

$$S_i(\boldsymbol{k}_0) = \int \mathrm{d}^N\boldsymbol{r}\; C_i(\boldsymbol{r}) \cdot \rho(\boldsymbol{r}) e^{-i\boldsymbol{k}_0\cdot\boldsymbol{r}} \tag{3.9}$$

where $\rho(r)$ is the spin density, $k_n = n \cdot \Delta k$ is the k-space line and $C_i(r)$ corresponds to the coil sensitivity profile. To calculate the value of a missing k-space point in a single coil, GRAPPA performs a linear superposition of the values of neighboring points across all coils. An example is shown in Figure 3.4 for an acceleration factor of R=2. To reconstruct a missing point (=target point) in a single receiver coil, a superposition of the six closest neighbors (=source points), across all coils is performed. The optimal choice of source and target points depends among other things on the acceleration factor, the coil sensitivity profiles, the properties of the object and the acquisition parameters. In practice, Kernels with a larger number of source points than in the example shown are very common.

To understand the implications of the GRAPPA reconstruction, consider a missing point at the k-space location $\boldsymbol{k}_0$. The linear superposition of the N_{SP} neighboring points across all N_C coils yields

$$\begin{aligned}
S_j(\boldsymbol{k}_0) &= \sum_{p=1}^{N_{SP}} \sum_{n=1}^{N_C} a_{nj}^p S_n(\boldsymbol{k}_p) && (3.10)\\
&= \sum_{p=1}^{N_{SP}} \sum_{n=1}^{N_C} \left(a_{nj}^p \int \mathrm{d}^N \boldsymbol{r}\; C_n(\boldsymbol{r}) \rho(\boldsymbol{r}) e^{-i\boldsymbol{k}_p \cdot \boldsymbol{r}} \right) && (3.11)\\
&= \sum_{p=1}^{N_{SP}} \sum_{n=1}^{N_C} \left(\int \mathrm{d}^N \boldsymbol{r}\; C_n(\boldsymbol{r}) \rho(\boldsymbol{r}) e^{-i\boldsymbol{k}_0 \cdot \boldsymbol{r}} \cdot a_{nj}^p e^{-i\Delta \boldsymbol{k}_p \cdot \boldsymbol{r}} \right) && (3.12)\\
&= \int \mathrm{d}^N \boldsymbol{r}\; \rho(\boldsymbol{r}) e^{-i\boldsymbol{k}_0 \cdot \boldsymbol{r}} \cdot \sum_{p=1}^{N_{SP}} \sum_{n=1}^{N_C} \left(C_n(\boldsymbol{r}) a_{nj}^p e^{-i\Delta \boldsymbol{k}_p \cdot \boldsymbol{r}} \right). && (3.13)
\end{aligned}$$

Hereby, $\boldsymbol{k}_p = \boldsymbol{k}_0 + \Delta \boldsymbol{k}_p$ with small values for $\Delta \boldsymbol{k}_p$, as only points in the neigborhood of $\boldsymbol{k}_0$ are used. For this term to yield the correct value for the missing k-space point, the relation

$$\sum_{p=1}^{N_{SP}} \sum_{n=1}^{N_C} C_n(\boldsymbol{r}) a_n^p e^{-i\Delta \boldsymbol{k}_p \cdot \boldsymbol{r}} = C_i(\boldsymbol{r}) \tag{3.14}$$

has to hold. As the coil sensitivity profiles never form a complete set of functions in the mathematical sense, this can only be true as an approximation.

Weight calibration

Prior to reconstruction, the coefficients of the superposition a_{nj}^p, called GRAPPA weights, have to be determined. A separate set of weights is required for each geometrically distinct source-target-point configuration. However, the weights do not depend on the location in k-space and so the same set of weights can be used for the reconstruction of a whole undersampled acquisition. Calculation of the weights is performed in a auto-calibration step using a fully sampled part of k-space called auto-calibration signals (ACS).

The ACS can either be obtained during acquisition or as an extra scan, not even necessarily with the same MRI sequence. This choice has to be made considering the requirements of the application at hand. This is even possible for dynamic imaging, as in contrast to SENSE the calibration is not sensitive to motion. Using a scan embedded in the actual measurement to acquire the ACS lines has the advantage of being able to improve SNR in the final image by replacing the corresponding phase encoding lines in the reconstructed k-space.

The weight calibration is illustrated in Figure 3.5 for the small example GRAPPA kernel used above. In this graph, calibration of the weights is shown for a single target point in one particular coil to simplify depiction. For each occurrence of the reconstruction kernel in the ACS data, the source points across all coils and the target point are assembled, forming a linear system of equations that will be solved to obtain the weights a_j. The number of unknowns (=the number of weights) for reconstructing a single k-space point in a specific coil is given by $N_C \cdot N_{SP}$. Therefore, the ACS data have to be large enough to provide at least the same number of occurrences of the GRAPPA kernel. In practice, a high overdetermination of the set of linear equations yields more stable results. The calibration process can be expressed conveniently using a matrix formulation. Assembling all source points and all target points into a matrix S_{SRC} of size $N_{SP} \cdot N_C \times N_K$, where N_K is the number of kernel repetition in the ACS, and a vector $\boldsymbol{S}_{TRG}$ of size $(N_{TP} \cdot N_K) \times 1$ (here, $N_{TP} = 1$), the relation

$$\boldsymbol{S_{TRG}} = S_{SRC} \cdot \boldsymbol{a_j} \tag{3.15}$$

holds for each individual coil. Now, the weights a_j can be extracted using a least-squares approximation by building the pseudo-inverse of the matrix S_{SRC}:

$$\boldsymbol{a}_j = \mathrm{pinv}(S_{SRC}) \cdot \boldsymbol{S_{TRG}}. \tag{3.16}$$

3.2 Discussion

The development of parallel imaging methods proved to be very valuable for MRI. On the one hand, they are used to reduce the acquisition time of conventional exams. This both increases patient comfort and decreases the number of failed experiments due to patient motion, as the time for the patient to remain completely still is reduced. On the other hand, parallel imaging made a wide range of new applications possible, especially in the area of dynamic MRI, that could not be investigated without an acceleration of acquisition speed.

A big advantage of pMRI is, that it can be combined with all existing sequences and all prior methods to decrease measurement time. All parallel imaging methods exploit the spatial information provided by coil receiver arrays to retrieve aliasing-free images from undersampled acquisitions. The maximum acceleration factor R_{max} that can be achieved is equal to the number of independent sensitivity profiles present in the coil array. In theory, for an ideal combination of coil configuration and sampling pattern, R_{max} is equal to the number of coils. In practice, this is never achieved and the maximum sensible values for R lie well below N_C. If a value R is chosen, that is too high for configuration of the coil array used for data acquisition, some aliasing artifacts will remain in the images after reconstruction.

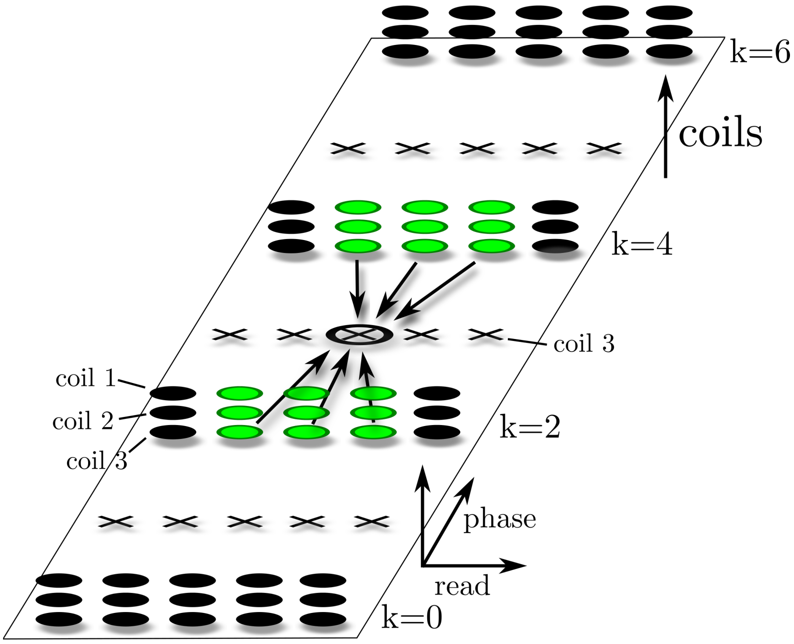

Figure 3.4: GRAPPA reconstruction of a R=2 undersampled k-space using a 3 × 2 GRAPPA kernel. Each missing point in k-space in a single coil represented by 'x' is replaced by a linear combination of the six closest sampled points (solid dots) across all coils.

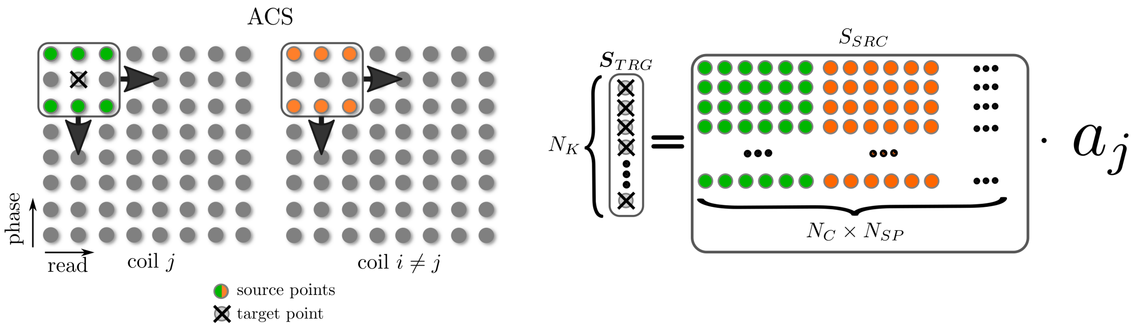

Figure 3.5: Auto-calibration of GRAPPA weights. Using a fully sampled part of k-space (ACS, shown to the left), for all occurences of the chosen GRAPPA kernel, source points across all coils and the target point in coil j are assembled into a matrix and a vector respectively (shown to the right), which are related by the GRAPPA weights a_j. The weights can subsequently be determined by applying the pseudo-inverse of the source matrix S_{SRC}.

Even when a pMRI reconstruction manages to remove all aliasing artifacts, some degradation of image quality is inevitable. The cost of pMRI reconstructions is reduced SNR. The SNR of an image reconstructed with pMRI from data accelerated by a factor of R is given by

$$SNR_{pMRI} = \frac{SNR_{Full}}{\sqrt{R} \cdot g}. \tag{3.17}$$

There are two different contributions to the SNR reduction in comparison to a full acquisition. First, fewer acquired k-space data lower the SNR by itself as this corresponds to fewer averages. This limits the acceleration factors used in clinical practice to a small range. Most common today are reductions of $R = 2$ or at most $R = 4$. Second, the SNR is reduced by the so-called g-factor, which is a result of noise amplification intrinsic to the reconstruction process. It depends on the coil configuration and can be calculated separately for each individual image pixel. SNR considerations are therefore very important for the application of pMRI. In cases of acquisitions with a high intrinsic SNR, a higher acceleration factor might be chosen if the coil configuration permits it.

3.3 Compressed Sensing

As already mentioned in the introduction of this chapter, compressed sensing (CS) belongs to the class of constrained reconstructions. It uses prior knowledge about the object to choose from all possible solutions that solve equation 3.1 for an undersampled data set y. Compressed sensing has its origins in the field of signal processing and was first proposed by Donoho [50] and Candes et al [51]. They were able to show, that the number of data points necessary for a successful reconstruction of a signal does not depend on the size of the space but instead on the information content. Compressed sensing exploits the compressibility of a data set to retrieve a complete signal from an incomplete number of samples. In most cases, image data is highly compressible, which means that its actual information content is much lower than its number of data points in image space. This is used on a daily basis by different *jpg* compression algorithms used for computer graphics/images. Therefore, in conventional fully sampled MRI acquisitions, much more information is obtained than present in the final image. This makes MRI an ideal candidate for the application of compressed sensing and led to the rapid introduction of CS to MRI in 2007 [7] by Lustig et al. Since then, it had and still has an increasing impact in MRI research.

3.3.1 Requirements of compressed sensing

In order to be able to apply CS for the reconstruction of a certain data set, some requirements have to be met. They are intrinsic to CS and do not depend on the specific algorithm used to perform the reconstruction.

Sparsity

A CS reconstruction picks the solution with the highest sparsity from all possible ones that fit the data. Sparsity of data refers to a finite support. This does not necessarily have to be fulfilled in image space. Instead, sparsity can be present in any different base that can be reached by means of a linear invertible transformation. This is called a sparsifying transform.

Figure 3.6 shows three different examples of sparsity that have been used to perform CS reconstructions in MRI. The most prominent example is angiography (shown on the left), where MRI is used to depict blood vessels. Angiograms exhibit a high level of sparsity directly in image space, which make them an ideal candidate for CS reconstructions. Other data (such as the brain image shown in the middle) are not sparse in image space, as can easily be appreciated. An important sparsifying operation is the Wavelet-Transform, which can also be applied to this example. A temporal series of images of a dynamic periodic motion exhibits sparsity in xf-space (f = temporal frequency), which can be reached by a conventional Fourier transform in time. A different popular representation called total variation (TV) is given by computing the difference of values of neighbouring pixels [52], which is very sparse for piece-wise constant images. For optimal results, sparsity can be enforced in different domains simultaneously. In general, a compressed sensing algorithm finds a solution to the inverse problem, that is compressible with respect to the sparsifying transform Ψ.

Incoherent measurement base

As CS reconstructs an image from a incomplete number of data sets, each data sample has to carry information about the whole object. If this were not the case, certain characteristics of the signal might be lost by omitting the corresponding data points during acquisition. For MR, this requirement is automatically met as measurements are performed in Fourier space of the object. A single Fourier sample (= k-space data point) has information about each temporal frequency of the object.

Incoherent sampling

While parallel imaging profits from a regular sampling pattern with coherent aliasing artifacts, the opposite is true for compressed sensing. CS reconstructions require a first estimate of the image from the sub-sampled data, where main characteristics can already be identified. For coherent aliasing artifacts, CS algorithms cannot distinguish between the ’real’ signal peaks and their identical copies and therefore do not converge to the correct solution. Ideal for CS are noise-like incoherent undersampling artifacts, that are for example generated by a random variable-density sampling scheme. Figure 3.7 shows a brain image, that was undersampled by a factor of 4 using variable-density random sampling. In practice, MRI sequences acquire data along a continuous path through k-space and this type of sampling for the Cartesian 2-dimensional case can only be performed in phase encoding direction. Therefore, a sampling scheme well suited for CS is not easily obtained. Non-Cartesian alternatives that have been used in combination with CS include radial and spiral trajectories.

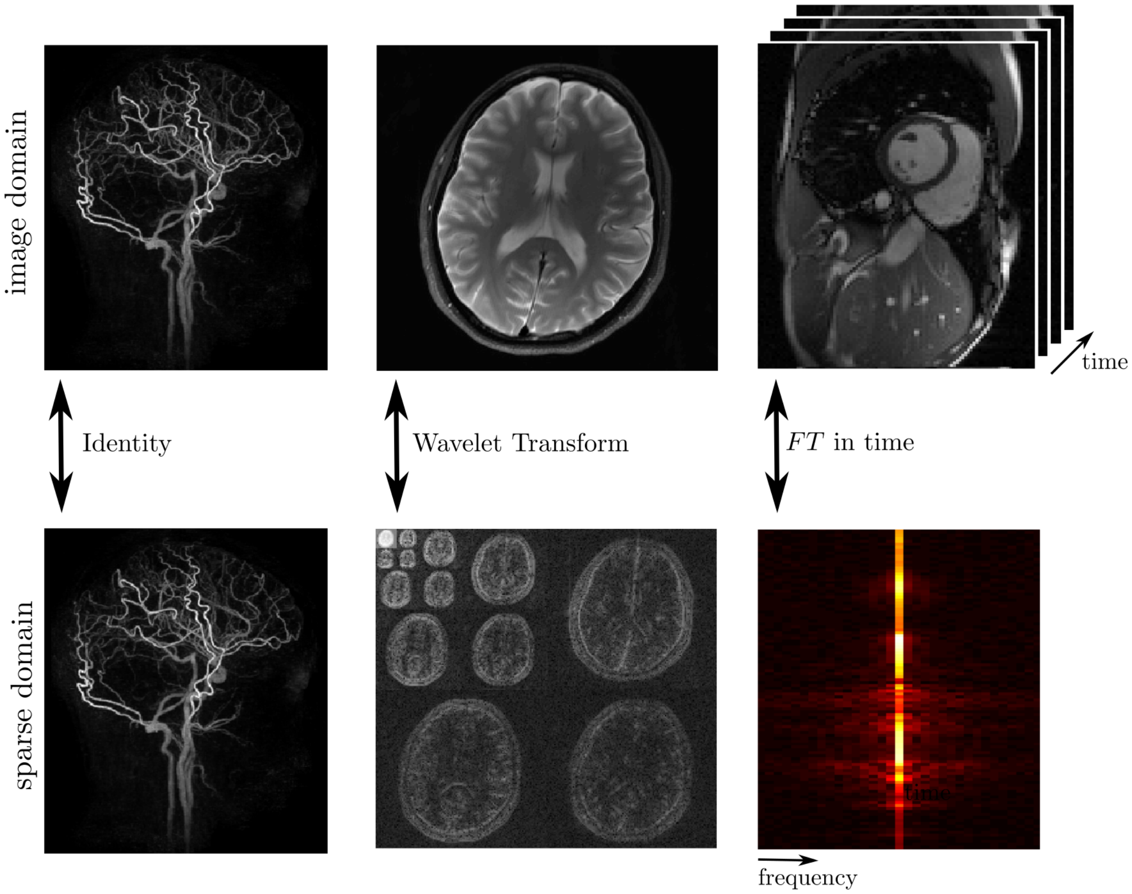

Figure 3.6: Three different examples of sparse data in MRI. MRI Angiography (left, courtesy of Dr. Gregory Lee, Cincinnati Children's Hospital) is sparse in image domain itself. Brain data among others is sparse in the Wavelet-domain (middle). Periodic motion only in a limited region within the FOV such as in cardiac imaging leads to sparsity in frequency space (right).

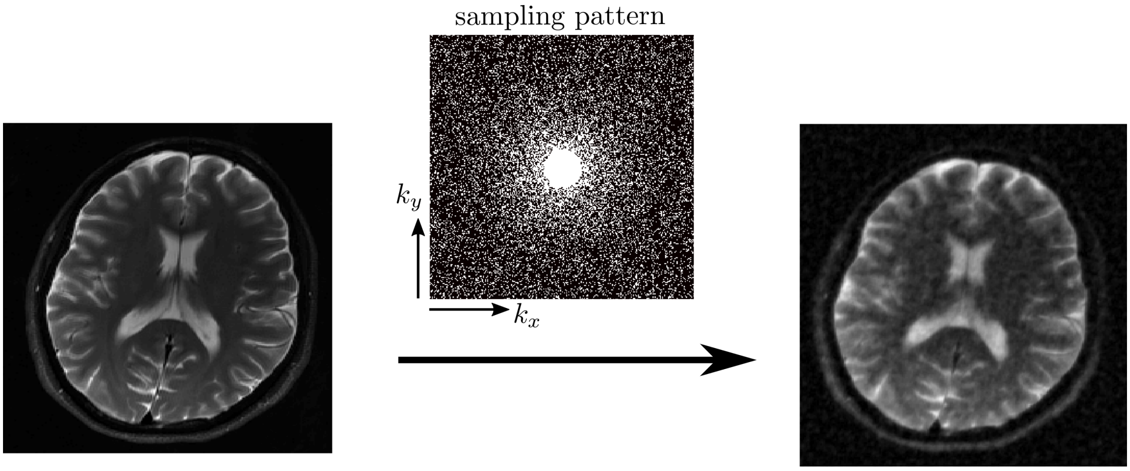

Figure 3.7: Variable density random undersampling. Aliasing artifacts have a noise-like characteristics, while the main characteristics of the image are still discernible.

3.3.2 Iterative soft threshold reconstruction algorithm

The iterative soft threshold (IST) algorithm is a conceptually simple and very intuitive way to implement compressed sensing. It was introduced by Stern et al in 2007 [53]. For a Cartesian sub-Nyquist data set with data samples S at the locations $\boldsymbol{k}^S$, the individual steps are given by:

1. Perform the inverse Fourier transform of undersampled k-space to obtain an image containing aliasing artifacts.
   $$\mathrm{img}^n = \mathrm{FT}^{-1}(\mathrm{ksp}^n), \tag{3.18}$$
   where $n = 0 \dots N - 1$ stands for the current iteration

2. Apply a soft threshold to the signal intensity in image space:
   $$\mathrm{abs}(\mathrm{img})^n = \max(\mathrm{abs}(\mathrm{img}^n) - \epsilon, 0) \tag{3.19}$$
   This step reduces the signal intensity in each pixel by ϵ, which is the only parameter in this algorithm and should be of the order of the magnitude of noise-level present in the data set. Hereby, the intensity cannot drop below zero.

3. Transform back into k-space
   $$\mathrm{ksp}^{n+1} = \mathrm{FT}(\mathrm{img}^n) \tag{3.20}$$
   and enforce consistency with the acquired undersampled data S (i.e. replace by measured signals)
   $$\mathrm{ksp}^{n+1}(\boldsymbol{k}^S) = S. \tag{3.21}$$

The IST algorithm is easy to implement and computationally not very expensive, as it mainly consists of fast Fourier transforms. However, it needs a rather large number of iterations for convergence. Figure 3.8 shows a IST reconstruction from a one-dimensional sparse data set of size 64×1 with only 4 samples with no noise (shown on the top left), that was subsampled randomly by a factor of $R = 4$ as shown on the top right. Reconstructed images at different iterations are shown below. The aliasing artifacts get gradually suppressed by the thresholding operation, until at iteration 400 few aliasing artifacts remain. At iteration 600, the signal is recovered perfectly. If the data set is sparse in a domain other than image space, the respective transform is needed before and after the threshold operation.

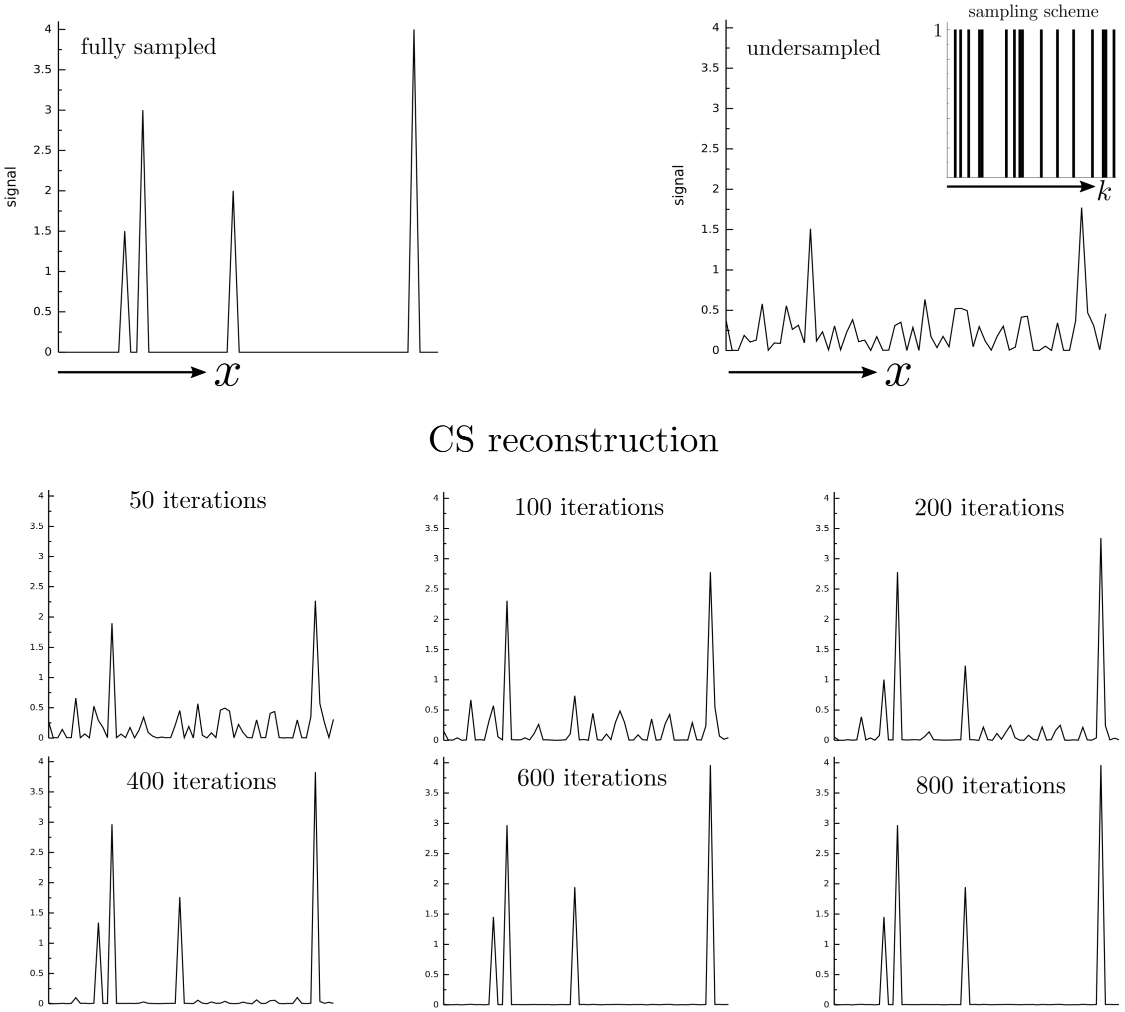

Figure 3.8: Reconstruction of a 1D data set with the iterative soft threshold algorithm. Undersampling the signal shown in the top left by a factor of R=4 leads to strong aliasing artifacts (top right). Reconstructed images for different numbers of iterations are shown below. The CS algorithm manages to suppress aliasing artifacts more and more, until the original signal is recovered.

3.3.3 Reconstruction via l_1 minimization

A different approach, as introduced to MRI by Lustig et al [7], formulates the CS reconstruction as the minimization problem

$$\min ||\Psi \boldsymbol{x}||_1, \tag{3.22}$$

where Ψ is the sparsifying transform and $\boldsymbol{x}$ is the image. The l_1-norm $||\boldsymbol{x}||_1 = \sum |x_i|$ delivers the sum of all pixel values and is not equal to the support of $\boldsymbol{x}$. However, minimizing this objective function also in many cases yields a sparse image [54]. The zero-norm, which computes the support of x and therefore is a more accurate measure of sparsity, cannot be used as it leads to infeasibly long computation times. The solution of the minimization also has to agree with the acquired data $\boldsymbol{y}$, so that the additional term

$$||E\boldsymbol{x} - \boldsymbol{y}||_2 < \epsilon, \tag{3.23}$$

is required in order to obtain solutions other than $\boldsymbol{x} = \boldsymbol{0}$. The data consistency (Eq. 3.23) is not assumed to be exact due to the presence of noise in the data. The last two equations form a constrained convex optimization problem. It can be rewritten in an unconstrained form

$$\text{argmin}_{\boldsymbol{x}} \left(||E\boldsymbol{x} - \boldsymbol{y}||_2^2 + \lambda ||\Psi \boldsymbol{x}||_1\right) \tag{3.24}$$

using a Lagrange multiplier λ. This equation leads to the same solution as Eq. 3.22 and 3.23 if λ is chosen appropriately. Equation 3.24 can be solved using a non-linear conjugate gradient algorithm. Details about an implementation of this algorithm can be found in [55]. In contrast to the iterative soft threshold algorithm, non-Cartesian sampling schemes can easily be implemented in the conjugate gradient calculations. A drawback of this method is however the additional parameter λ, that in many cases has to be chosen heuristically.

3.3.4 Discussion

In compressed sensing, the achievable acceleration factors are not limited by the number of coils, but merely by properties of the object that is investigated. This makes CS an interesting candidate also for settings, where pMRI cannot be applied due to the lack of receiver coil arrays with a high number of elements, as for example the case for many small animal systems. A challenge of compressed sensing is to identify a appropriate sparse base for each desired application. Also, many reconstruction algorithms require a parameter similar to the Lagrange multiplier λ used in l_1-minimization, that has to be chosen heuristically and may change for each different application and even for different patients. Last, CS reconstructions are usually computationally expensive. Nonetheless, compressed sensing reconstructions may prove very usefull, as in some cases very high acceleration factors may be achieved without a significant drop of SNR.

CHAPTER 4

Reducing Contrast Contamination in Radial Turbo Spin-Echo Acquisitions

4.1 Introduction

TSE imaging is an established fast multi-echo acquisition technique widely used in the clinic and in research. A TSE sequence applies multiple equidistantly spaced RF pulses to refocus the magnetization several times and significantly reduces measurement time when compared to a conventional spin-echo sequence (Chapter 2.3.3). For long repetition times (TR >> T_1) , the intensity of the pixel at location $\boldsymbol{x}$ for the nth echo is given by

$$I(\boldsymbol{x}, n) = PD(\boldsymbol{x}) \cdot \exp\left(-\frac{TE_n}{T_2(\boldsymbol{x})}\right) \tag{4.1}$$

and therefore comprises a combination of proton density and T_2 contrast depending on the specific position in the echo train. Nonetheless, as was shown in Figure 2.8, by careful reordering individual echoes of a Cartesian TSE acquisition into a single k-space it is still possible to obtain an image with a defined contrast. Using different reordering schemes in separate acquisitions allows the generation of the two clinically important proton density and T_2 weighted images. Despite the combination of data belonging to different echo times, Cartesian TSE images exhibit only insignificant artifacts connected with the T_2 decay of echo intensity over the duration of an echo train.

In clinical practice, Cartesian exams are performed almost exclusively due to their straightforward reconstruction. However, the general robustness of radial sampling strategies with respect to patient motion and flow has been demonstrated also in radial TSE (rTSE) acquisitions [56,57]. Additionally, radial sampling has further advantages in the particular case of a TSE acquisition. Each radial projection samples across the k-space center and collects both contrast- and high frequency information. Unlike in Cartesian acquisitions, contrast information is therefore available for all echo times TE_n. Hence, multiple images of different contrasts can be obtained from a single rTSE acquisition [56–59]. One way to reconstruct a series of aliasing-free images from a single rTSE data set is to use data sharing between projections from different locations in the echo train, for example with k-space weighted image contrast (KWIC, [60]).

For both Cartesian TSE images and radial TSE images reconstructed with KWIC, data belonging to different echo times are combined into a single image. Such a sharing of data from multiple contrasts may result in undesired mixed contrast contributions to the images. This is illustrated by an example shown in Figure 4.1. The digital proton density map and the corresponding T_2 values shown in the top row were provided by Brainweb [61–63]. A full set of spin-echo data were simulated for different echo times $\mathrm{TE}_n = n \cdot 8.8$ ms with $n = 1, 2, \ldots, 15$ according to equation 4.1. From the spin-echo data, Cartesian TSE and radial TSE data were generated. Images from the radial data were obtained using conventional KWIC reconstruction.

For the PD weighted images at an echo time of $8.8\,\mathrm{ms}$, a visible change of contrast occurs in the TSE images when compared to the spin-echo. Significant T_2 contributions appear in both the Cartesian and radial images. This is not the case for the T_2 weighted images, where only minor differences in contrast can be observed. An explanation for this effect is the generally strong contrast variation of different brain tissues in T_2 weighted images. This leads to a stronger influence on the contrast, when T_2 weighted data are used for the reconstruction of proton density images than in the reverse situation.

The effect of T_2 contributions to PD weighted TSE images grows with the strength of the magnetic field B_0 due to decreasing T_2 relaxation times and may reduce their diagnostic value. Today, this can be problematic especially at field strengths ≥ 3T. Similar effects can be observed for other data sharing techniques (such as keyhole, [64]) that are used to accelerate TSE data acquisition. The Motivation for the work presented in this chapter was to reduce undesired contrast contributions by reducing the bandwidth of KWIC in the reconstruction of radial TSE data.

To provide high flexibility, an adapted golden angle reordering scheme for rTSE acquisitions is presented. It allows a free choice of both the echo train length (ETL) and the bandwidth of the KWIC reconstruction. Undesired contrast contaminations from different contrasts in the characteristics of a single image are reduced by incorporating only data collected within a small temporal range of the desired echo time in KWIC. However, this also reduces the data available for each image and leads to both undersampled k-spaces and aliasing artifacts. In order to recover missing data and remove aliasing artifacts from the images, a conjugate gradient (CG) iterative SENSE reconstruction algorithm (Section 3.1.1) is applied. To remove residual aliasing artifacts as well as to improve SNR, temporal correlations present in the image series are exploited in a final step. Simulations and reconstructions of radial TSE brain data show greatly reduced contrast contamination when compared to conventional KWIC reconstruction or Cartesian TSE experiments.

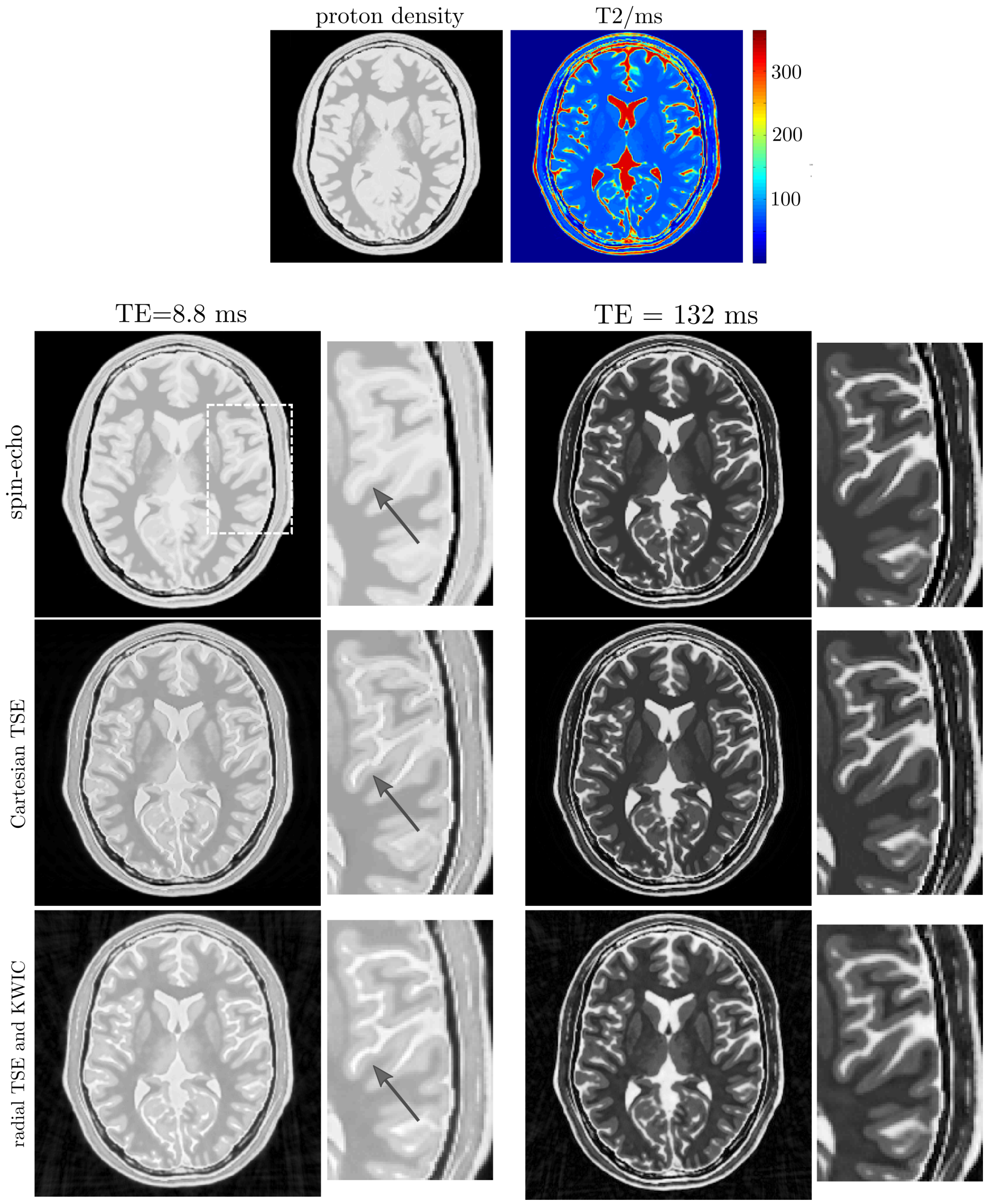

Figure 4.1: The impact of data sharing in proton density and T_2 weighted images for both Cartesian TSE and radial TSE with KWIC reconstruction. While in the simulated TSE proton density images, T_2 contributions are visible when compared to the spin-echo reference, the T_2 weighted images exhibit no significant differences.

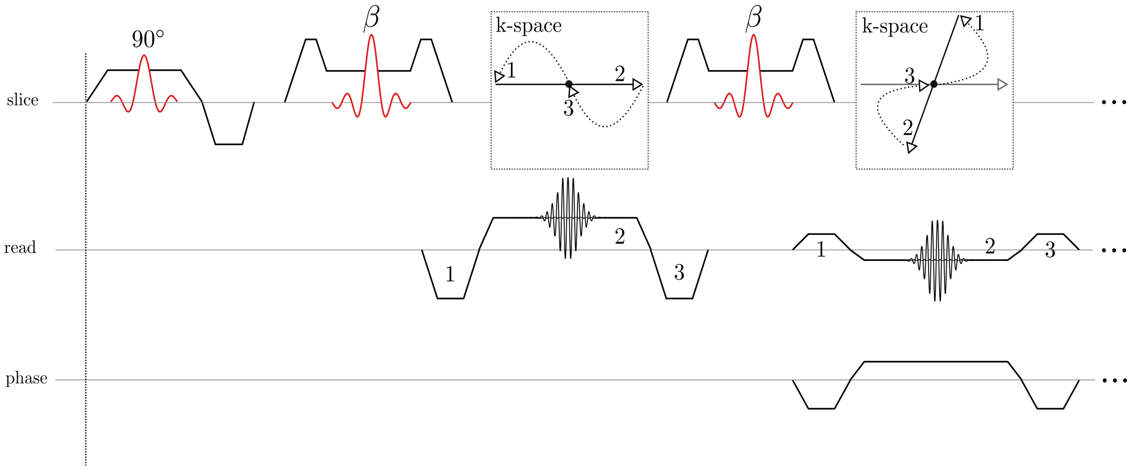

Figure 4.2: Diagram of radial TSE sequence

4.2 Methods

4.2.1 Radial TSE with adapted golden angle reordering

A TSE echo train can be combined with a radial sampling strategy in a straightforward manner. After each refocusing pulse, a radial TSE acquisition samples one projection across the center of k-space at a certain angle. A sequence diagram of the rTSE sequence used in this work is shown in Figure 4.2. To be able to freely increment the projection angles for subsequent echoes, the radial TSE sequence refocuses the magnetization before each RF pulse. Each individual projection in one echo train belongs to a different contrast. Hence, for each contrast both low- and high-frequency information are obtained. This can be exploited for the reconstruction of ETL images of different contrasts from a single radial TSE data set.

As explained in Section 2.4.1, projection reordering is an important parameter of radial sampling and has to be carefully considered for each application. In the case of a radial TSE acquisition, due to the different contrast information provided by the individual echoes of one echo train, existing reordering schemes have to be modified for optimal results. An ideal reordering scheme should provide a k-space sampling of maximal uniformity for every image contrast individually. In the proposed reconstruction, undersampled k-spaces are formed by using projections from a few neighbouring echoes in the echo train. A high flexibility in the choice of the amount of data used for each image and correspondingly the undersampling factors is desirable. Hence, the reordering scheme should additionally aim for a uniform k-space coverage using an arbitrary number of neighbouring echoes for reconstruction of a single image.

Previously, a projection reordering for rTSE measurements has been implemented based on the bit reverse operation [65] and reduced image artifacts were reported when compared to linear reordering. A drawback to bit-reversed reordering is the requirement for the echo train length (ETL) to be a power of two. In this work, a reordering scheme is developed based on the golden angle ratio due to its high flexibility in image reconstruction. A golden-ratio reordering was com-

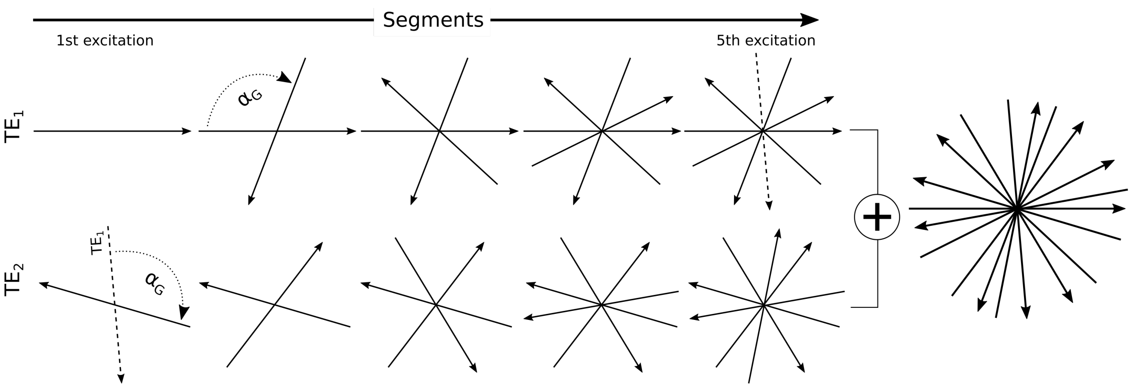

Figure 4.3: Modified golden angle reordering scheme for a radial TSE acquisition with an ETL of 2 and $\mathrm{N}_{Seg} = 5$ echo trains. The projection angle is increased by the golden angle α_G for subsequent segments, so that projections acquired at the same echo time are distributed according to the golden ratio. To guarantee golden ratio distribution for the whole set of projections, all projections belonging to TE_2 are rotated by $\mathrm{N}_{Seg} \cdot \alpha_G$ relative to those acquired at TE_1. For a bigger numbers of ETL, now even a subset of all acquired projections exhibit golden ratio sampling.

bined previously with rTSE acquisitions by increasing the projection angles linearly in a single echo train and by α_G for subsequent echo trains [66]. This guarantees that all the projections acquired at the same echo time are distributed uniformly according to the golden ratio.

To optimize sampling, the linear increment can be chosen in such a way that not only data from a single echo time are reordered according to the golden ratio, but also the combined data from an arbitrary number of adjacent echoes in the echo train. This can be assured by setting the linear increment for subsequent echoes in one echo train to $\Delta\alpha = \mathrm{N}_{Seg} \cdot \alpha_G$, where N_{Seg} corresponds to the number of excitations. Hence, the angle for any projection in the rTSE acquisition can be calculated according to

$$\alpha(\mathrm{Echo}, \mathrm{Seg}) = (\mathrm{Echo} \cdot \mathrm{N}_{Seg} + \mathrm{Seg}) \cdot \alpha_G, \tag{4.2}$$

where Seg = $(0, 1, \ldots, \mathrm{N}_{Seg} - 1)$ is the current segment and Echo = $(0, 1, \ldots, \mathrm{ETL} - 1)$ is the position in the echo train. The modified reordering is depicted in Figure 4.3 for ETL = 2 and 5 segments (i.e. number of excitations). It leads to a distribution of projections according to the golden ratio using an arbitrary number of different adjacent echoes for reconstruction. This reordering is optimal when the total number of segments is chosen to be a Fibonacci number, but no restrictions are made towards the echo train length.

4.2.2 Data processing

If a sufficient amount of data was acquired in a radial TSE acquisition, fully sampled images could be reconstructed at each TE. This corresponds to a multi spin-echo (MSE) acquisition for Cartesian sampling and has the major drawback of prohibitively long scan times. An acceleration of the acquisition can be achieved by reducing the total number of echo trains N_{Seg} and correspondingly the total number of projections. However, using only the data belonging to the accurate contrast for reconstruction in this case leads to undersampled k-spaces and aliasing artifacts in the images.

A KWIC reconstruction [60] allows data sharing for radial data, that are composed of different contrasts but share the same high frequency information. Consider an arbitrary fully sampled radial data set. Due to the nature of radial sampling, the center region of k-space is highly oversampled. This is exploited by a KWIC reconstruction to generate multiple fully sampled images of different contrast from one fully sampled multi-contrast radial data set. A typical KWIC reconstruction for radial TSE data is shown in Figure 4.4 a). Here, k-space is divided into annular rings. Only data from the desired echo time is used to fill the center region, which is primarily responsible for the image contrast. This also means that only from those projections all data points are used. For all outer regions, remaining gaps in k-space are filled with data closest to the desired echo time. As the gaps increase in size with the distance from $\boldsymbol{k} = 0$, more data with inaccurate contrast information have to be used. This reconstruction scheme can be applied to numerous applications and mostly results in images with only insignificant aliasing artifacts, but contamination from undesired contrast information.

In order to reduce mixed contrast contributions to the reconstructed images, it is necessary to use fewer data with undesired contrast information. For radial images reconstructed with KWIC, this can be achieved in two different ways. A first possibility is to only use the more accurate projections for reconstruction, hereby discarding a part of all acquired data. This corresponds to a narrower KWIC filter bandwidth. Secondly, the KWIC filter can be modified to remove more data points at the center of projections exhibiting an undesired contrast. Here, a combination of both methods is proposed as shown in Figure 4.4 b). An exemplary narrow-band KWIC filter is depicted for contrast corresponding to the 6th echo of a rTSE acquisition with $\text{ETL} = 15$. Due to the large amount of data omitted by narrowing the KWIC filter band, this leads to an undersampled k-space and aliasing artifacts in the image. Obtaining a fully sampled k-space is infeasible due to the long acquisition times necessary. Instead, missing data points can be recovered using (among others) one of the reconstruction algorithms presented in Section 3. In this work, parallel imaging in form of the conjugate gradient SENSE algorithm [6] introduced in section 3.1.1 was chosen due to its ability to reconstruct arbitrarily sampled data and its stable convergence properties. As with all parallel imaging methods, after reconstruction enhanced noise and some artifacts may remain. However, additional correlations between the images may be exploited to further improve SNR and to remove residual artifacts.

The bandwidth of the KWIC filter influences both the resulting image contrast and the degree of aliasing and has to be tailored to individual applications. In the case of radial TSE data, a fast change of image contrast occurs during the first few echoes. Therefore, only a small number of adjacent echoes may be used to still obtain images with an accurate proton density contrast. The complete proposed reconstruction for radial TSE data is illustrated in Figure 4.5. A narrow-band KWIC filter using the data of three adjacent echoes is used to reconstruct one image at each echo time. As will be shown later, this provides both a small enough temporal window to retain an accurate contrast and a sufficient amount of data for image reconstruction. Each k-space is undersampled and the corresponding images exhibit aliasing artifacts. The KWIC filtered data at each TE is then used directly as input for a CG-SENSE reconstruction. The coil sensitivity

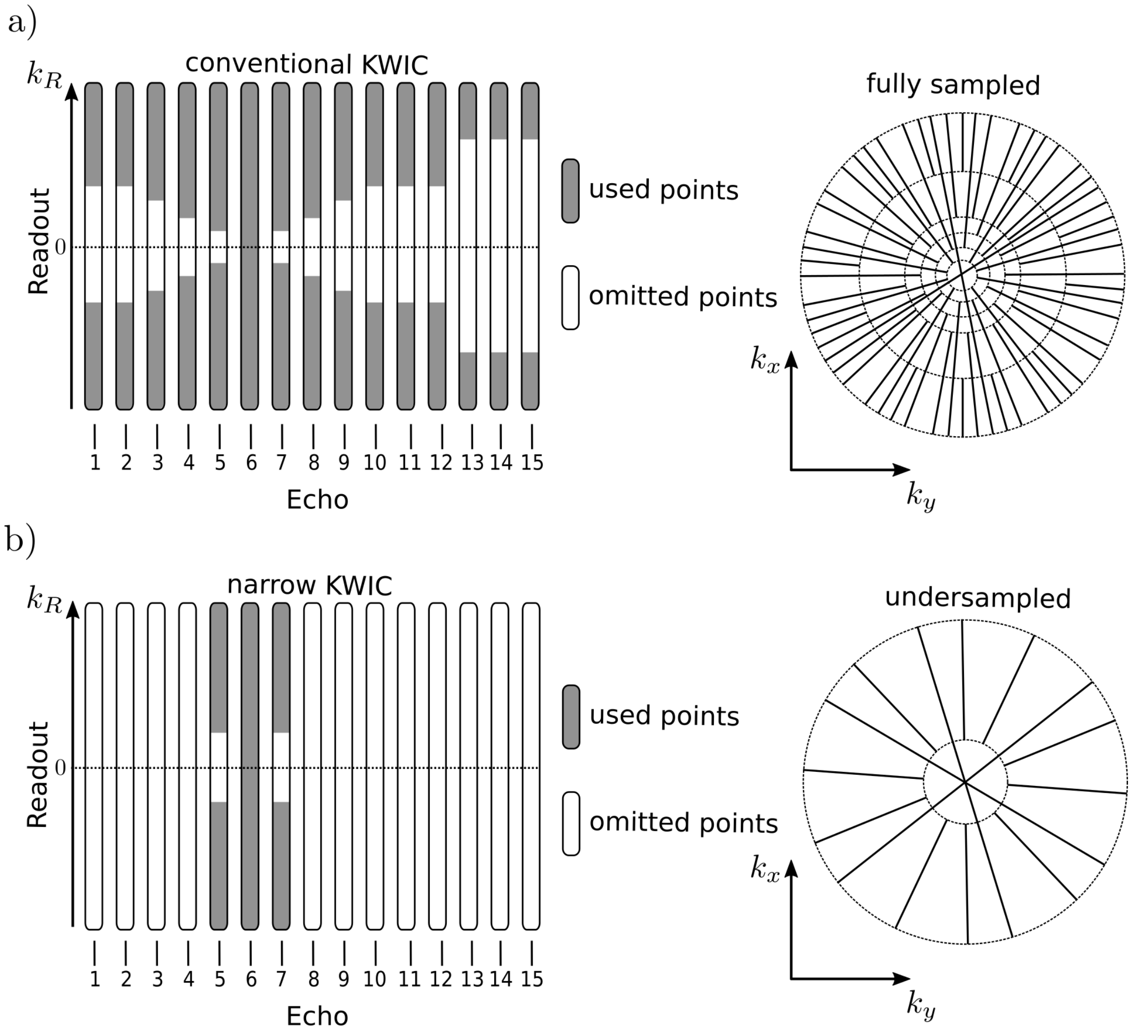

Figure 4.4: Conventional (a) and narrow bandwidth (b) KWIC reconstruction for radial TSE data. In conventional KWIC, data from all echo times are employed for reconstruction, which leads to a fully sampled k-space shown to the right. In the example narrow KWIC filter illustrated below, only three of the whole train of 15 echoes are used for reconstruction to reduce the contributions of unwanted contrasts. Additionally, more data at the center of each projections adjacent to the desired echo time are removed. If the number of segments is not increased, the corresponding k-space will be undersampled which in turn leads to aliasing artifacts in the image.

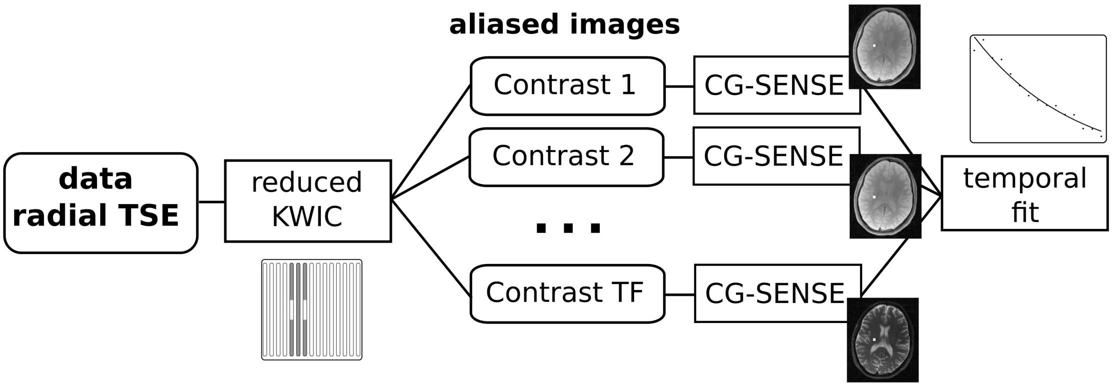

Figure 4.5: Schematic diagram of the complete reconstruction of radial TSE brain data. Applying a narrow KWIC filter leads to a number of ETL aliased images. Subsequently, a CG-SENSE reconstruction is performed. Finally, noise and residual aliasing artifacts are reduced enforcing an exponential decay in each voxel.

information required by CG-SENSE can be obtained by gridding the full radial TSE dataset and performing array correlation statistics [67]. The temporal behavior of the signal of one voxel across the image series approximately follows a mono-exponential decay. Noise and residual artifacts introduce deviations from this signal evolution. Hence, to improve image quality, this relation is enforced for the reconstructed images by performing a pixel-wise fit in accordance with

$$I(\boldsymbol{x},t) = PD(\boldsymbol{x}) \cdot \exp - \frac{t}{T_2(\boldsymbol{x})}. \tag{4.3}$$

Using the results for PD and T_2 in each pixel, synthetic images can subsequently be obtained at each desired echo time.

All gridding and degridding operations were performed using non-uniform Fourier transform [33, 68]. Density compensation was applied with the method proposed by Bydder et. al. [38].

4.2.3 Simulations

Each step of the proposed reconstruction was simulated using the digital spin density map and the corresponding T_2 values of matrix size 256×256 shown in Figure 4.1. A Cartesian image series was obtained from Equation 4.1 with an echo spacing of $8.8\,\mathrm{ms}$ and modified with a simulated 12-channel coil sensitivity profile. A fully sampled radial MSE data set was synthetically generated with 510 projections per image and golden angle reordering. A radial multi-contrast data set with the modified reordering was assembled from the MSE data, corresponding to a TSE acquisition with ETL = 15 and 34 segments. After adding uncorrelated complex Gaussian noise, images were obtained using the proposed reconstruction depicted in Figure 4.5. Data from three different echoes in the echo train, corresponding to a total of 102 projections, were used for the reconstruction of each image. To obtain SNR information of the reconstruction, the whole process was repeated 100 fold [69]. For every pixel x of each image at an individual echo time, SNR was estimated by

$$\mathrm{SNR}(x, \mathrm{TE}_i) = \frac{\mathrm{mean}(I(x, \mathrm{TE}_i, n))}{\mathrm{std}(I(x, \mathrm{TE}_i, n))}, \tag{4.4}$$

where $I(x, TE_i)$ is the signal intensity of the n = 100 reconstructed images at the echo time TE_i.

4.2.4 In vivo experiments

All in vivo experiments were performed on a standard clinical scanner (Skyra, Siemens Healthcare, Erlangen, Germany) with a field strength of 3T using a 32 channel head receiver array. Written consent was obtained from all volunteers prior to the imaging session. Two different sets of brain data of two healthy volunteers were acquired using a radial TSE sequence with the modified golden angle reordering. For an optimal distribution of the projections, 34 excitations (= Fibonacci number) were performed. With an ETL of 15, this corresponds to a total number of 510 projections. A temporal echo-spacing of 8.8 ms and a repetition time of TR = 5 s leads to a total acquisition time of 2:50 minutes for the single-slice experiments.

One rTSE data set was acquired in an axial orientation with a field of view of 200 × 200 mm^2, a matrix size of 256×256, and a slice thickness of 4 mm. For comparison, a radial multi spin-echo dataset was obtained using the same sequence with a total number of 293 projections per image but otherwise identical parameters. Furthermore, Cartesian TSE data sets with the same measurement parameters were obtained with echo times of 8.8 ms and 132 ms corresponding to the first and last echo of the rTSE measurement.

An additional, high resolution rTSE data set was acquired in a sagittal orientation with a matrix size of 384×384 and a field of view of 220 × 220 mm^2. Due to the higher readout gradient amplitude at higher resolution, the echo-spacing was increased to 9 ms. For comparison, two Cartesian TSE data sets of matrix size 384×384 were obtained at echo times of 9.9 ms and 99 ms.

For each data set, the reconstruction depicted in Figure 2 was performed applying 8 iterations of CG-SENSE. In order to reduce reconstruction time, the number of channels were compressed to 12 via principal component analysis [70, 71]. For each image of the series, 102 projections were used belonging to the 3 nearest echoes. To investigate the impact of the bandwidth of the KWIC filter, additional reconstructions were performed from the high-resolution data set using 1, 5 and 7 adjacent echoes in each image. For comparison, an image series was obtained with conventional KWIC reconstruction using all available data.

4.3 Results

4.3.1 Simulations

Figure 4.6 displays reconstructed images from the simulated rTSE data for both PD contrast (top row) and with strong T_2 weighting (bottom row). Images with a pure spin-echo contrast are

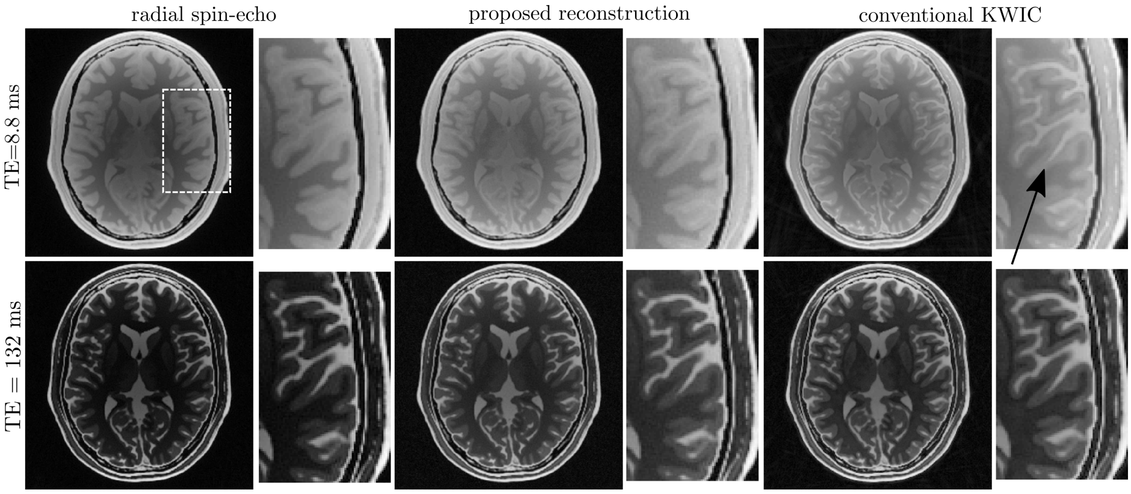

Figure 4.6: Comparison of radial images with a spin-density contrast (left) to images obtained with a narrow bandwidth (middle) and conventional (right) KWIC-filter.

shown on the left hand side. The proton density image obtained with a narrow-band KWIC filter (middle) exhibits no visible T_2 contributions. This is not true for conventional KWIC (right), where significant T_2 characteristics appear in the image as indicated by the arrows. The T_2 weighted images exhibit a similar contrast in all cases. No remaining aliasing artifacts can be observed.

Figure 4.7 depicts the SNR performance of the individual steps of the reconstruction. SNR maps of both PD and T_2-weighted images are shown on top for radial MSE images reconstructed from 510 projections (left) and for images reconstructed from a rTSE data set with a narrow-band KWIC filter before (middle) and after (right) the mono-exponential fit. Exploiting the temporal correlations between the images after the parallel imaging reconstruction leads to a significant increase of SNR. This can also be seen from the mean SNR plotted over each individual TE. The highest gain can be achieved for the central images.

4.3.2 In vivo experiments

In Figure 4.8, images obtained with a MSE acquisition (row 1), with a Cartesian TSE (row 2) and with a radial TSE are compared for both proton density weighting (left column) and T_2 weighting (right column). Images from the radial TSE data set are shown that were reconstructed with conventional KWIC using all projections (row 3) and the proposed combination of a narrow KWIC filter and CG-SENSE (row 4). The image resolution is 0.78 × 0.78 mm^2. In the proton density images, undesired T_2 contrast contributions are visible in both the Cartesian TSE and the standard KWIC images as indicated by the arrows. Contributions of unwanted contrast can also be observed in the T_2 weighted images, although less apparent. These contributions are strongly reduced in the images reconstructed with a narrow-band KWIC filter, which in both cases exhibit a similar contrast to the MSE images.

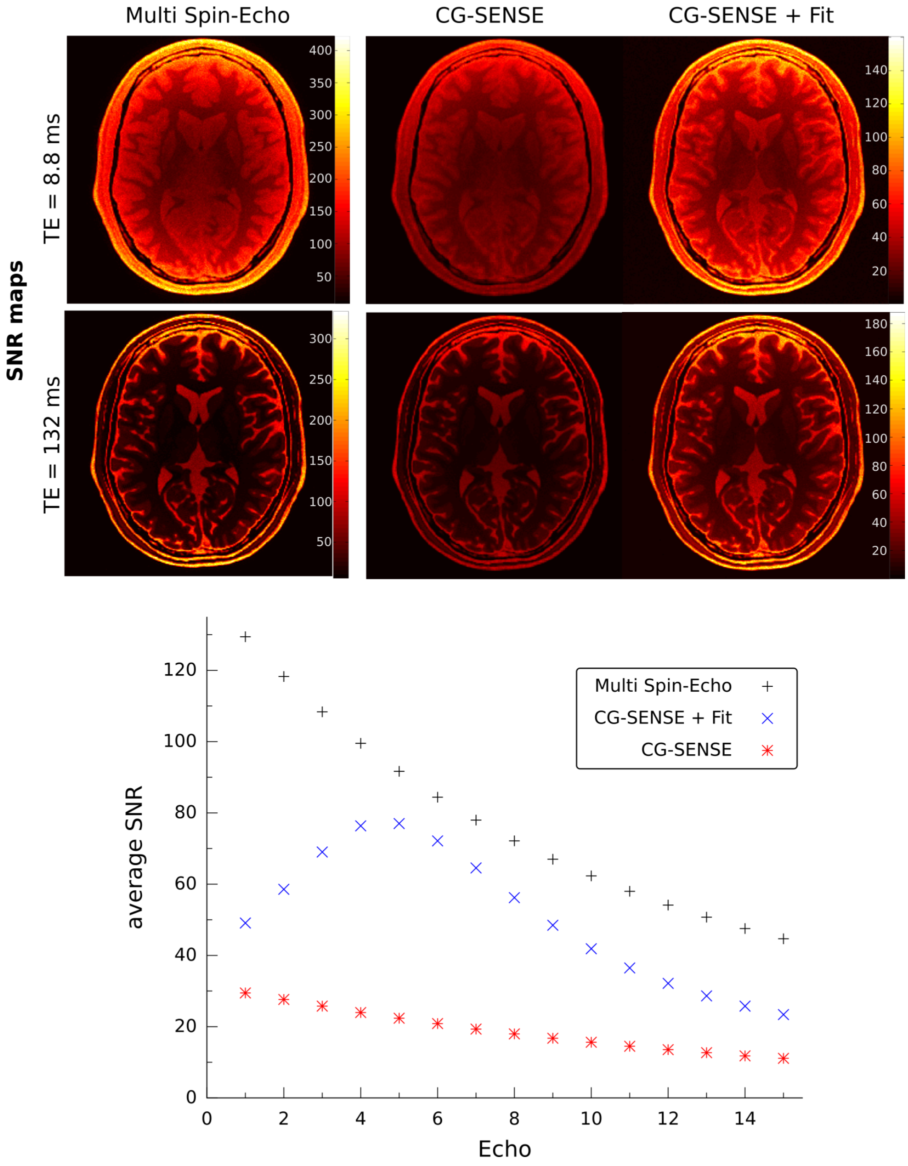

Figure 4.7: SNR performance of the reconstruction. Compared to the MSE acquisition, images obtained with narrowband KWIC and CG-SENSE show a decrease in SNR due to fewer available data and the parallel imaging reconstruction. Applying an additional temporal fit results in increased SNR.

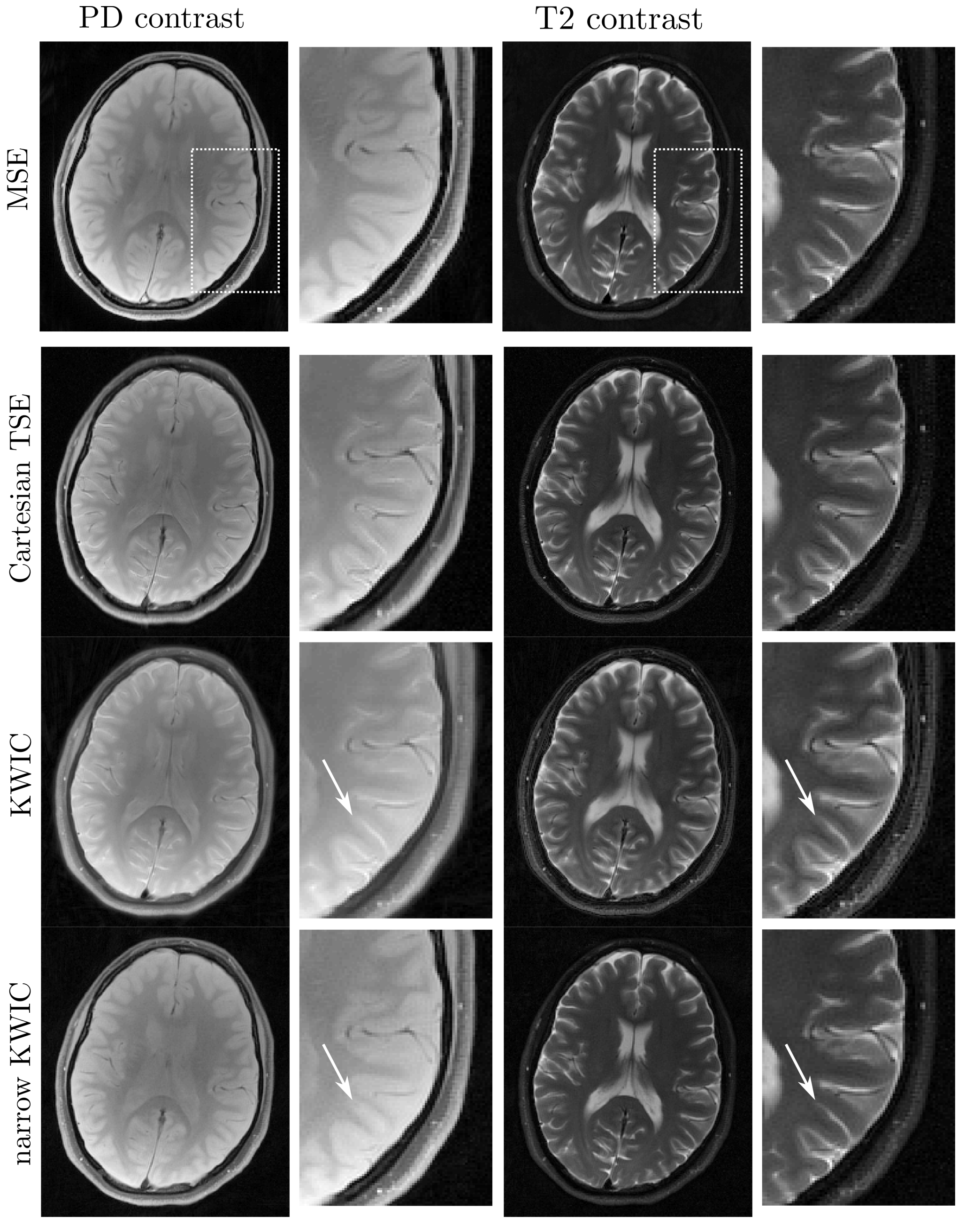

Figure 4.8: Proton density (PD) and T_2-weighted images of the brain of a healthy volunteer obtained with a multi spin-echo (MSE) acquisition, a standard Cartesian TSE acquisition and a radial TSE acquisition applying both conventional KWIC and a narrow-band KWIC filter for reconstruction. In the Cartesian TSE and KWIC images, mixed contrast contributions are visible (see arrows) in the PD weighted images.

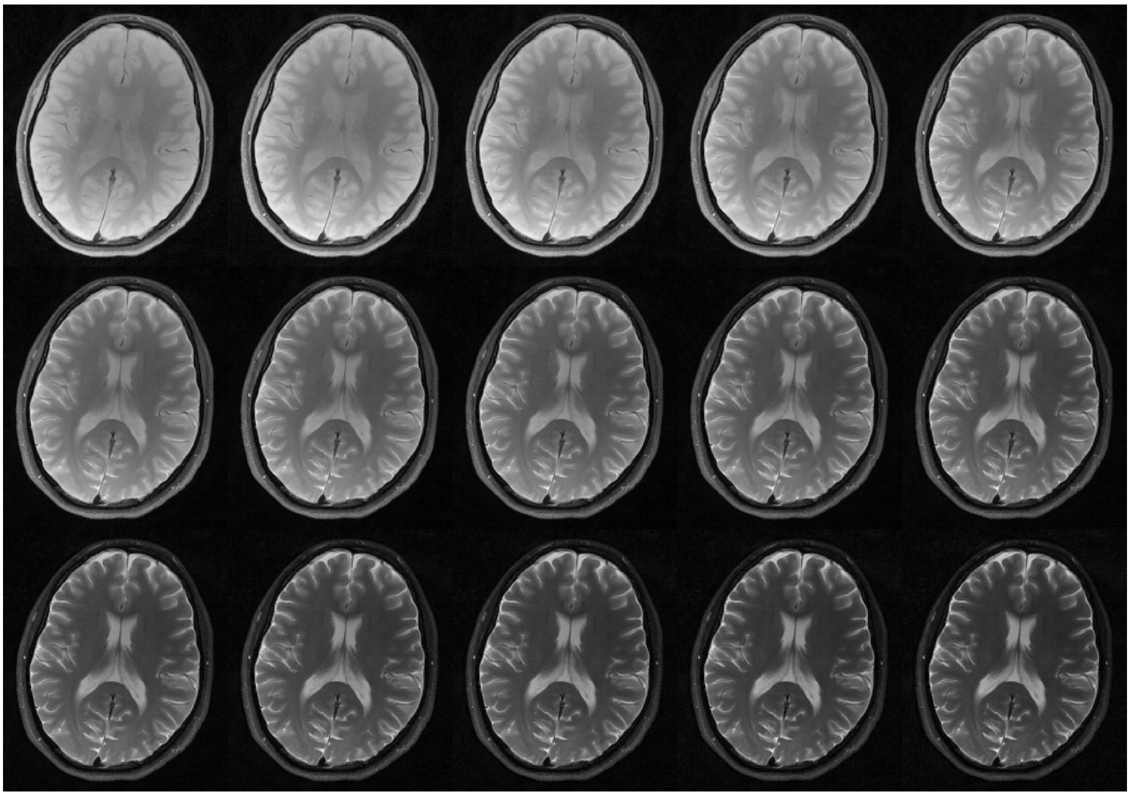

Figure 4.9: Complete image series of 15 different contrasts with an echo spacing of 8.8 ms obtained with a single radial TSE measurement (510 projections) using the proposed method for reconstruction.

Figure 4.9 shows the entire image series of 15 different contrasts obtained from a single rTSE measurement. A fast change in contrast during the first few images of the series can be observed. No streaking artifacts are visible.

Figure 4.10 demonstrates the impact of the filter bandwidth on images reconstructed with CG-SENSE. Proton density weighted high-resolution images are shown reconstructed using KWIC filter bandwidths from one to seven echoes. Images reconstructed from only one echo reveal significant remaining aliasing artifacts. Using three echoes, few aliasing artifacts remain with no significant change in image contrast. Using more data for the reconstruction leads to a higher SNR but also to significant unwanted T_2 contrast contributions to the PD weighted images.

In Figure 4.11, high-resolution Cartesian and radial TSE brain images (0.57×0.57 mm^2 isotropic) of matrix size 384×384 for both PD and T_2-weighted contrasts are shown. Pulsating flow in the occipital artery at the back of the head leads to significant flow artifacts in the Cartesian images, which is highlighted by the arrow. These artifacts are not present in the images obtained with radial sampling. After the CG-SENSE reconstruction of the radial narrow-band KWIC data, some aliasing artifacts remain. Those artifacts are greatly reduced after exploiting the temporal correlation between the single images by applying a pixel-wise mono-exponential fit.

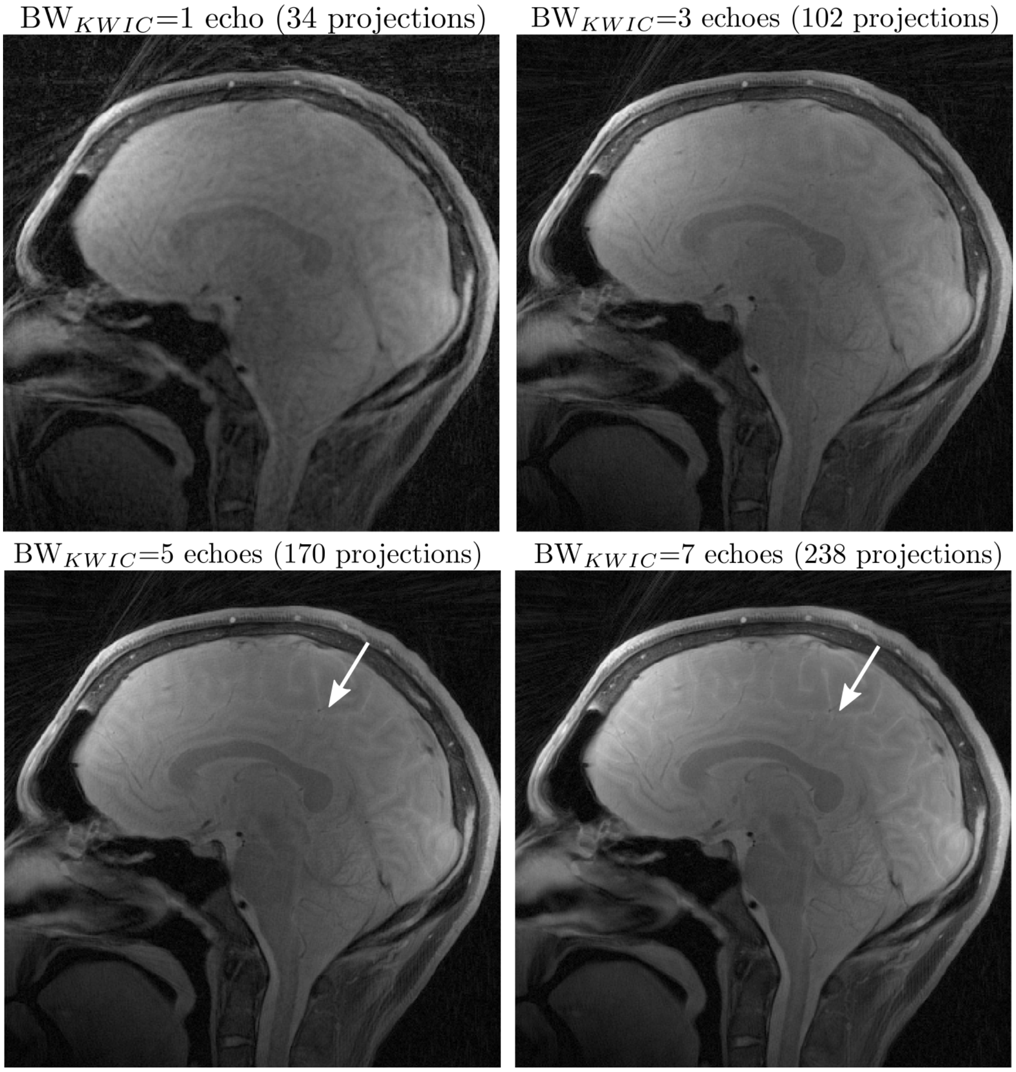

BW$_{KWIC}$=1 echo (34 projections)

BW$_{KWIC}$=3 echoes (102 projections)

BW$_{KWIC}$=5 echoes (170 projections)

BW$_{KWIC}$=7 echoes (238 projections)

Figure 4.10: Impact of the filter bandwidth on the image contrast. PD images are shown reconstructed with CG-SENSE from different amounts of data.

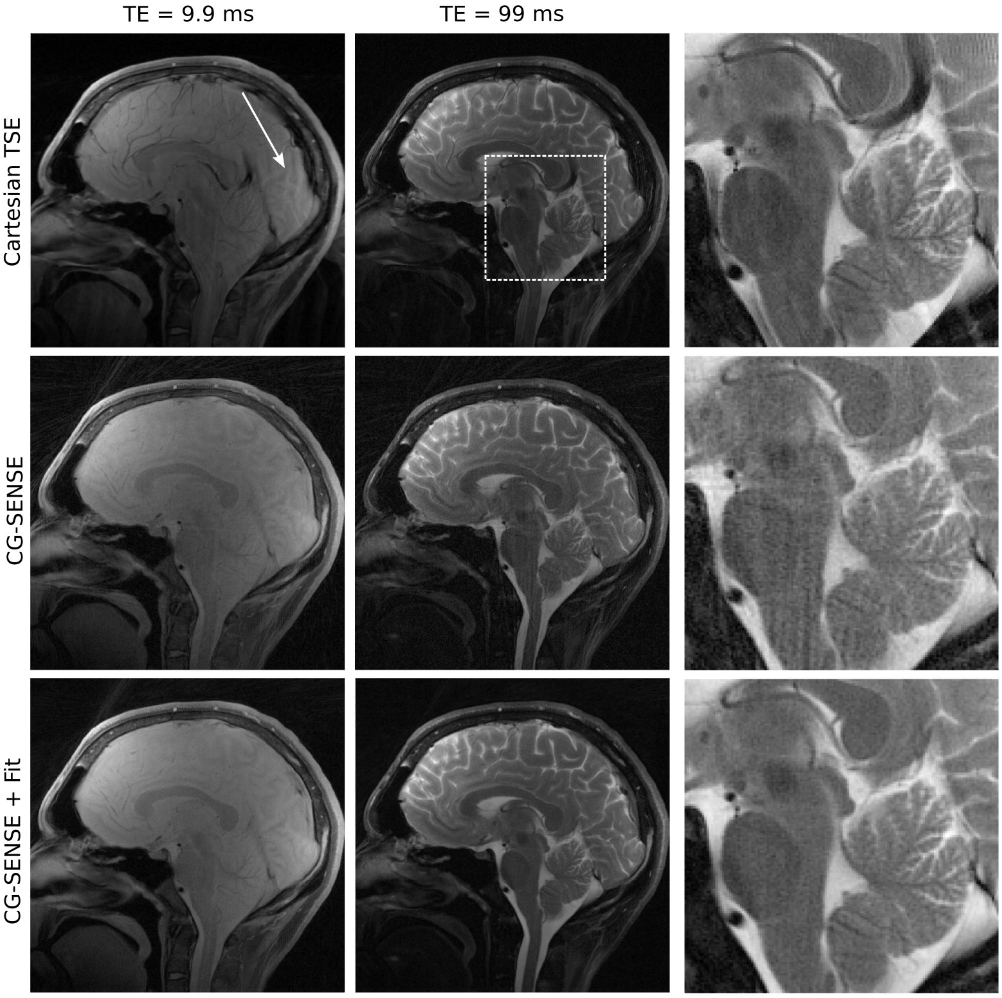

Figure 4.11: Sagittal brain images of a healthy volunteer, obtained with a radial TSE acquisition. PD and T_2 weighted images are shown both before and after the final fitting step. After the CG-SENSE reconstruction, some remaining aliasing artifacts can be observed.

4.4 Discussion and Conclusion

Using a KWIC reconstruction, multiple images with different contrasts can be reconstructed from a single rTSE data set. The images exhibit a contrast very similar that of multi spin-echo images. This is especially true for T_2 weighted images. However, some important differences can be observed. To obtain unaliased images, KWIC uses data sharing from different echo times. Especially in PD weighted images, undesired T_2 contrast contributions are the consequence. This is also true for Cartesian TSE images. In both cases, no true PD contrast can be obtained. The impact of this effect increases with the strength of the main field due to smaller relaxation times T_2. However, avoiding this data sharing requires a conventional spin-echo acquisition with prohibitively long measurement times.

The proposed method exploits the flexibility of radial sampling to greatly reduce the amount of shared data in each image while keeping scan times short. For each reconstructed image, only data with at least a similar contrast are used. Fewer data result in images, that with reduced SNR and aliasing artifacts. With the specific KWIC-filter used in this work for the radial data set of 510 projections, the undersampling factors are R = 2.8 and R = 4.0 when compared to data sets with 256 projections (matrix size 256) and 384 projections (matrix size 384) respectively. When compared to two separate Cartesian TSE acquisitions to obtain both the clinically important PD and T_2 weighted images, a reduced measurement time by 5.5% (256 projections) and 34.6% (384 projections) can be reported.

To allow a high flexibility in the choice of data used for the reconstruction of a single image, a modified golden-ratio sampling scheme optimized for TSE sequences was presented. It guarantees a distribution of projections according to the golden ratio both for data belonging to a single echo time as well as the combined data from an arbitrary number of adjacent echoes. Furthermore, in contrast to existing schemes it poses no restrictions on the length of the echo train.

Aliasing artifacts in the images are removed with the CG-SENSE algorithm. For different applications, other parallel imaging- or compressed sensing methods may be applied. The 32 channel coil array employed for data acquisition allows high quality parallel imaging reconstructions at the moderate acceleration factors used in the shown examples. A further reduction of residual aliasing artifacts and an increase of SNR can be achieved by exploiting temporal correlations between the individual images of the complete series. In the case of a TSE acquisition, the approximate signal evolution is known and a pixel-wise mono-exponential is used. As is to be expected, the fit is more robust for the center images of the image series, where the simulation shows a SNR gain of up to 250% when compared to the reconstruction employing CG-SENSE only. For the images with proton density or maximal T_2 contrast, a SNR gain of over 70% can still be observed. For other applications, different correlation methods such as a principal component analysis could be performed, which is not model-dependent and computationally fast. In this work, all individual steps of the reconstruction were implemented in Matlab. With optimization, such as GPU implementations [72], it may be possible to push the reconstruction time well below 10s per slice.

An important parameter of the reconstruction is the bandwidth of the KWIC filter. It controls the trade-off between mixed-contrast contributions to the images and the severity of the aliasing artifacts in the images. Therefore, it has to be adjusted for different applications depending on the dynamics of the data and the capability of the reconstruction algorithm. In the examples shown in this work, a filter-width of more than 3 echoes already led to visible T_2 contributions in the proton density images. On the other hand, a width smaller than 3 led to significant aliasing artifacts that could not be removed by the CG-SENSE algorithm.

In conclusion, the proposed reconstruction is a combination of a narrow-band KWIC filter and parallel imaging and generates images with different contrasts from a single radial TSE data set. The resulting image contrast is very close to the contrast of a (multi) spin-echo acquisition. This is a major improvement, especially over the commonly used Cartesian TSE proton density images, where significant T_2 contributions to PD weighted images may appear. The combination of the presented acquisition and reconstruction scheme could be an important step towards implementing radial TSE in clinical practice. It poses no restriction on the echo train length and uses combination of existing and established methods, which can be highly parallelized and are already implemented on modern clinical scanners.

CHAPTER 5

Accurate T_2 estimates from MSE acquisitions

5.1 Motivation

One of the most important tissue properties for the detection of pathologies with MRI is the T_2 relaxation time. In clinical routine, it is mostly used for the generation of images with a contrast that is a function of T_2. For the example of a conventional spin-echo acquisition with long repetition times, the signal in a pixel at location $\boldsymbol{x}$ is given by

$$S(\boldsymbol{x},t) = PD(\boldsymbol{x}) \cdot \exp(-\frac{t}{T_2(\boldsymbol{x})}) \tag{5.1}$$

and hence depends on both proton density and T_2. Other sequences such as bSSFP- or spin-echo acquisitions with a short TR provide a contrast that additionally depends on T_1. However, for applications such as tissue characterization and the detection of certain diseases [73–78], in some cases it is not sufficient to obtain images with a particular contrast but knowledge about the actual value of the T_2 relaxation time is required.

Gold standard for T_2 quantification is the acquisition of an image series with a multi spin-echo (MSE) acquisition, as a more accurate single spin-echo acquisition leads to infeasibly long scan times. MSE sequences use a train of refocusing pulses identical to a TSE acquisition. However, in contrast to TSE experiments, where data from all echoes are combined into a single image, a fully sampled image is acquired at every echo time. Using a perfect refocusing pulse with a flip angle of 180°, the signal evolution in one pixel is given by Eq. 5.1 and therefore is equal to that

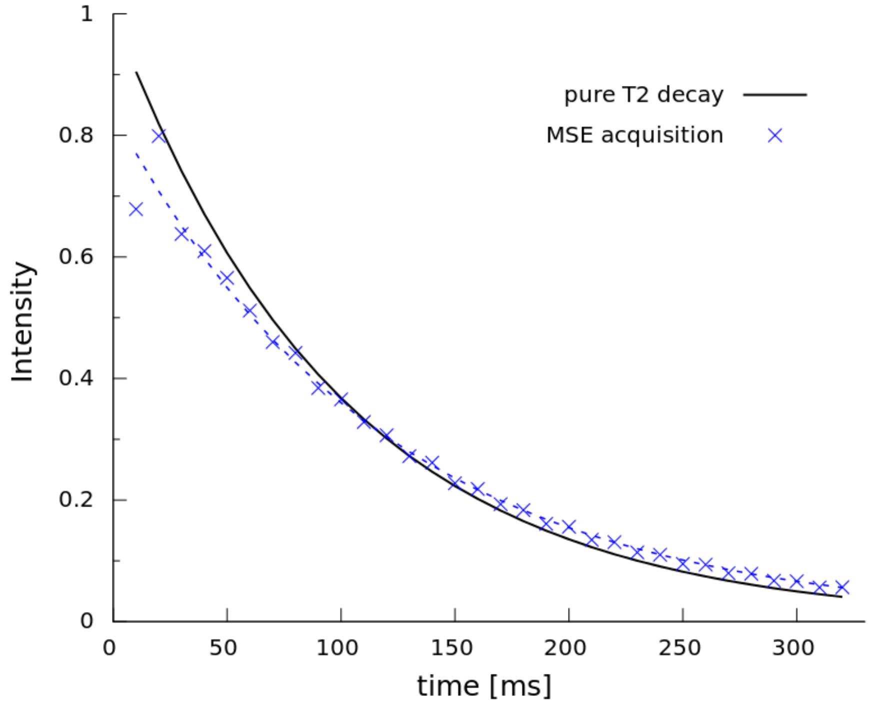

Figure 5.1: Signal time-course of a SE acquisition shown for refocusing pulses with flip angles of 180° (solid line) and for refocusing pulses with a reduced flip angle of 120°. In practice, the ideal signal evolution can never be achieved.

of a single spin-echo acquisition. A fully sampled image is obtained at every echo time TE and a T_2 map can be derived by using a simple pixel-wise mono-exponential fit. In practice, however, a perfect flip angle of 180° is impossible to achieve for several reasons. Due to a finite pulse duration, the slice profile of RF pulses deviates from the ideal box function. Further deviations from the desired flip angle arise due to (spatially varying) imperfections of B_1. At higher field strengths of the main magnetic field, nominal refocusing flip angles lower than 180° might even be desirable due to limits for the specific absorption ratio (SAR).

Using a refocusing flip angle of lower than 180° gives rise to a modified signal evolution. The main reason are stimulated echo contributions, which are a result of encoded magnetization that is temporarily moved onto the z-axis and are explained in more detail below. Figure 5.1 shows the simulated signal evolution for a MSE sequence with TF = 32, echo spacing = 10 ms, T_2 = 100 ms, T_1 = 3000 ms and flip angles of 120° (dashed line) and 180° (solid line). A typical characteristic of a signal evolution with significant stimulated echo contributions is the hyper-intense second echo and a prolonged decay constant. This leads to errors in T_2 values derived from this signal time-course. In the example shown, the T_2 value obtained with a mono-exponential fit exhibits a 18% increase from the actual value.

In this chapter, a method is introduced that calculates a correction factor for T_2 values obtained via a mono-exponential fit of conventional MSE data. This correction factor is obtained using the extended phase graph (EPG) formulation [23, 24] and depends on sequence parameters such as echo train length (ETL) and echo spacing (ESP) as well as the flip angle of the refocusing pulses and T_2. All parameters required by the method are hereby extracted from the MSE data itself, so that no additional acquisitions are necessary. The accuracy of the method is investigated in simulations for different excitation and refocusing slice profiles as well as for varying noise levels. The simulations are confirmed with phantom experiments for different nominal refocusing flip angles by comparing the results to those obtained with SE acquisitions. A part of the content of this chapter was taken from the first manuscript listed on Page 121, which was submitted to the journal 'Magnetic Resonance Materials in Physics, Biology and Medicine' for publication.

5.2 Methods

5.2.1 Extended Phase Graphs

The extended phase graph (EPG) formulation introduced by Jürgen Hennig [23, 24], is a convenient way to predict the occurrence and intensity of echoes in sequences with multiple RF pulses. In EPG, the complete magnetization at a particular time point is segmented into so called configurations. A configuration is a subset of the total magnetization that exhibits the same level of coherence and is classified by the gradient moment it has experienced. Each RF pulse splits each configuration into three new configurations. One of the resulting configurations (under the influence of gradients) dephases, one rephases and may lead to an echo and one is aligned with the longitudinal axis and therefore maintains its current state. The percentage of the total magnetization contained in each configuration is determined by the flip angle value of the pulse.

Figure 5.2 shows an example phase graph for a double spin-echo sequence. Depicted is the state of coherence of each configuration (vertical axis) over time (horizontal axis). Generally, dephasing configurations (i.e. increasing decoherence) are located above the axis, rephasing configurations (i.e. decreasing decoherence) below. Longitudinal configurations are depicted as horizontal (dashed) lines. A configuration crossing the temporal axis corresponds to an echo in the sequence. Applied to a completely relaxed system, the excitation pulse produces a single dephasing configuration. Each of the refocusing pulse splits this configuration into three parts and generates two echoes. While the first echo is a pure spin-echo, the second echo exhibits contributions from both the longitudinal configuration and the spin-echo, as indicated by the green color.

Stimulated echoes and MSE/TSE

Echoes stemming from encoded magnetization on the longitudinal axis are known as stimulated echoes. For a MSE/TSE acquisition, stimulated echoes can make up a significant share of the total signal intensity. In contrast to transversal magnetization, encoded longitudinal magnetization (and consequently the intensity of stimulated echoes) decays with T_1 instead of T_2. As T_1 is greater than T_2 for common tissue types, stimulated echoes usually prolong signal decay. Even when refocusing pulses with nominal flip angles of 180° are used, stimulated echoes occur due

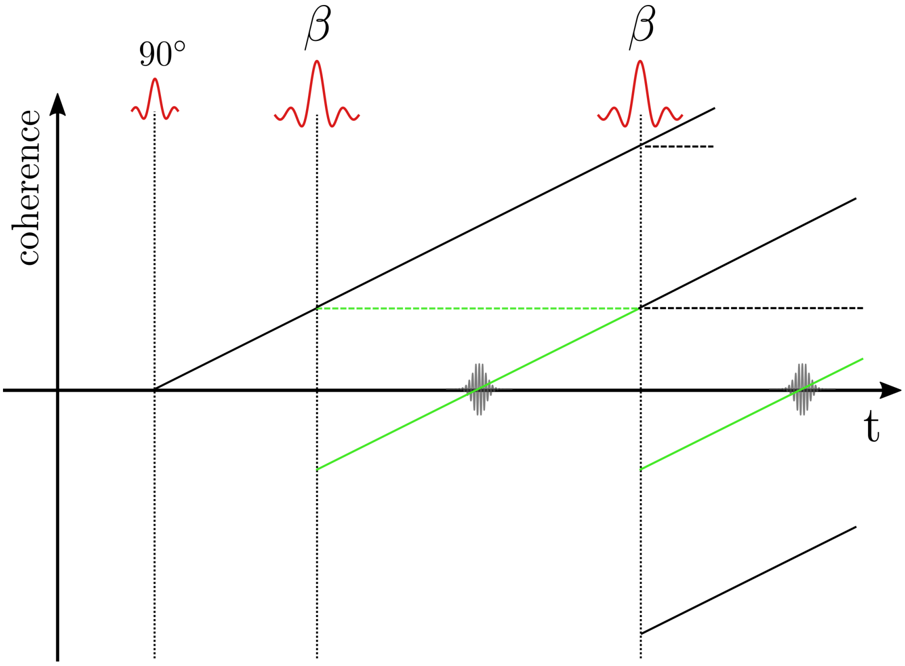

Figure 5.2: Extended phase graph of a double echo sequence. The paths leading to the second echo are depicted in green.

to technical imperfections such as slice profile deviations, inaccurate calibration and B_1 inhomogeneities. As consequence, using a MSE acquisition for T_2 quantification usually leads to higher results than the actual values.

The EPG-formalism can not only be used to predict the occurrence of echoes but also to quantify the contributions from different echo paths and to calculate the signal intensity of each echo. The exact representation of the rotation matrices between the individual configurations caused by RF pulses can be found for example in [79]. For a MSE acquisition using ETL echoes with a temporal spacing of ESP and a fixed flip angle β of the refocusing pulses, the signal magnitude $\boldsymbol{S}(\boldsymbol{x}) \in \mathbb{R}^{\mathrm{ETL}}$ for all echoes in the image pixel located at $\boldsymbol{x}$ is given by

$$\boldsymbol{S}(\boldsymbol{x}) = S_0(\boldsymbol{x}) \cdot \boldsymbol{EPG}\Big(\beta(\boldsymbol{x}), \mathrm{ESP}, T_1(\boldsymbol{x}), T_2(\boldsymbol{x})\Big). \tag{5.2}$$

Hereby, $\boldsymbol{EPG}$ cannot be expressed as an analytical function but has to be calculated numerically. As all parameters other than ESP may exhibit a spatial dependency, the calculations have to be performed separately for each image pixel.

5.2.2 Correction for stimulated echoes

The gold standard for T_2 quantification using a mono-exponential fit of MSE data delivers estimated values T_2^{MSE}. Here, we propose to calculate corrected T_2 values

$$T_2 = r \cdot T_2^{MSE} \tag{5.3}$$

by determining the ratio r with the help of EPG simulations. This can only be accomplished, if all parameters required for the EPG formalism (see Eq. 5.2) are known. While the temporal echo spacing ESP is known for a given acquisition, other parameters have to be determined from the data itself in order to compute r. In the following this is discussed in more detail for each of the parameters.

T_1:

For in vivo measurements, the T_1 relaxation time is usually high when compared to the T_2 values. Therefore, the T_1 decay of stimulated echoes plays a very small role in the signal evolution and its contributions can be neglected using a rough estimate for T_1 in all EPG calculations, which introduces only negligible errors [80]. In this work, a value of T_1 = 3000 ms is used for human tissue.

T_2:

The mono-exponential fit based on the MSE data itself yields a first estimate of T_2, which can then be used for the calculation of the correction factor. Figure 5.3 a) shows the dependency $r(T_2)$ for a MSE acquisition with ESP = 10 ms, ETL = 32, T_1 = 3000 ms and $\beta = [120°, 150°, 180°]$.

flip angle:

As explained above, the value for the flip angle may be inhomogeneous both in slice direction and in the image plane. For the calculation of the correction factor r, a mean flip angle across the slice is assumed. Under this condition, the flip angle can be approximated from the data itself by looking at the ratio R_E of the signal magnitude of first to second echo. Using EPG, it is calculated according to

$$\begin{aligned} R_E &= \frac{\sin(0.5 \cdot \beta)^4 \cdot \exp\left(-\frac{ESP}{T_2}\right) + 0.5\sin(\beta)^2 \cdot \exp\left(-\frac{ESP}{T_1}\right)}{\sin(0.5 \cdot \beta)^2} \\ &= \frac{1}{\sin(0.5 \cdot \beta)^2} \sin(0.5 \cdot \beta)^4 \cdot \exp\left(-\frac{ESP}{T_2}\right) + 0.5\sin(\beta)^2 \cdot \exp\left(-\frac{ESP}{T_1}\right) \\ &= \sin(0.5 \cdot \beta)^2 \cdot \exp\left(-\frac{ESP}{T_2}\right) + (1 + \cos(\beta)) \cdot \exp\left(-\frac{ESP}{T_1}\right) \\ &\approx \sin(0.5 \cdot \beta)^2 \cdot \exp\left(-\frac{ESP}{T_2}\right) + (1 + \cos(\beta)) \end{aligned} \tag{5.4}$$

For a given R_E in one image pixel, the flip angle can be numerically deduced from this equation. The exponential term containing T_1 usually approaches unity for T_1 >> ESP and its contribution can be neglected. Figure 5.3 b) depicts the dependency $r(\beta)$ with T_2 values of 50 ms, 200 ms and 500 ms.

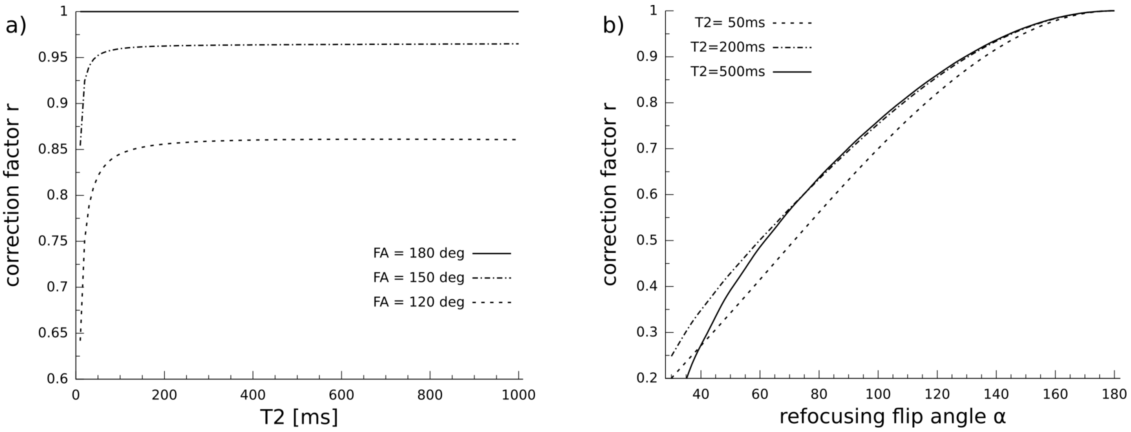

Figure 5.3: Illustration of r(T_2) for different refocusing flip angles β (a) and r(β) for different T_2 values (b) using a MSE acquisition with ESP = 10 ms, ETL = 32 and T_1 = 3000 ms.

Using the estimations for all required parameters, the MSE signal evolution can be computed with the EPG algorithm according to Eq. 5.2 and apparent T_2^{EPG} values are obtained via a mono-exponential fit. The correction factor then follows from the relationship

$$r = \frac{T_2}{T_2^{EPG}}. \tag{5.5}$$

The ratio r was calculated with the EPG formalism for clinically relevant sequence parameters ETL= 24 and 32, refocusing flip angles from 100° to 170° and an ESP ranging from 7 ms to 12 ms. As shown in Figure 5.4 for an ETL of 24 and 32, it can be described with excellent agreement by the heuristic formula

$$r(T_2) = a + \frac{b}{T_2} + c \cdot T_2, \tag{5.6}$$

since the curves are dominated by b/T_2 for small values of T_2 and by $c \cdot T_2$ for larger values. The parameters a, b and c are given in Tables A.1 and A.2 in the Appendix for the different values of ETL, flip angles and ESP. Using this formula removes the need for performing EPG calculations when applying this method.

The complete approach to obtain the corrected T_2 values from the MSE data is illustrated in Figure 5.5 and can be summarized in the following steps:

1. Perform a mono-exponential pixel-wise fit on the MSE image series to obtain a first estimate T_2 map.
2. Using Eq. 5.4, estimate the flip angle in each pixel from the ratio of the magnitude of the second to the first echo and the estimated T_2 value.
3. Compute the correction factor either by EPG calculations and using Eq. 5.2 or directy by using the heuristic formula given in Eq. 5.6.
4. Update the estimated T_2 values with the correction factor.

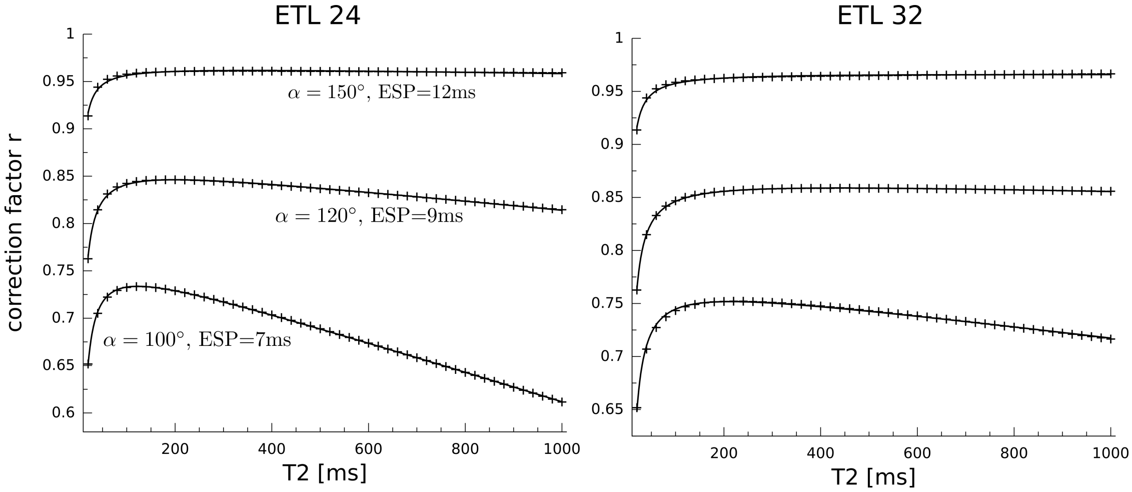

Figure 5.4: Deviation of T_2 values obtained with a MSE sequence from their real value for two different MSE sequences and three different sets of parameters. The solid line depicts the results from the EPG calculations, the points correspond to the values provided by the heuristic formula. All values are in excellent agreement.

5. Until convergence, iterate by going back to step 2, now using the updated T_2 value as input.

For all data shown in this work, a number of 2 iterations proofed to be sufficient for convergence.

5.2.3 Simulations

To investigate the influence of noise on the accuracy of the results, noise of three different levels was added to MSE signal evolutions calculated with the EPG algorithm for ETL = 16, T_2 values between 50 ms and 500 ms and for flip angles β = $120°, 150°, 180°$. Resulting maximum/mean SNR values along the echo train were 200/131, 100/66 and 50/33. The maximum value is hereby defined as the SNR of the highest peak along the signal evolution. For all signal decays curves, estimate and corrected T_2 values were obtained. This process was repeated 100fold for each noise level to obtain mean T_2 values and the corresponding standard deviations.

To obtain flip angle values from the data itself, the assumption of a constant flip angle across the slice is necessary. As this assumption is not met in real experiments, its impact on the accuracy of corrected T_2 values is evaluated. Simulations were performed for a typical excitation and refocusing slice profile shown in Fig. 5.7. Both slice profiles were obtained by direct measurement using a modified sequence. Simulations were carried out for three different combinations of refocusing over excitation slice thickness (1.0, 1.2 and 1.5), which corresponds to different levels of refocusing slice profile homogeneity across the excited slice. The overall signal evolution for the whole slice was computed for a MSE acquisition with ESP = 10 ms, ETL = 32 and T_1 = 3000 ms using the SEPG model introduced in [80]. Hereby, the slice was divided into 21 sections with different values of the peak refocusing flip angle β = $120°, 150°, 180°$ and for T_2 values between 50 ms and 1000 ms. The signal evolution for T_2 values between 50 ms and 1000 ms was calculated in each section with the EPG-algorithm and the total signal was obtained by a sum over all

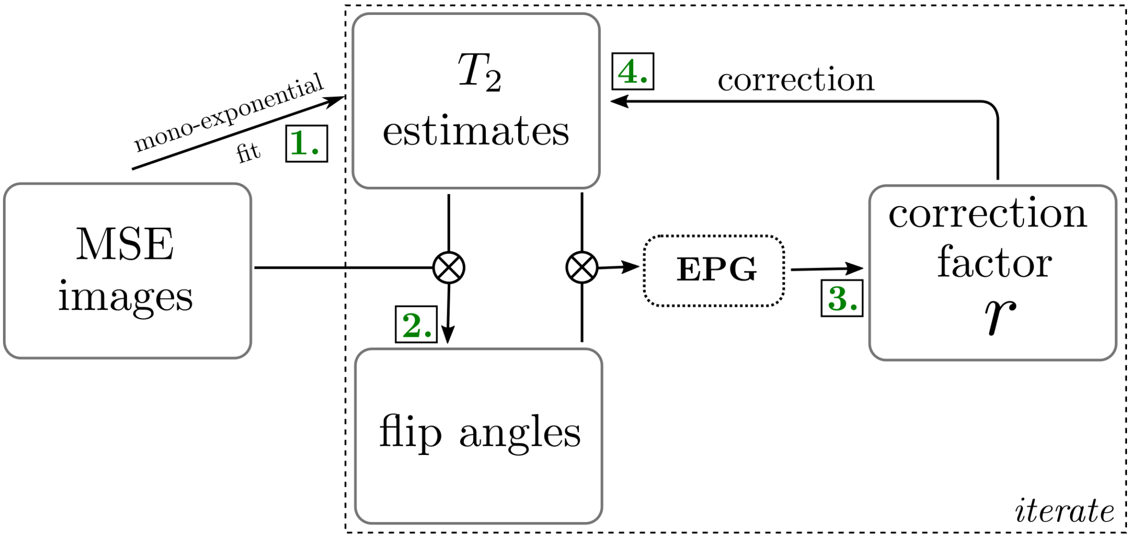

Figure 5.5: Calculation of accurate T_2 estimates from a multi spin-echo data set.

sections. Estimates of T_2 were obtained in each case using a mono-exponential fit. Subsequently, the mean flip angle as well as the correction ratio r were calculated with the proposed method.

Additional simulations were performed to investigate the influence of the specific T_1 value used in the proposed algorithm on the corrected T_2 estimates. MSE signal evolutions were generated with ESP = 10 ms, ETL = 32, α = 120° for T_2 = 60 ms, 100 ms, 200 ms and 300 ms and for T_1 values ranging from T_2 to $10 \cdot T_2$. Corrected T_2 values were obtained assuming a T_1 value of 3000 ms and compared to the reference.

5.2.4 Experiments

Experiments were performed on a standard clinical MRI scanner with a field strength of 3 Tesla using a phantom consisting of 9 bottles filled with liquids of different T_1 and T_2 values. Data were acquired with a head 12-channel receiver array and a Cartesian multi spin-echo sequence. Parameters were field of view 220 × 220 mm^2, matrix size 128 × 128, ESP = 9.3 ms, ETL = 32, receiver bandwidth = 200 Hz / Px and TR = 5 s. Three different data sets with refocusing flip angles of 120°, 150° and 180° were obtained. Additionally, spin-echo data sets of the phantom with identical sequence parameters were acquired at different echo times TE corresponding to the echoes of the MSE acquisition. Reference T_2 maps were extracted from the SE data using a mono-exponential fit. As the refocusing flip angle has no influence on the T_2 values obtained with a SE sequence, only one acquisition with a flip angle of 180° was performed.

In contrast to in-vivo experiments, the assumption $T_1 >> T_2$ is not valid for the phantom. For some substances, the value of T_1 is close to the corresponding T_2 value. Therefore, additional data were obtained using an inversion-recovery snapshot-flash sequence and T_1 values were computed following the procedure described in [81]. In each pixel, a fit of the signal evolution was performed with

Bottle	1	2	3	4	5	6	7	8	9
T_2 / ms	183	464	18	65	273	722	34	396	553
T_1 / ms	199	858	165	722	386	2036	344	732	1483

Table 5.1: Reference relaxation times of individual bottles of the phantom. T_2 was obtained with a spin-echo and T_1 with a IR Snapshot-FLASH acquisition.

$$M(t) = A - B \cdot \exp(-\frac{t}{T_1^*}). \tag{5.7}$$

T_1 values can be calculated according to

$$T_1 = T_1^* \cdot (B/A - 1). \tag{5.8}$$

The nine different T_1 and the reference T_2 values are listed in Table 5.1. The T_1 values were used in the proposed method to determine both the mean flip angle and the correction ratio r. Two iterations were used for the calculation of r in each pixel yielding spatially resolved T_2 and flip angle maps.

Neurological data of healthy volunteers were acquired with a clinical Cartesian MSE sequence. Written consent was obtained from the volunteers prior to the imaging session. Sequence parameters were field of view 220 × 220 mm^2, matrix size 160 x 130, ESP = 9.3 ms, TR = 5 s, ETL = 32, receiver bandwidth = 200 Hz / Px. A nominal refocusing flip angle of 120° was used. T_2 estimates were obtained via a pixel-wise mono-exponential fit and both the correction ratio r and the mean flip angle for each pixel were computed over two iterations.

5.3 Results

The impact of noise on the accuracy of estimate and corrected T_2 values is shown in Figure 5.6. Three different noise levels were added to the MSE signal evolution computed for ETL = 16 and for different T_2 and flip angle values. Mean estimate and corrected T_2 values as well as standard deviations were calculated by repeating the experiment 100-fold. In all cases, the standard deviation of corrected values is below or similar to the standard deviation of estimate T_2 values.

Another parameter to consider is the form and relative thickness of refocusing and excitation slice profiles. Figure 5.7 illustrates the impact of the refocusing and excitation slice profile on the accuracy of the estimated and corrected T_2 values. A MSE signal evolution was generated for two measured slice profiles with slice thickness ratios of 1.0, 1.2 and 1.5 and the three peak refocusing angles 120°, 150° and 180°. T_2 values were obtained with the proposed method. Mean relative deviations across all T_2 values are given in Table 5.2. A more inhomogeneous refocusing slice profile introduces larger errors in both the T_2 estimations and the corrected values, which is also true for a nominal flip angle of 180°.

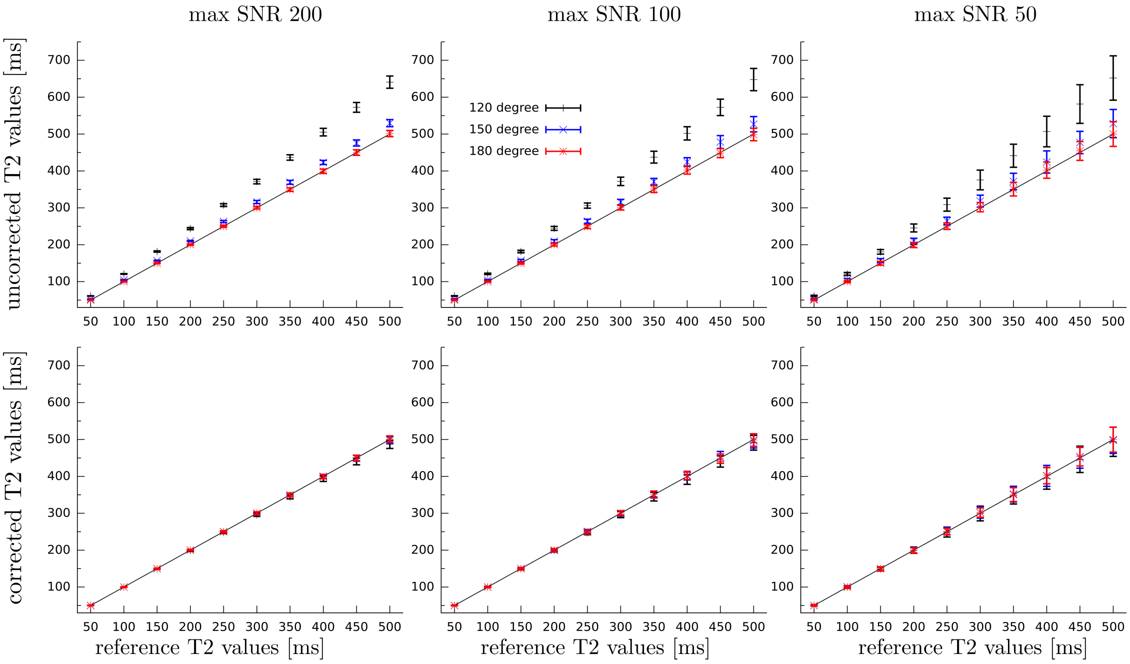

Figure 5.6: Impact of Gaussian noise on the accuracy of the T_2 estimates obtained with a mono-exponential fit (top row) and after correction (bottom row). Shown are the T_2 values obtained from simulated MSE signal evolutions together with the corresponding standard deviations for different noise levels and refocusing flip angles.

Thickness ratio	1.0		1.2		1.5	
Flipangle	Estimate	Corrected	Estimate	Corrected	Estimate	Corrected
120°	34.1%	7.4%	27.6%	3.6%	22.3%	1.2%
150°	16.7%	5.9%	11.6%	2.9%	7.5%	0.8%
180°	9.3%	4.8%	5.0%	1.9%	1.9%	0.5%

Table 5.2: Deviations of estimate and corrected T_2 values for different combinations of excitation and refocusing slice thickness.

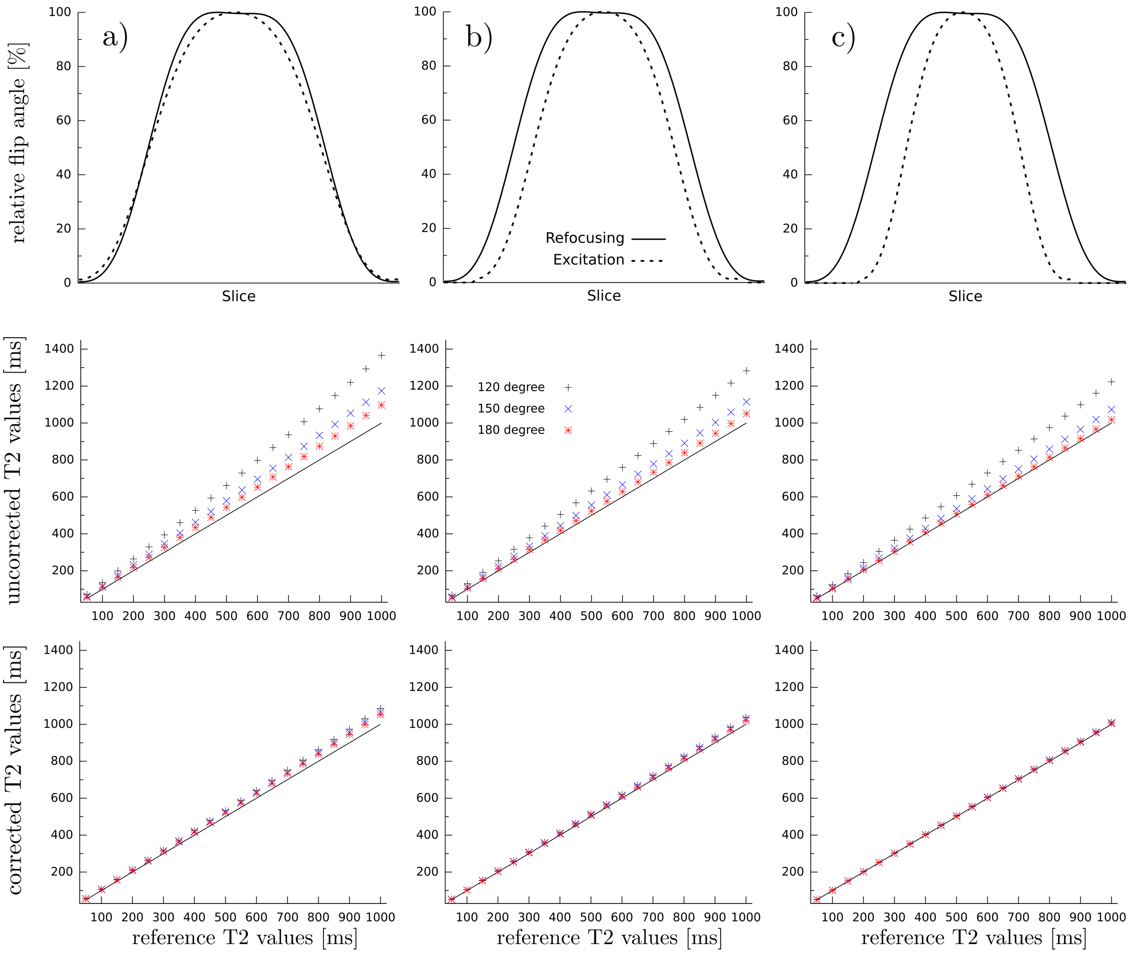

Figure 5.7: Impact of the slice profile on the T_2 results. Simulations were performed for one set of refocusing and excitation slice profiles typical for a SE sequence and three different combinations of relative slice thickness (top row). In each case, the signal evolution of a MSE acquisition was computed for three different nominal flip angles and T_2 estimates were obtained (second row). The corrected T_2 values are shown below.

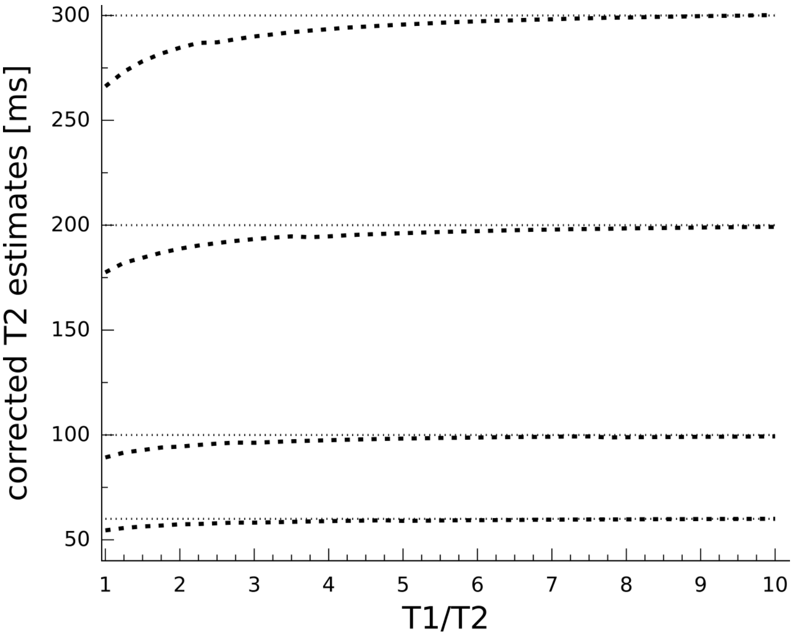

Figure 5.8: Influence of T_1 on the accuracy of the results. Shown are corrected T_2 values (dashed horizontal lines) from simulated MSE signal evolutions for four different T_2 and varying T_1 values. The proposed method was applied with a constant T_1 = 3000 ms.

Figure 5.8 demonstrates the influence of T_1 on the accuracy of corrected T_2 values, when a T_1 of 3 s is assumed in the algorithm. Corrected T_2 values were obtained from simulated MSE signal evolutions with T_2 values of 60 ms, 100 ms, 200 ms and 300 ms and for different T_1 values. Shown are the corrected T_2 values over the ratio T_1/T_2. For all four T_2 values used in the simulation, a similar behavior of the curve can be observed. While there are significant errors for small ratios ≤ 2, the deviation from the reference drops below 1% for ratios ≥ 6 in all cases.

Figure 5.9 shows T_2 maps of the phantom experiment using a reference spin-echo experiment and three separate MSE acquisitions with refocusing pulses of nominal flip angles 120°, 150° and 180°. The reference T_2 values obtained from the spin-echo acquisition are listed in Table 5.1 and range from 18.2 ms to 722.3 ms. While uncorrected T_2 maps from the MSE acquisitions show significant deviations from the reference, deviations are small for corrected values. Hereby, values obtained from the acquisition with a 120° flip angle are the most accurate. The mean flip angle maps corresponding to the three acquisitions are shown in Figure 5.10.

Figure 5.11 shows T_2 maps of the in-vivo brain data obtained with a MSE sequence using a refocusing flip angle of 120°. A significant difference is visible between the uncorrected and the corrected values. The corresponding mean flip angle map is shown on the right side.

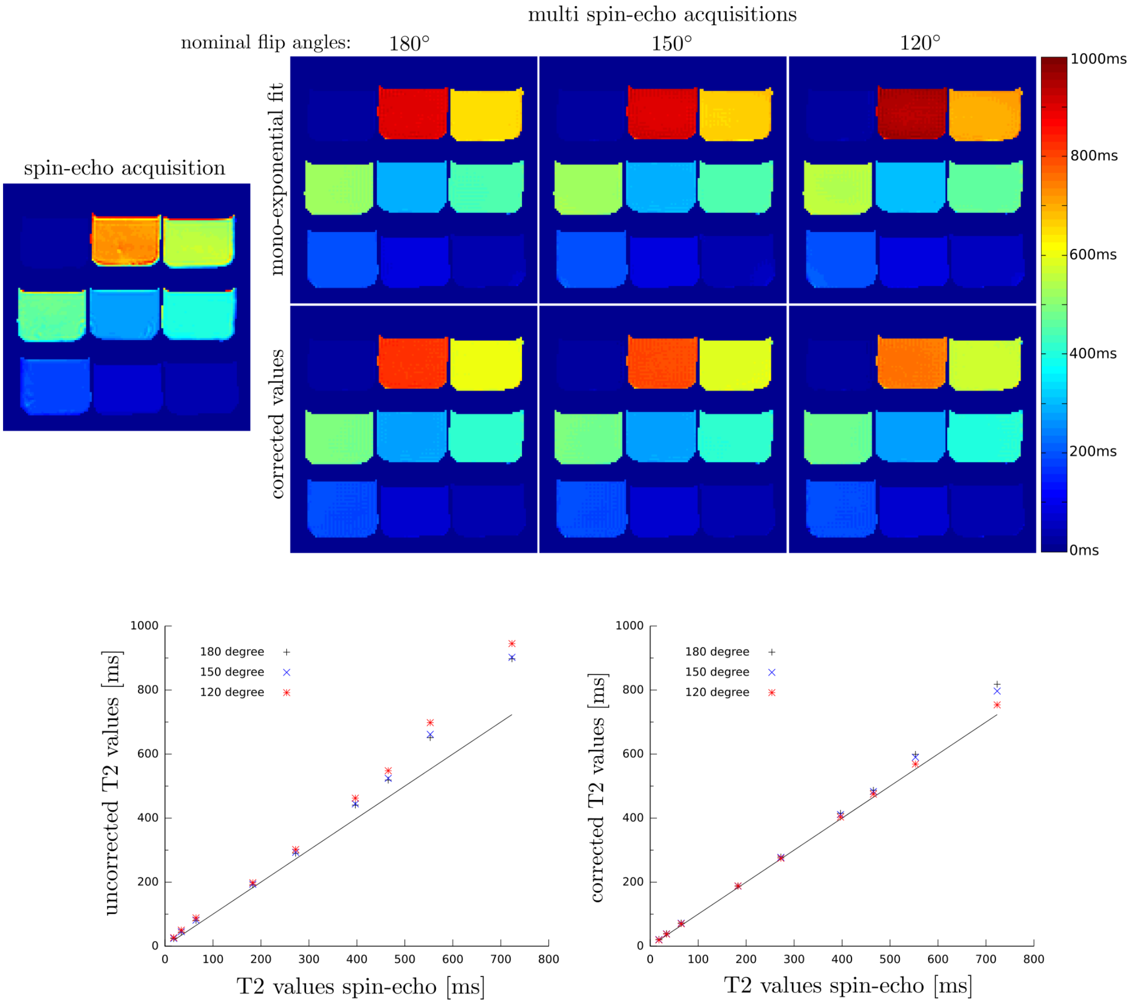

Figure 5.9: Phantom experiment. Spatially resolved T_2 maps are shown on top from a reference SE acquisition (left) and three separate MSE acquisitions (right) with varying flip angles of the refocusing pulses before and after correction. T_2 values were extracted in a ROI for each bottle and are displayed below.

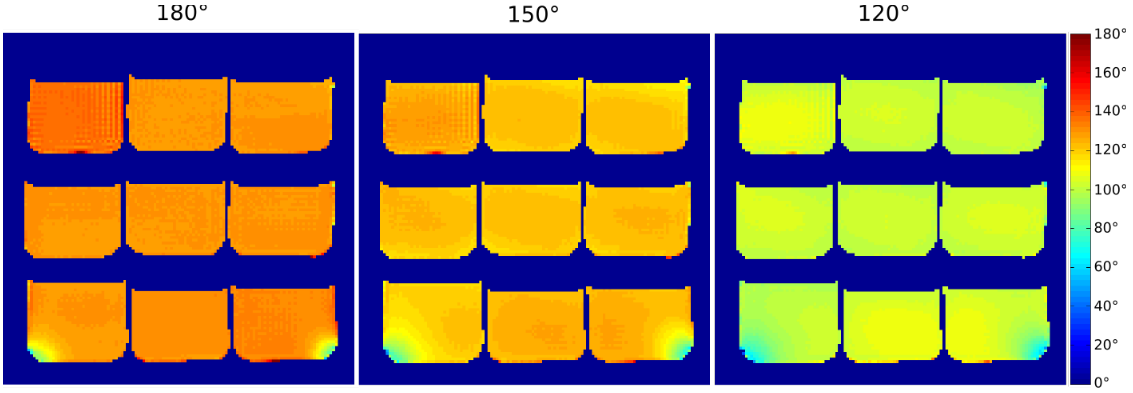

Figure 5.10: Spatially resolved maps of the mean flip angle from the phantom experiment.

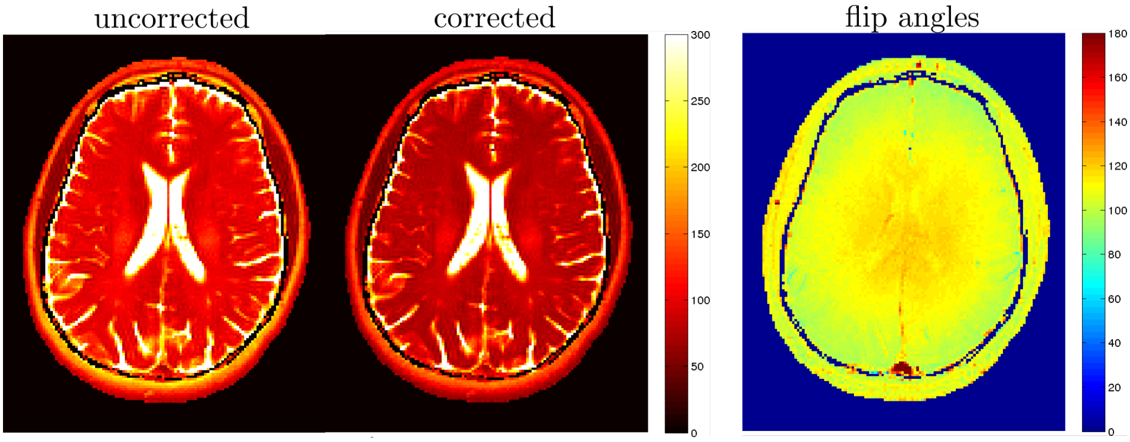

Figure 5.11: In-vivo brain T_2 maps before (left) and after (middle) correction and the corresponding flip angle map for a MSE acquisition with a nominal flip angle of 120°.

5.4 Discussion and Conclusion

In this chapter, a new method was introduced for the correction of T_2 estimates, that are obtained from a pixel-wise mono-exponential fit of MSE data. Due to refocusing pulses with flip angle values lower than 180°, stimulated echoes prolong the overall signal decay and lead to deviations of the T_2 estimates from the accurate values. The proposed method significantly reduces the errors introduced by stimulated echoes. The deviation of estimated from accurate T_2 values is a function of the flip angle of the refocusing pulses, the sequence parameters ETL and ESP as well as the time constants T_1 and T_2. Typical T_1 values in in-vivo experiments are significantly higher than T_2. As was shown in simulations, for $T_1 >> T_2$ an approximate value of $T_1 = 3\,\mathrm{s}$ can be assumed without noticeable impact on the accuracy of the method. However, the deviations show a strong dependence of the specific values of T_2. Especially for small T_2 values (specifically $T_2 < 100$ ms), the stimulated echo contributions to the overall signal intensity play a big role and the corresponding signal decay is prolonged significantly.

To allow correction of T_2 values obtained from a given MSE data set, the flip angle of the refocusing pulses has to be determined. In this work, a mean value for the flip angle is extracted from the data themselves by assessing the ratio of the intensities of the second and the first echo. This yields spatially resolved flip angle maps, so that potential B_1 inhomogeneities can be accounted for. One assumption of this approach is to disregard the flip angle variation across the slice. Simulations were performed to investigate the impact of this assumption on the accuracy of the results. Deviations of the corrected T_2 values from the real values increase with the extent of the refocusing flip-angle variation across the excited slice. For accurate results, a homogeneous refocusing slice profile across the excited slice is therefore desirable. As shown, this can for example be achieved by using a higher slice thickness for the refocusing than for the excitation pulse. Uncorrected T_2 estimates exhibit deviations ranging from 1.9% to 34.1% depending on the peak flip angle and the particular form of excitation and refocusing slice profiles. In contrast, deviations for corrected values (0.5% to 7.4%) are significantly reduced. In general, accuracy increases when using higher refocusing flip angle values. However, this effect is smaller than the impact of providing a homogeneous refocusing slice profile. Even only a moderate widening of the refocusing slice thickness leads to significantly improved results. This method therefore might also be valuable for high field strengths, where the SAR for 180° pulses is prohibitively high and lower flip angles have to be used.

The accuracy of the proposed method depends on the SNR of the acquired signal. However, as was shown in simulations, no loss in accuracy can be observed when compared to T_2 estimates obtained from a simple mono-exponential fit. Since flip angle values are computed from the two echoes with the highest SNR, results are very robust even in the presence of noise.

Results provided by the simulations could be confirmed in phantom experiments. Estimated and corrected T_2 maps were obtained from conventional MSE acquisitions using refocusing pulses with different flip angles. In all cases, T_2 values after correction only show small deviations from the reference. However, thanks to the better slice excitation profile at lower flip angle values, results obtained from the experiment with the lowest (120°) refocusing pulse turned out to be the most accurate. This is a welcome property of this method. It promises to allow accurate multi-slice T_2 quantification at high field strengths, which today is difficult due to SAR restrictions of sequences with a large number of high flip angle RF pulses. Since spatially resolved flip angle maps are used in this method, it delivers accurate results even in the presence of severe B_1 inhomogeneities, that pose a problem especially at high fields.

The proposed method requires nothing but the acquired data itself for calibration. The corrected T_2 values and the B_1 maps are computed in an iterative process. A fast convergence could be observed and only two iterations had to be applied for all examples presented in this chapter. This method might be especially valuable for experiments at high field strengths, where the SAR of sequences with a large number of 180° pulses is prohibitively high and lower flip angles have to be used. Using the highly accurate heuristic formula for the correction factors r developed in this work, no explicit EPG calculations are needed. This makes this method very easy to implement and in addition allows a real-time reconstruction on standard clinical scanners at runtime due to the low computational cost.

CHAPTER 6

Iterative GROG

Non-Cartesian trajectories in MRI have several advantages over standard Cartesian k-space coverage, including faster acquisition. Another method to reduce measurement time is parallel imaging. Many parallel imaging methods require a fully sampled center portion of k-space for either calibration or the calculation of coil maps. In this work, we use Calibrationless Parallel Imaging by Structured Low-Rank Matrix Completion, which exploits the low-rank property of GRAPPA source matrices, in combination with GROG to generate a fully sampled low-resolution center portion of k-space from undersampled non-Cartesian data.

6.1 Introduction

The acceleration of data acquisition in MRI is important for many reasons, and consequently many methods have been proposed to obtain a scan time reduction. One such method is to acquire fewer lines in k-space and to use parallel imaging (pMRI) to reconstruct a fully sampled image. Parallel imaging is well-established for Cartesian k-space sampling and available on many modern clinical scanners. However, for two-dimensional imaging, Cartesian sampling does not make full use of the potential of pMRI, as data acquisition is accelerated in the phase encoding direction and thus only a part of the spatial variation of the sensitivity profiles can be used. The combination of pMRI with non-Cartesian trajectories is a natural way to increase the possible acceleration factor, as undersampling these trajectories opens gaps in k-space in all directions and the potential of pMRI can be more efficiently exploited. Additionally, many non-Cartesian k-space sampling schemes are known to have intrinsic advantages, such as the oversampling of the k-space center, intrinsic reduction of acquisition times and reduced motion artifacts.

Many approaches have been proposed to combine the advantages of parallel imaging and non-Cartesian sampling. For SENSE-like reconstructions [6] which work in the image domain, a major obstacle is the complicated aliasing pattern of most non-Cartesian trajectories with contributions from almost every point in k-space, which leads to an inversion problem of large matrices. These can be solved by using iterative algorithms [42], which depend on the availability of accurate coil sensitivity maps. Unlike SENSE, reconstructions based on GRAPPA (General autocalibrating partially parallel acquisitions, [5]) do not require explicit coil sensitivity maps, but instead use a fully sampled portion of k-space for calibration. Several approaches for combining GRAPPA-based parallel imaging methods and non-Cartesian trajectories have been made [82–85]. While some of the existing methods can be used only for special trajectories such as radial or spiral, other methods use a multitude of GRAPPA kernels to adapt to arbitrary trajectories [86]. For some non-Cartesian trajectories, the necessary additional data for parallel imaging (sensitivity maps or calibration data) can be generated by gridding the center of k-space, if it is sampled sufficiently dense. This is the case for radial and some spiral trajectories applying moderate acceleration factors. Otherwise, the data has to be acquired in an additional scan.

In this chapter, the potential of Calibrationless Parallel Imaging by Structured Low-Rank Matrix Completion (CPI, [87, 88]) is explored to generate calibration data from arbitrary undersampled non-Cartesian data. CPI is an iterative k-space based parallel imaging method and was introduced for reconstructions of randomly undersampled Cartesian data. This method exploits the low-rank property of GRAPPA source matrices to calculate missing data points. The reconstruction of undersampled non-Cartesian data with CPI directly is not possible, as CPI requires gridded Cartesian data points. Therefore, the non-Cartesian data points must first be moved onto a Cartesian grid before the application of CPI. For undersampled non-Cartesian data, this gridding can be achieved using GROG (GRAPPA Operator Gridding, [89]). As a parallel imaging method similar to GRAPPA, GROG also requires a fully sampled central portion of k-space for calibration.

Thus, in this work an iterative algorithm (iterative GROG) has been developed using CPI in combination with GROG, which allows the calculation of the GROG weights based solely on the non-Cartesian data itself. This algorithm also works for many trajectories exhibiting undersampling in k-space center, where existing methods cannot be applied. The performance of this iterative process to generate a fully sampled center portion of k-space from undersampled data is shown for radial, rosette and spiral trajectories. The quality of the reconstructed data is assessed by using the corresponding GROG weights to grid the respective fully sampled datasets.

6.2 Methods

6.2.1 Cartesian CPI

Calibrationless Parallel Imaging by Structured Low-Rank Matrix Approximation uses part of the GRAPPA calibration process to reconstruct missing data points. In order to calculate GRAPPA

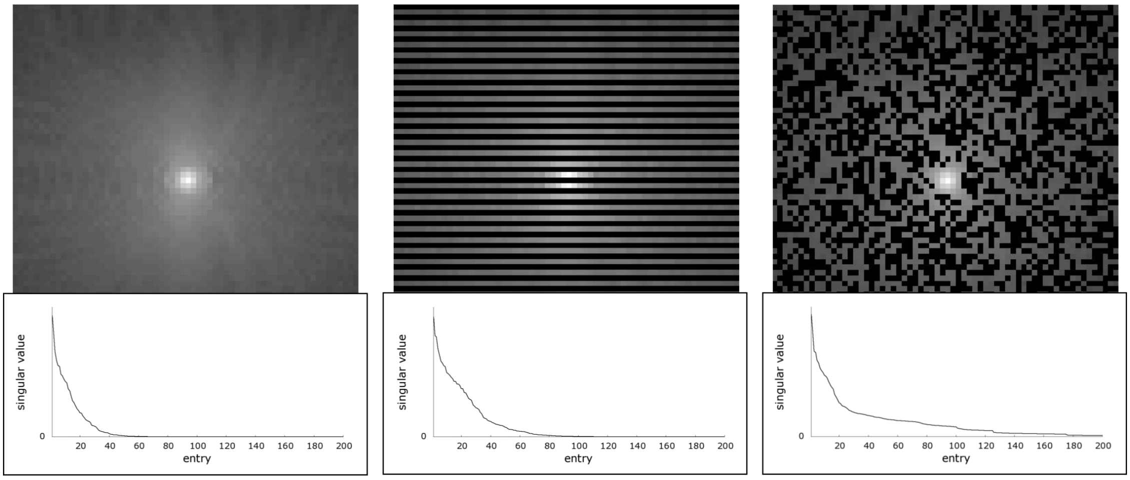

Figure 6.1: Singular values of the GRAPPA source matrix for a fully sampled (left) and R=2 regularly (middle) and randomly (right) undersampled k-spaces.

weights, the first step is to collect kernel repetitions in the autocalibration data and assemble these points into a source matrix. k-Space points close to each other are linearly dependent across coils, which is exploited by GRAPPA for the reconstruction of missing points. As a consequence, GRAPPA source matrices usually exhibit a low rank. This property changes if the source matrix is not assembled from a fully-sampled but an undersampled portion of k-space. In this case, the pattern of the source matrix is defective and its rank changes depending on the structure of the undersampling pattern. Figure 6.1 shows three example k-space patterns and the singular values of the corresponding source matrices, assembled with a square 5×5 kernel. In the case of a fully sampled k-space (left), the singular values quickly approach zero (only approximately 40 singular values are important) and thus the GRAPPA source matrix has low rank. If the k-space is regularly undersampled by skipping every second line corresponding to an acceleration factor of 2, the source matrix still exhibits a low but slightly higher rank (middle), whereas for a randomly undersampled k-space the singular values do not reach zero and therefore the matrix has full rank (right).

These properties of the rank of the GRAPPA source matrices are exploited by CPI to reconstruct missing data points. The first step of a CPI reconstruction is to assemble all points of an undersampled part of k-space into a source matrix SRC of size $N \times M$, where N is equal to the number of points in the chosen kernel times the number of coils and M equals the number of occurrences of the kernel in the undersampled k-space. As no GRAPPA reconstruction will be performed, in contrast to the procedure described in section 3.1.2 no target points need to be identified and a square kernel is used. As next step, a singular value decomposition of the source matrix is employed:

$$SRC = U \cdot S \cdot V \tag{6.1}$$

where S is a quadratic real-valued matrix of size $L \times L$ with $L = \min(N, M)$ containing the singular values of SRC. A low-rank approximation of SRC is calculated by truncating the

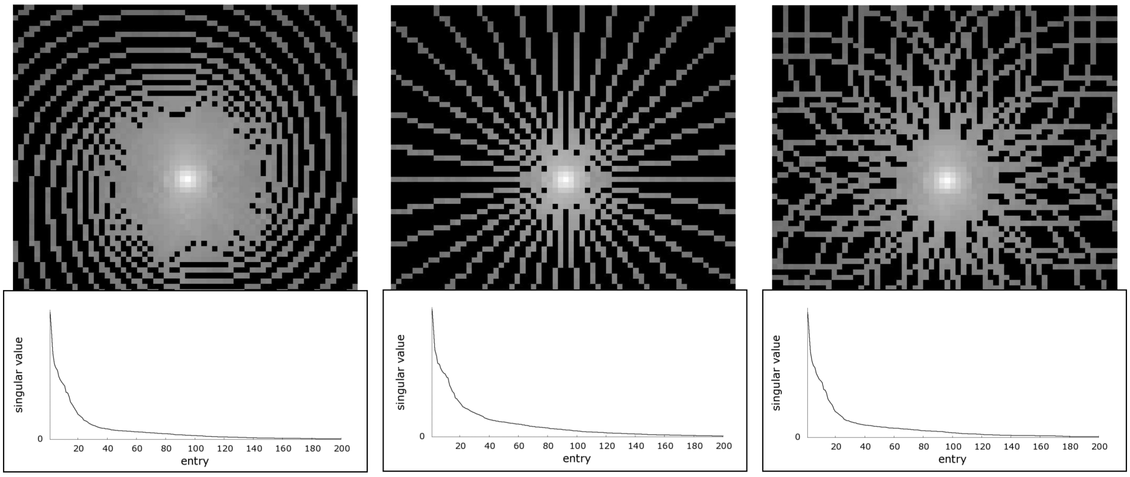

Figure 6.2: Undersampled k-spaces using three different trajectories after gridding with GROG and the singular values of the corresponding GRAPPA source matrices. The source matrices for the spiral (a), the radial (b) as well as the rosette (c) trajectories all exhibit full rank.

singular values and using the new singular values matrix S' to compute the updated source matrix

$$SRC' = U \cdot S' \cdot V. \tag{6.2}$$

The number of singular values employed has to be equal to or slightly below the value of the rank of the fully sampled GRAPPA source matrix. The data are then reassembled into k-space und averaged over the multiple occurrences of single k-space points. Finally, data consistency is invoked by replacing acquired data points into k-space. These steps are iterated until the singular values are constant. For optimal reconstruction performance of CPI, the sampling pattern should be chosen to guarantee a source matrix with full or at least high rank. While reconstruction is still possible for low-rank sampling patterns similar to Fig. 6.1 (middle), the number of required iterations is much higher. Figure 6.2 demonstrates, that non-Cartesian sampling schemes are in principle suited for reconstruction with CPI. Undersampled spiral (left), radial (middle) as well as rosette k-spaces lead to a source matrix exhibiting a full rank.

One important requirement of CPI is that the source matrices contain repeated points at the same locations in the kernel; this requirement is not met when working with undersampled non-Cartesian data. For randomly undersampled Cartesian data this is not a problem, but in order to use CPI for non-Cartesian data, the points must first be gridded before CPI can be employed. The gridding cannot be achieved using convolution gridding, as this method can only be applied to fully sampled datasets.

6.2.2 GROG

The concepts of GRAPPA introduced in section 3.1.2 can be used to grid non-Cartesian data by employing only one source and one target point in a method known as GROG (GRAPPA

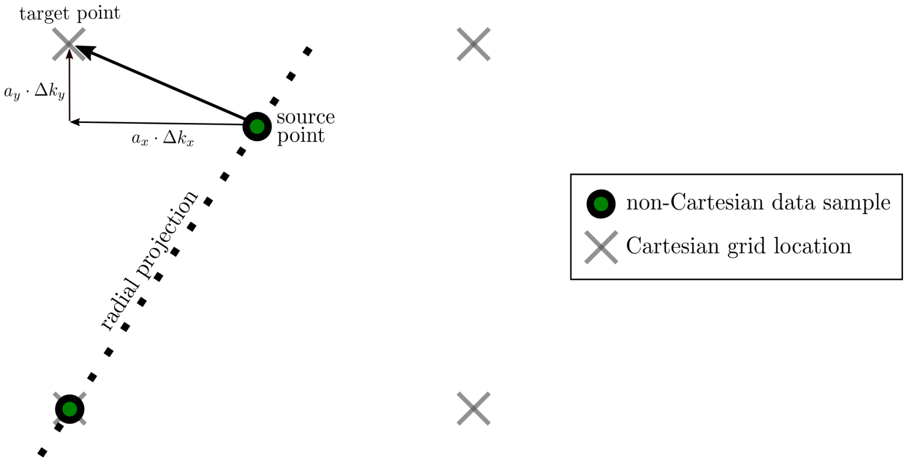

Figure 6.3: Gridding of non-Cartesian data with GROG. Using one source point, the corresponding value on the closest Cartesian grid location is obtained using GRAPPA.

Operator Gridding, [89]). This is shown in Figure 6.3. GROG uses one non-Cartesian data sample as source point to calculate the value at the closest location on the Cartesian grid (= target point). Same as GRAPPA weights, GROG weights are calibrated from a fully sampled center part of k-space. The resulting weights w_G describe the relationship between two neighboring points in k-space with a relative distance of Δk. However, to perform the desired gridding operation, non-Cartesian points have to be moved by only a certain part of Δk. As GROG weights are calculated from a single source- and a single target point, they have a quadratic form. In contrast to conventional GRAPPA weights, GROG weights can be scaled and combined to obtain shifts of arbitrary size in any direction. For example, to perform an arbitrary shift in two dimensions, GROG weights $w^x_{G,x}$ and w^y_G in two directions are generated from the ACS data for step sizes of Δk_x and Δk_y. An arbitrary shift is then given by

$$S(k_x + a_x \cdot \Delta k_x, k_y + a_y \cdot \Delta k_y) = w^{a_x}_{G,x} w^{a_y}_{G,y} S(k_x, k_y). \tag{6.3}$$

The scaled weights

$$w^a_G = \hat{U}(\underbrace{\hat{U}^{-1} w_G \hat{U}}_{w_{G,\text{diag}}})^a \hat{U}^{-1} \tag{6.4}$$

are calculated by diagonalization of the GROG weights and scaling their eigenvalues. For large shifts, GROG becomes unstable as it is based on a single source point. However, the required shift size for moving non-Cartesian points onto a Cartesian grid is always smaller than $0.5 \cdot \Delta k$. Because GROG relocates each non-Cartesian point to its nearest Cartesian grid location and does not use a large convolution kernel, it can be employed to grid undersampled data in addition to fully sampled data, which is not the case for standard convolution gridding. While the GROG weights needed to shift data can be determined from the non-Cartesian data points themselves for some trajectories, such as radial and some spiral trajectories [12], the calibration is more difficult for arbitrary trajectories. In these cases, GROG weights have to be calculated using a Cartesian auto-calibration signal, like GRAPPA, which can be obtained by either a prescan or by gridding the center of k-space if it has been fully sampled.

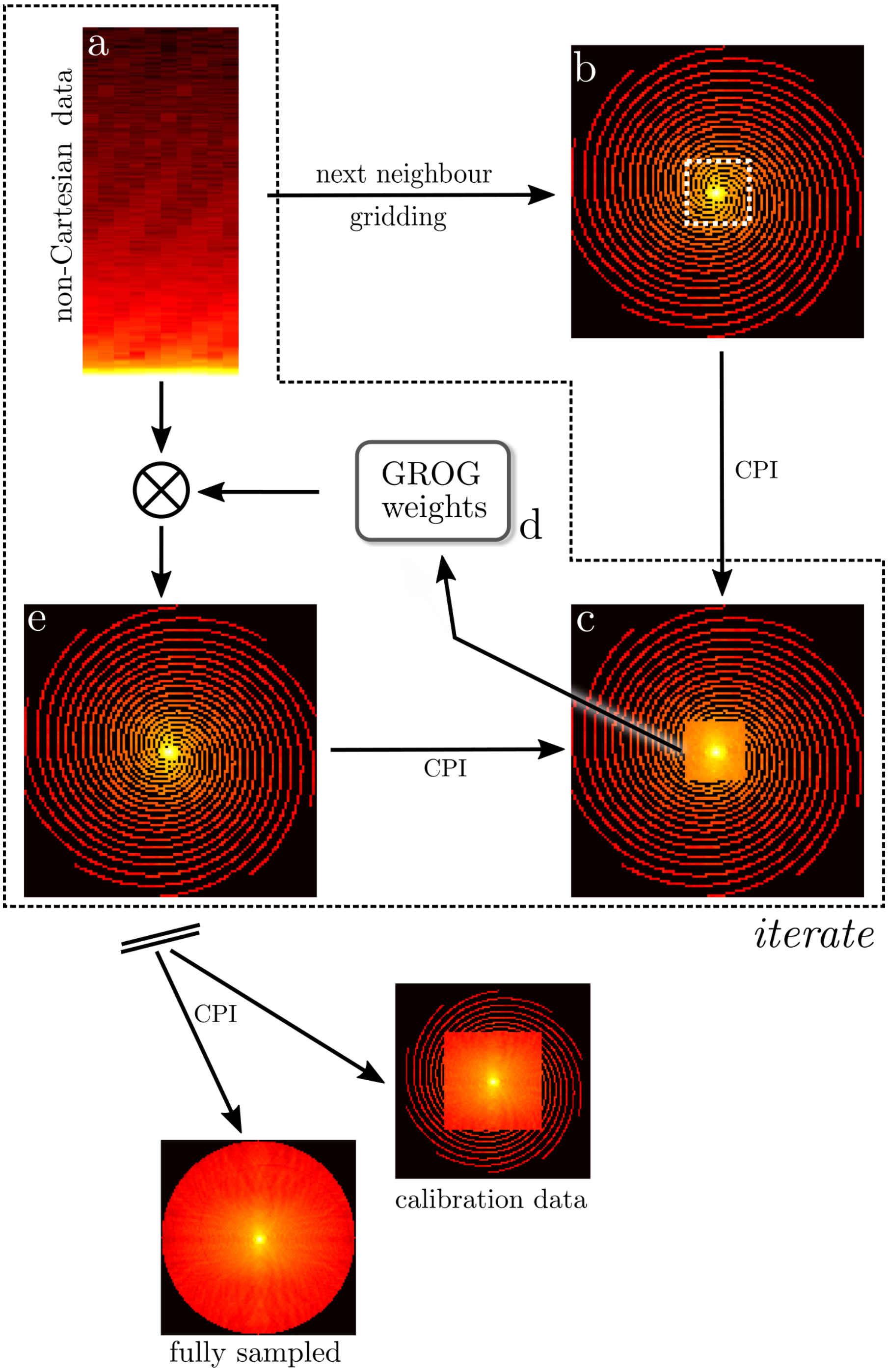

Figure 6.4: Flow diagram of the proposed iterative GROG gridding procedure.

6.2.3 Iterative GROG

In order to be able to employ CPI for reconstructing data acquired along non-Cartesian trajectories, they first have to be moved onto a Cartesian grid. However, in some cases neither is the center of k-space fully sampled, nor is it feasible to carry out an additional pre-scan. To address the challenge of determining GROG weights using undersampled non-Cartesian data, a new iterative gridding method based on a combination of GROG and CPI is presented. This method is shown schematically in Figure 6.4:

1. For initialization, the undersampled non-Cartesian data (a) are moved to the nearest Cartesian grids points without any change (next neighbour gridding) and averaged over all occurrences (b).
2. The central portion of the resulting k-space is selected and reconstructed using CPI (c). This fully reconstructed part of k-space can subsequently be used as calibration area for a first approximation of GROG weights (d).
3. Gridding of the undersampled non-Cartesian data is repeated, this time employing GROG and using the initial weights (e).
4. Go back to step 2 and iterate, until the GROG weights converge.

After convergence, the undersampled non-Cartesian data can be gridded with the final GROG weights. Now, a full k-space can be reconstructed using CPI. Alternatively, a calibration data set for a different reconstruction method (e.g. to obtain coil-maps for CG-SENSE or GRAPPA weights) of any desired size can be generated. It is important to note that the iterative GROG step is not necessary if the GROG weights can be determined from the data themselves, and in that case only CPI is employed.

6.2.4 Simulations and Experiments

To show the performance of CPI for non-Cartesian data, simulations were performed using spiral, radial and rosette trajectories. After generating a multi-coil signal by multiplying the standard Shepp-Logan phantom with simulated sensitivities of an eight-coil array, the non-Cartesian signals were calculated by resampling the corresponding k-spaces using NUFFT (Non-Uniform Fast Fourier Transform, [33]) and the image reconstruction toolbox [68]. Each trajectory was undersampled retrospectively using only every third projection/arm.

In order to determine whether the iterative GROG weights yield the same image quality as GROG weights determined using the fully-sampled center of k-space, reconstructions were performed using both methods. To calibrate the weights using iterative GROG, a center portion of k-space of size 32×32 was created from R = 4 undersampled non-Cartesian data using next-neighbor gridding. A kernel of size 5×5 was used to assemble the GRAPPA source matrix for CPI, and only the 35 largest singular values were retained and used to calculate the new data points. The first iteration of GROG weights was calculated using this 32×32 portion of k-space, and the process repeated. After five iterations of iterative GROG, the weights converged and the iteration was terminated. To assess the quality of the iterative GROG weights, they were used to grid the fully sampled non-Cartesian datasets. For comparison, additional sets of GROG weights were calculated using the 32×32 center portion of fully sampled Cartesian k-space and also used to grid the fully sampled non-Cartesian data.

A second non-Cartesian data set for all three trajectories was generated from a Cartesian brain image and undersampled by a factor of R = 3. Following the iterative GROG method, the weights were used to grid the undersampled non-Cartesian datasets as a first step in the CPI reconstruction. After gridding, CPI was employed for the reconstruction of the full k-space (128×128 points), again with a kernel size of 5×5 points. The singular values were truncated to the 35 largest values and 100 steps of CPI were used.

In vivo data of the head healthy volunteers were acquired on a standard clinical 1.5 T system (Magnetom Espree, Siemens Healthcare, Erlangen, Germany) and a Siemens head-coil with 32 channels. A spiral bSSPF sequence was employed with a repetition time of 4.96 ms, a field of view (FOV) of 250×250 mm^2 and a slice thickness of 5 mm. The variable density spiral trajectory employed consisted of 48 arms with 700 readout points each for a fully sampled dataset and covered a matrix size of 128×128. In order to reduce the size of the dataset and subsequent computation time, the number of receiver channels was compressed from 32 to 10 by applying principal component analysis [70, 71].

For reconstruction, data were retrospectively undersampled to factors of R = 2 with 24 arms, R = 4 with 12 arms and R = 6 with 8 arms, gridded with iterative GROG using the same parameters as above, and reconstructed using CPI. A number of 50·R iterations were chosen, increasing with the acceleration factor to account for the bigger gaps in k-space. Again, a kernel size of 5×5 was used and for all reconstructions with CPI only the 35 largest singular values of the GRAPPA source matrix were employed in every iteration step. For comparison, a CG-SENSE reconstruction with 12 iterations was performed on the R = 4 undersampled data. The required coil sensitivity profiles were obtained by gridding the fully sampled center region of k-space and using adaptive combine [67].

6.3 Results

The top row of Figure 6.5 shows the results of gridding fully sampled data acquired along the spiral (left image), radial (center) and rosette (right) trajectories with iterative GROG (left side of images), where the weights were computed from R = 4 undersampled data, and standard GROG (right side of images). The corresponding difference images with respect to the standard Cartesian Shepp-Logan phantom are shown in the second row. No differences in image quality using either method can be observed. In both cases, the relative error is of the order $1.1 \cdot 10^{-6}$ (spiral), $1.2 \cdot 10^{-6}$ (radial) and $1.8 \cdot 10^{-6}$ (rosette).

The results of reconstructing the R = 3 undersampled data using the complete CPI with iterative GROG reconstruction are shown in Figure 6.6. These images were generated using undersampled spiral (left), radial (center), and rosette (right) trajectories. The undersampled data gridded using iterative GROG are shown on the left side of each image, and the final CPI reconstruction shown

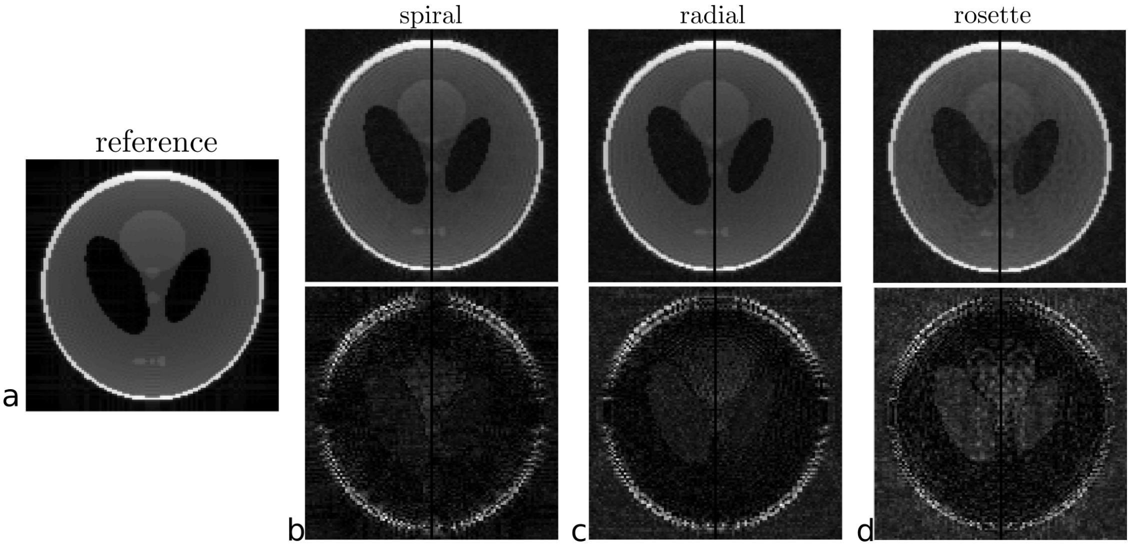

Figure 6.5: Gridding results using iterative GROG (left part of each image) and standard GROG (right part of each image) for spiral (b), radial (c) and rosette (d) sampling. In iterative GROG, weights were determined from R = 4 undersampled data sets; for standard GROG they were obtained from a fully sampled Cartesian center region of k-space. Below each gridded dataset, the difference image with respect to the standard Cartesian phantom (a) is shown.

on the right side. Note the reduction in blurring and streaking artifacts for each of the trajectories. For rosette sampling, residual artifacts are visible after reconstruction.

Figure 6.7 shows images obtained after gridding and reconstructing undersampled spiral data of the head using iterative GROG and CPI. For comparison, the fully sampled spiral image is shown on the top left. The undersampled and reconstructed image corresponding to acceleration factors of R = 2, R = 4 and R = 6 are shown in (b), (c) and (d) respectively. While the images reconstructed using data undersampled by a factor of 2 and 4 show few residual artifacts and exhibit mostly additional noise, at a R = 6 the reconstruction breaks down and artifacts are visible in the image. A CG-SENSE reconstruction of R = 4 accelerated data is displayed in (e) and shows comparable image quality.

6.4 Discussion and Conclusion

Calibrationless Parallel Imaging by Structured Low-Rank Matrix Completion has been shown to allow the reconstruction of images from undersampled non-Cartesian data acquired along radial, spiral and rosette trajectories. Existing parallel imaging methods for reconstructing arbitrary non-Cartesian data require either accurate coil sensitivity profiles or a fully sampled portion of k-space for calibration. This is not the case for CPI, which only requires that the GRAPPA source matrix assembled from the undersampled data has a higher rank than a fully sampled one. The GRAPPA source matrices corresponding to the mentioned trajectories all exhibit full rank and this

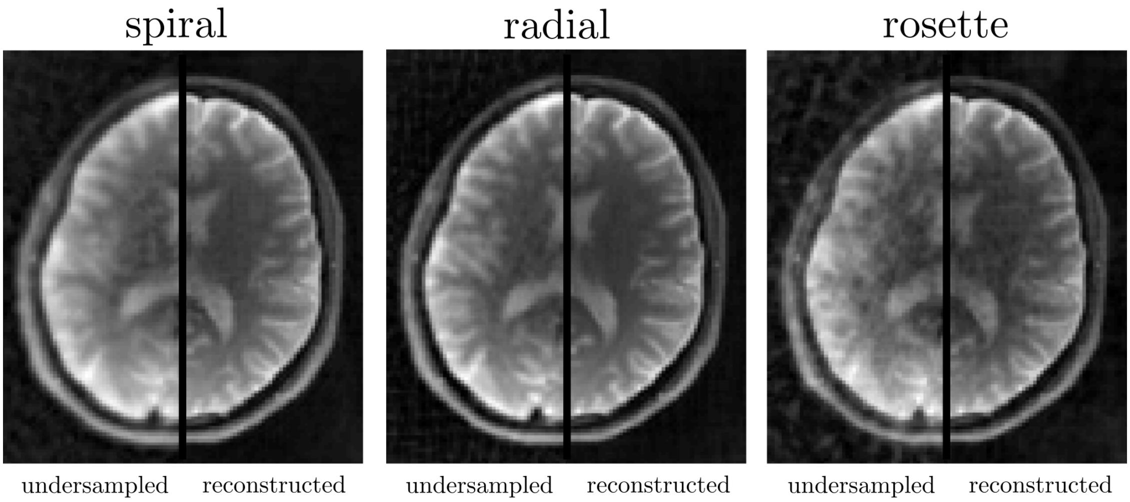

Figure 6.6: R = 3 undersampled (left part) and reconstructed (right part) images for spiral (left), radial (middle) and rosette (right) sampling. Reconstructions were performed using the complete iterative GROG with CPI method.

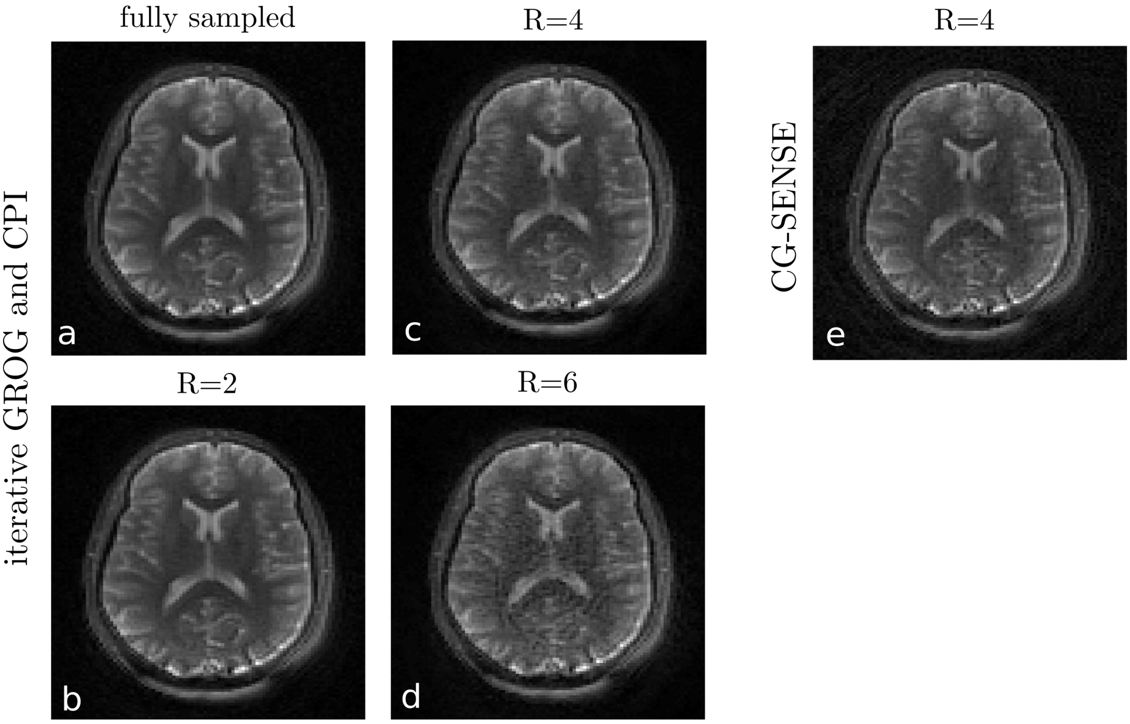

Figure 6.7: Reconstructions of in-vivo data acquired along a spiral trajectory. Figure (a) shows the fully sampled data after gridding with iterative GROG. The undersampled data after reconstruction with CPI are shown for acceleration factors of two (b), four (c) and six (d). A CG-SENSE reconstruction for an acceleration factor of 4 is shown in (e) for comparison.

is expected also to hold true for any non-Cartesian undersampled data with non-regular sampling patterns. Thus, CPI can potentially be used for any undersampled trajectory, without the need for adjustments to the algorithm.

In CPI, the rank of the source matrix changes only slightly with both the size of k-space and the number of channels and so the number of singular values employed does not have to be adjusted. If the number of singular values employed is either significantly too low (< 10) or too high, the reconstruction will fail completely, while for singular values in the range of 10 to 20, the reconstructed images exhibit blurring effects. The number of iterations needed in the CPI reconstruction depends mainly on the size of the gaps in k-space, which in turn varies with the acceleration factor and the sampling pattern employed. Therefore, non-Cartesian trajectories exhibiting gaps of constant size are best suited for reconstruction with CPI. It is important to note that CPI is a parallel imaging method, and the maximal gap-size must not exceed the reconstruction capability according to the available spatial variation in the coil sensitivity profiles.

As part of the CPI algorithm for non-Cartesian data, the undersampled data points are gridded using a novel iterative GROG method. This algorithm has been shown to generate accurate weights, which cannot be distinguished from those obtained using the standard approach. Thus, this method could be valuable for other applications, where undersampled non-Cartesian data have to be gridded and the GROG weights cannot easily be calculated. The reconstruction of non-Cartesian data with CPI employing GROG for gridding involves two separate parallel imaging steps. This leads to higher noise compared to other parallel-imaging methods, which reconstruct the non-Cartesian data directly before gridding, as errors in the gridding step influence the reconstruction with CPI and so propagate to the fully reconstructed image. Furthermore, the coil sensitivity maps have to show sufficient variation for both reconstruction steps. Thus, CPI should only be applied to trajectories, for which no optimized direct GRAPPA reconstructions exist.

CPI is an iterative method and so reconstruction time has to be considered. The most costly step in the reconstruction process in this respect is the singular value decomposition. The processing time strongly increases with the size of the GRAPPA source matrix $O(\min(n^2 d, nd^2))$, where n = number of columns and d = number of rows and amounts to several seconds for 8 channels and points. Implementing CPI in Matlab and using a standard desktop computer, the total reconstruction time for the simulated data is approximately twelve minutes. This issue could be addressed by using existing fast algorithms for low-rank matrix approximation (for example [90]), which reduce the computation time for each decomposition step.

CHAPTER 7

Multiple Oscillating Efficient Trajectories

7.1 Motivation

In the last few years, much research effort has been put forward to the development and application of Compressed Sensing (CS). CS is a specific type of constrained reconstruction relying on the sparsity of the investigated object. For successful reconstructions of MR data with Compressed Sensing, three main requirements (see section 3.3) have to be met. 1. The data to be reconstructed has to be sparse in a certain domain. 2. Every data sample has to carry information about the whole object and 3. the acquisition scheme has to provide incoherent aliasing in the presence of undersampling. A well-suited sparse base can be found for many applications. Examples (see Fig. 3.6) are reconstructions directly in image space [7, 91], in the wavelet domain [7], in the frequency domain in the case of dynamic objects with periodic movements [92] or combinations thereof. While the second requirement is automatically fulfilled for Fourier sampled MR data, truly incoherent aliasing artifacts in undersampled images is difficult to achieve in 2D sampling.

The point spread function (PSF) of a particular trajectory is well suited for investigating the level of (in)coherency. The PSF can be obtained by inverse transformation of matrix ksp_S made up of ones at all sampled and zeros at other k-space locations:

$$\text{PSF} = E^H(ksp_S). \tag{7.1}$$

The operator E^H represents a simple inverse Fourier Transform for Cartesian sampling or a combined gridding and Fourier Transform operation for the non-Cartesian case, as described in section 2.4.2.

Figure 7.1 shows undersampled 2D sampling schemes and the corresponding PSFs. Ideal for Compressed Sensing is Cartesian variable density random sampling on both dimensions (a) due to highly incoherent aliasing artifacts present in the PSF. Unfortunately, this sampling scheme is not feasible as the path through k-space has to be continuous. Restricting the variable density random sampling to one dimension (b) as proposed in [7, 93] leads to a higher level of coherence with pronounced aliasing artifacts. For a higher flexibility in k-space, non-Cartesian sampling schemes with varying read-out directions can be taken into account. Radial sampling (c) is routinely used for CS [94, 95] as it exhibits milder aliasing artifacts that, however, still show a significant level of coherence especially for high acceleration factors. Spiral sampling (d) can be implemented with a variable density distribution, but still exhibits coherent structures in the PSF.

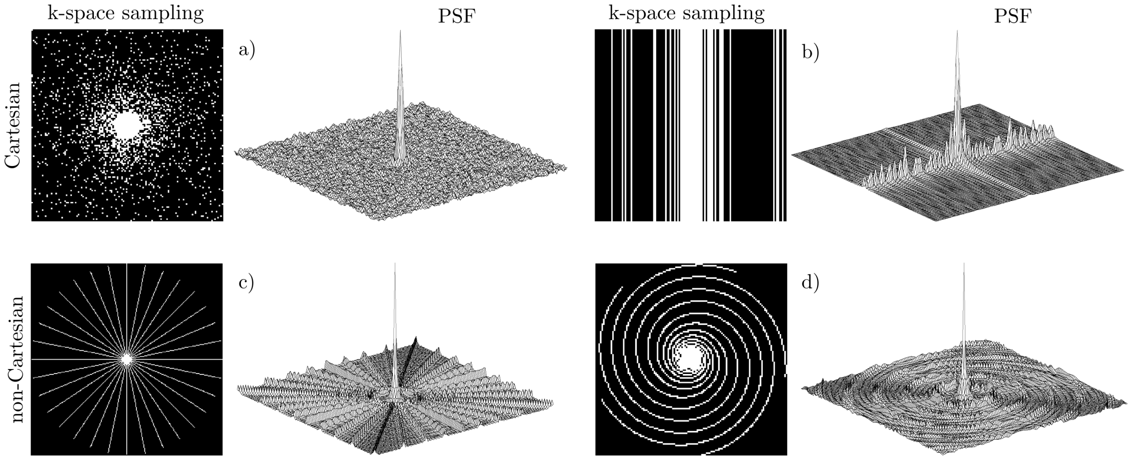

Figure 7.1: Two example Cartesian and non-Cartesian sampling schemes and the corresponding point spread functions.

As Compressed sensing is applied in the sparse basis and relies on an accurate first estimate of the image, coherent aliasing artifacts can prevent the reconstruction from converging to the desired solution. To achieve an incoherent sampling in 2D imaging, a new sampling scheme is proposed consisting of multiple oscillating efficient trajectories (MOET). MOET is based on radial sampling combined with oscillating gradients and provides high temporal efficiency and highly incoherent aliasing artifacts. To show the feasibility of this approach with temporarily varying gradient waveforms, MOET was implemented into a balanced SSPF sequence. Compressed sensing reconstructions of MOET data were performed in simulations exploiting sparsity in image domain. Additionally, both simulated and in vivo cardiac dynamic data with high sparsity in temporal frequency space were reconstructed with CS. In both cases, results were compared to reconstructions of radially sampled data. In-vivo cardiac images can be reconstructed with compressed sensing from data sampled along the MOET trajectory using only 8 projections per frame.

7.2 Methods

7.2.1 MOET

The proposed MOET sampling scheme is a combination of radial sampling stretched to fill the full rectangular k-space and oscillating gradients of varying amplitude orthogonal to the readout direction. To achieve coverage of the full rectangular grid, the readout gradient amplitude G_R has to be varied with the projection angle α according to

$$G_R(\alpha) = G_{RO} \cdot \mathrm{MIN}\left(\frac{1}{\cos(\alpha)}, \frac{1}{\sin(\alpha)}\right), \tag{7.2}$$

where G_{RO} is the amplitude of the standard readout gradient. Since the diagonal projections cover the greatest distance in k-space and therefore has to be highest, they are chosen to be sampled along a straight line without oscillations and define the maximum gradient strength used. For all other projections, a smaller readout gradient strength suffices and the difference in gradient strength can be used for the oscillating gradients orthogonal to the readout direction allowing for optimizing the PSF as well as time efficiency of the trajectory. The maximum amplitude of the oscillations is calculated to be:

$$G_M(\alpha) = \sqrt{G_{R,max}^2 - G_R(\alpha)^2}. \tag{7.3}$$

To achieve high efficiency, the oscillating gradients are chosen to have a standard trapezoidal form. This guarantees the highest total gradient moment and therefore highest velocity in k-space. The number of oscillations can be chosen freely given that slew rate restrictions are taken into account. The orientation of the oscillating gradients can also be flipped, allowing for more incoherent sampling patterns. A central part of each projection is sampled without oscillations to achieve a homogeneous coverage of the center region of k-space. Oversampling in the readout direction was increased from the standard value of two to four to capture the faster movements through k-space compared to radial sampling. The MOET sampling pattern changes slightly with field of view (FOV) and receiver bandwidth.

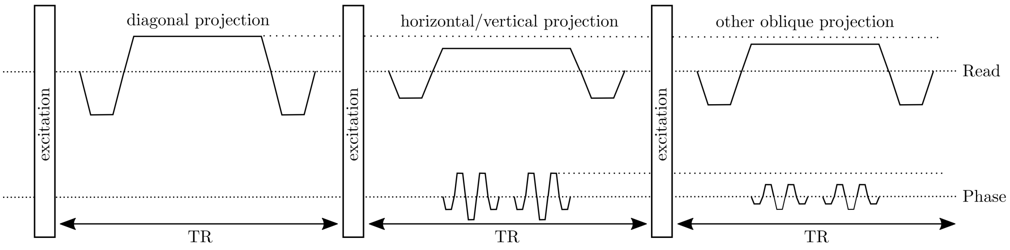

Figure 7.2: Diagram of the MOET bSSFP sequence. The gradient waveforms of the logical Read and Phase encoding axes are shown. Diagonal projections are sampled along a straight line. The gradient amplitude is hereby adjusted to fill the full rectangular k-space. Other projections require less readout gradient amplitude. The remaining available gradient strength is used for oscillating gradients. The slice selection axis is omitted.

The MOET trajectory was implemented into a balanced SSFP sequence. An example sequence diagram for a MOET trajectory with 4 oscillations is depicted in Figure 7.2 and shows the gradient waveforms on the logical read and phase axes. To allow for retrospective undersampling to different acceleration factors as well as to provide incoherent sampling in the image-time domain, a golden ratio ordering scheme was employed [32]. As discussed in section 2.4.1, the golden angle sampling scheme is accomplished by using large jumps in the rotation angle (namely 111.2461°). These jumps in turn correspond to large differences of the gradient amplitudes on the physical axes, which can disrupt the steady state due to eddy currents. Therefore, gradient pairing was applied as proposed in [96] by always acquiring two adjacent projections before calculating the next step according to the golden ratio. Figure 7.3 shows the impact of gradient pairing on fully sampled MOET images. The phantom image without gradient pairing (left) exhibits visible artifacts, that are not present in the image acquired with gradient pairing (right).

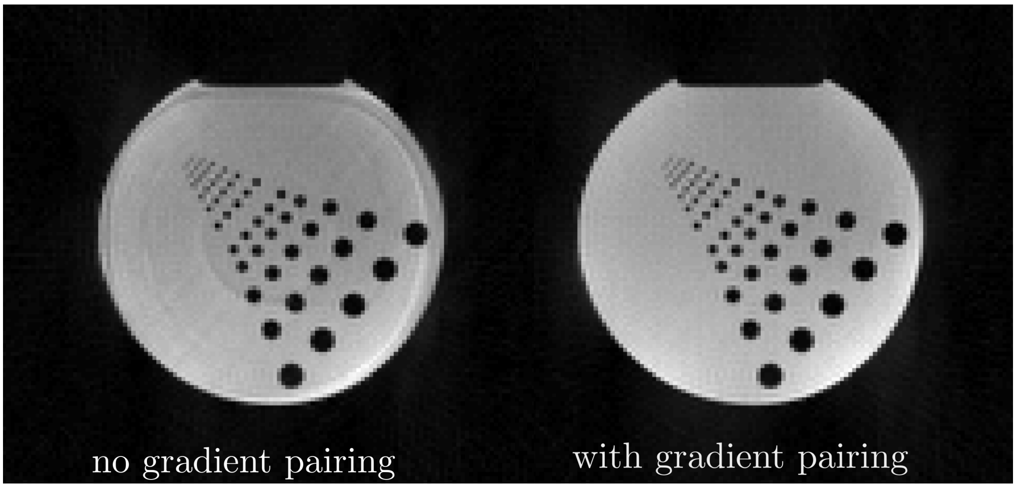

Figure 7.3: Example MOET images of a phantom without (left) and with (right) pairing the trajectory. Eddy current artifacts are present in the image acquired without gradient pairing.

k-Space Trajectory Measurement

MOET sampling changes with the chosen field of view and the receiver bandwidth. Additionally, deviations from the theoretical trajectory can occur due to both eddy currents (induced by the gradients with high slew rates necessary for fast dynamic imaging) and gradient delays. The latter lead to small changes in the trajectory that are also dependent on the slice orientation due to different gradient delays for the physical axes. Therefore a method for the accurate determination of the actual trajectory has to be applied. Duyn et. al. proposed a method for trajectory measurements that requires no extra hardware but only small changes in the sequence used for the actual experiment [97].

In this method, a thin slice (1-2 mm thickness) is excited orthogonal to the desired gradient direction as shown in Figure 7.4 (left). In the sequence, this is achieved by moving the slice selection gradient from the slice axis to the desired axis. Placing the slice at an off-center position

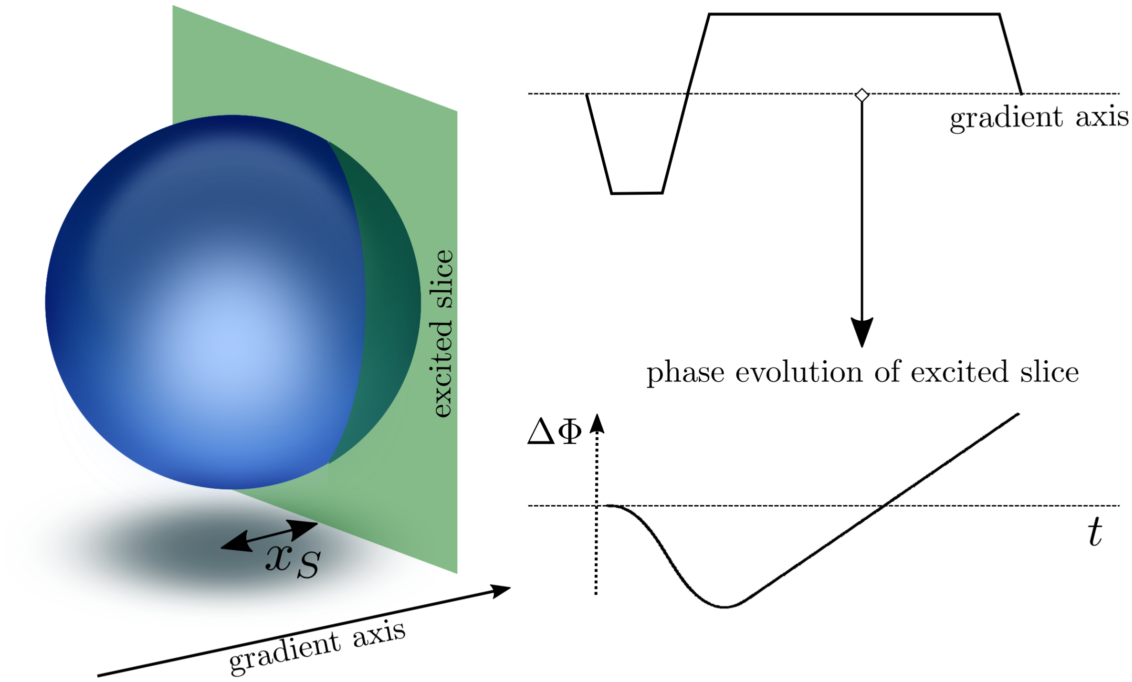

Figure 7.4: Trajectory measurement method. A thin slice is excited orthogonal to the axis of the gradient to be measured. The corresponding k-space trajectory can be deduced from the phase evolution of this slice.

x_S, the signal evolution $S_G(t)$ during application of the gradient $G(t)$ is given by

$$S_G(t) = c \cdot \exp\left(i\gamma \int_0^t dt' \; G(t') x_S + i\alpha(t) \right) = c \cdot e^{i(kx_S + \alpha(t))} \equiv c \cdot e^{i\Phi_G(t)}. \tag{7.4}$$

To remove the phase contributions $\alpha(t)$ that are independent of G, the same experiment is repeated without applying the gradient:

$$S_0(t) = c \cdot e^{i\alpha(t)} \equiv c \cdot e^{i\Phi_0(t)} \tag{7.5}$$

The offset x_S of the slice is known and so the trajectory can easily be deduced from the phase difference

$$\Delta\Phi(t) = \Phi_G(t) - \Phi_0(t) = x_S \cdot k(t) \tag{7.6}$$

of both acquisitions. A typical temporal evolution of $\Delta\Phi(t)$ for a conventional readout gradient is shown on the right hand side of Figure 7.4. If multiple gradient axes are active during data acquisition, this trajectory measurement has to be performed separately for each of those axes.

For MOET, both the frequency encoding gradient as well as the oscillating gradients have to be measured. Figure 7.5 shows the trajectory measurement of two identical oscillating gradients with inverted polarity. In the center part without oscillating gradients, the two waveforms are not symmetrical due to eddy current contributions.

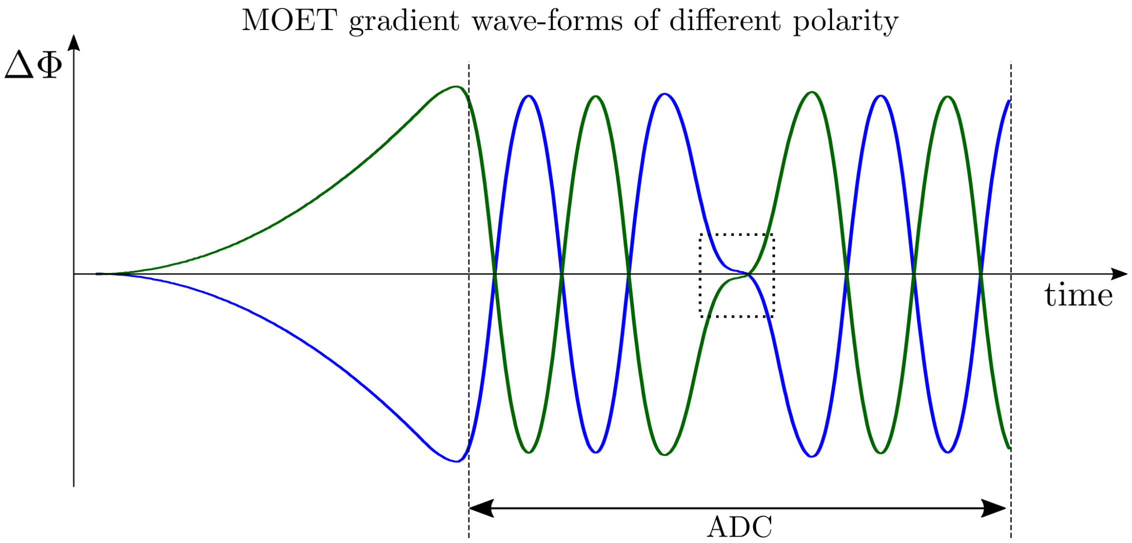

Figure 7.5: Two measured MOET waveforms of different polarity, that are otherwise identical. Due to eddy current contributions, the measured trajectories are not symmetrical (marked by the square).

Point Spread Functions

Three example Moet trajectories with 2, 4 and 6 oscillations per line using only 16 projections are shown in Figure 7.6 together with their point spread functions for a matrix size of 128×128. For comparison, the corresponding radial trajectory with its PSF is also displayed. While for both 2 and 4 oscillations the point spread function is highly incoherent, the PSF of MOET with 6 oscillations as well as of radial sampling exhibit streaking artifacts due to the smaller (or non-existent) amplitude of the oscillations. Therefore, all simulations and in-vivo acquisitions in this work were done using the MOET trajectory with 4 oscillations.

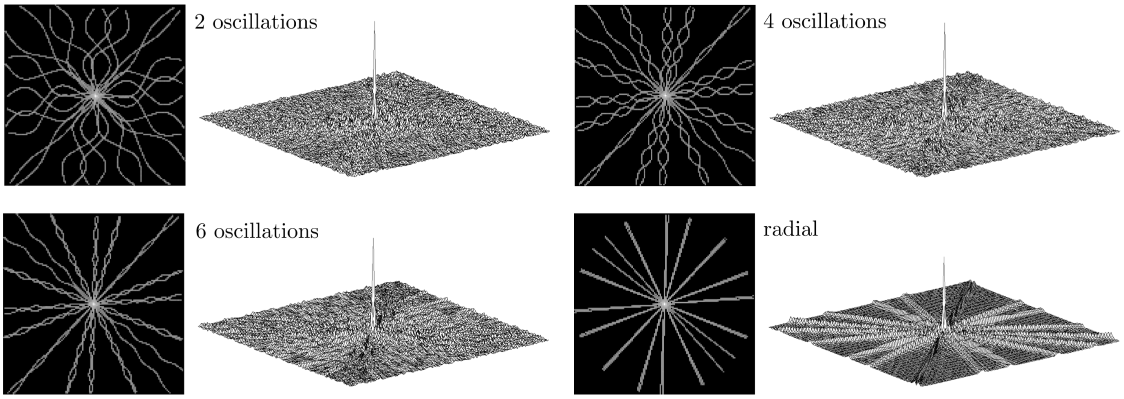

Figure 7.6: Trajectory of a typical frame with 16 projections for radial and MOET sampling with 2, 4, and 6 oscillations. The corresponding point spread functions are shown to the right. While the radial sampling exhibits leads to streaking in the PSF, this is not the case for the MOET sampling.

7.2.2 Compressed Sensing reconstruction

All reconstructions in this chapter were performed by minimizing the term

$$||E \cdot x - y||_2^2 + \lambda ||\Psi x||_1 \tag{7.7}$$

using a non-linear conjugate gradient algorithm [7] as discussed in section 3.3.3. Hereby, E is the encoding matrix incorporating the employed trajectory and the sensitivity information of the receiver array, y is the acquired data, x is the reconstructed image and Ψ the sparsifying transform. This particular algorithm was chosen because it is well established and can be applied to arbitrarily sampled data.

The necessary gridding and degridding operators were implemented using convolution gridding [33, 68]. Following the procedure described in [42], data from all coils were combined into one single image employing adaptive combine [67] before each iteration step was applied. The required density compensation functions were calculated according to the iterative approach proposed by Bydder et. al [38]. All simulations and reconstructions were implemented in MATLAB (The MathWorks).

7.2.3 Simulations

Due to its incoherent aliasing artifacts, MOET is expected to outperform radial sampling in compressed sensing reconstructions. In order to demonstrate this, simulations were performed using an image with high sparsity in image space with a matrix size of 128 × 128. After modification with a simulated receiver array with four elements, fully sampled non-Cartesian data for the MOET and standard radial trajectory were obtained using the toolbox provided by Fessler [68]. White Gaussian noise was added to the non-Cartesian data in order to generate realistic conditions, resulting in SNR values ranging from $10 - 100$ for the fully sampled images. Images were reconstructed from only 4, 16 und 24 projections (MOET) and 24 projections for the radial trajectory using Eq. 7.7 with $\Psi = \mathbb{1}$.

The influence of the trajectory on CS reconstructions of dynamic MR data was investigated using a periodically moving phantom with a matrix size of 128 × 128 and 20 temporal frames. This phantom exhibits no sparsity directly in image space but high sparsity in the frequency (xf) domain, since only a small region of the image exhibits motion. After modifying with the simulated receiver arry, non-Cartesian data was simulated along the MOET and a standard radial trajectory using the golden-ratio reordering with 16 projections per frame. This reordering leads to a high incoherence of aliasing artifacts in xf space. Compressed sensing reconstruction were performed in the frequency domain (so that $\Psi = \mathrm{FT}_t$) without added noise as well as with Gaussian noise for SNR values ranging from 27 – 100 for the fully sampled images (144 projections per frame).

7.2.4 In vivo cardiac experiments

Dynamic cardiac data from a healthy volunteer were acquired with both the radial and MOET trajectories on a conventional 1.5T whole-body clinical scanner (Avanto, Siemens Healthcare, Erlangen, Germany) using a 15 channel combined body and spine array. Prior to the imaging session, written informed consent was obtained. Data acquisition was performed during a breath hold in order to obtain high sparsity in xf space. A bSSPF sequence with golden-ratio reordering and gradient pairing was used for data acquisition along the radial and the MOET trajectory with 4 oscillations. Sequence parameters were: TR = 2 ms, flip angle = 60°, receiver bandwidth 890 Hz / Px, FOV = 300 mm^2, slice thickness 5 mm. A total number of 4096 projections were acquired leading to a measurement time of 13.1 s. Compressed sensing reconstructions in xf-space according to Eq. 7.7 ($\Psi = \text{FT}_t$) were applied to undersampled MOET and radial data using 8 and 16 projections per frame with temporal resolutions of 25.6 ms / frame and 51.2 ms / frame respectively. The receiver sensitivity profiles required for gridding operations were estimated with the adaptive reconstruction algorithm [67] using the temporal average of acquired data.

7.3 Results

Figure 7.7 shows CS reconstructions from MOET and radial data, which were simulated from a phantom with high sparsity in image space. Images were reconstructed from 4, 16 and 24 MOET and from 24 radial projections. The top row displays the corresponding undersampled images reconstructed with convolution gridding. In the undersampled MOET images, the structures can be resolved even for the image reconstructed from only 4 projections. Consequently, the corresponding CS reconstructions show few residual aliasing artifacts, especially for 16 and 24 projections. In contrast, for radial sampling the structures are not distinguishable either in the undersampled or in the reconstructed image. This is also reflected in the relative RMSE values of 18.4% (4 projections), 13.9% (16 projections) and 12.1% (24 projections) for the MOET images and 32.7% for the radial image.

Figure 7.8 displays the CS reconstructions of dynamic phantom data exhibiting sparsity in xf-space. In the top half, results for both MOET and radial sampling are displayed without noise, while on the bottom results are shown for added noise leading to SNR values between 27 and 100. For each reconstruction, the specified line in image space is plotted versus time to visualize the temporal accuracy of the reconstruction. Without added noise, using the radial trajectory leads to reconstruction artifacts clearly visible in image domain (relative RMSE 2.9%), while using data along the MOET trajectory provides very high image quality in the reconstructions (relative RMSE 1.6%). Similar observations can be made in the reconstructions with added noise. Again, more reconstruction artifacts are visible for the radial trajectory, especially at the locations indicated by the arrows. Here, the relative RMSE values are 4.5% for the radial images and 4.1% for the MOET images.

Figure 7.9 shows the compressed sensing reconstructions of in-vivo cardiac data. Data along a radial and the MOET trajectory were acquired during a breath hold to obtain high sparsity in xf space. Reconstructions were performed in frequency space ($\Psi = \text{FT}_t$) from undersampled

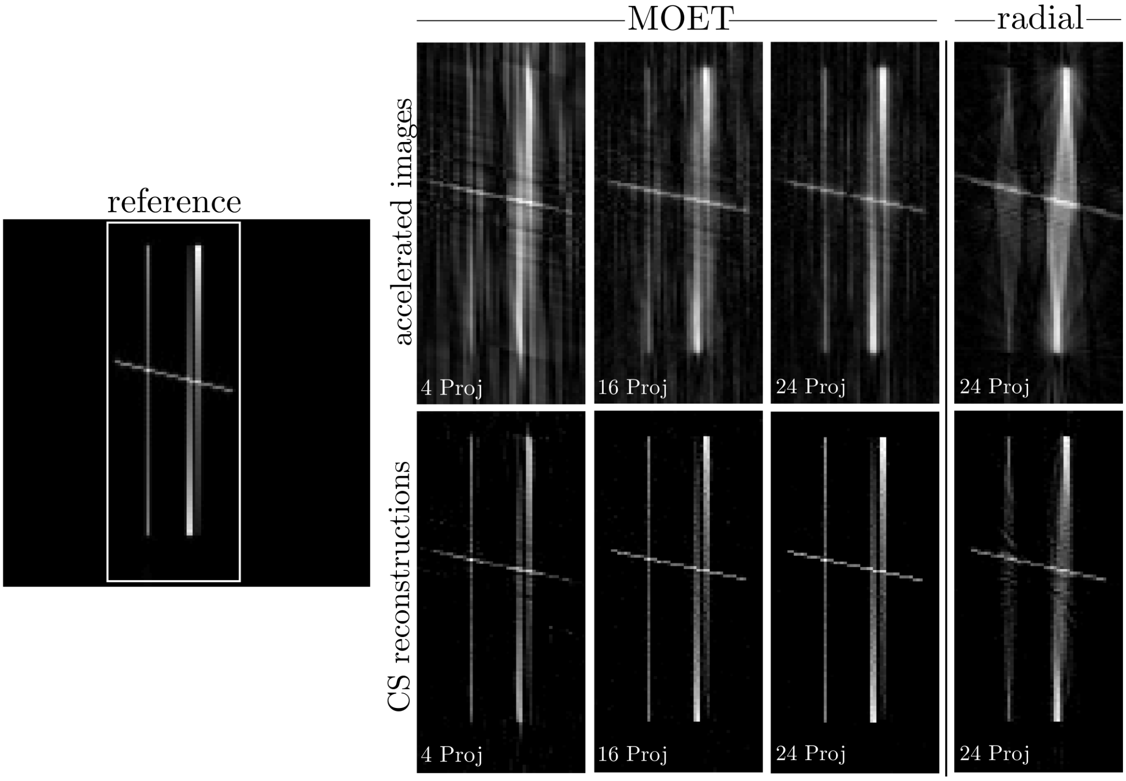

Figure 7.7: Undersampled images and compressed sensing reconstructions of simulated data for both radial and MOET sampling. The simple synthetic phantom image (left) exhibits high sparsity in image space and is ideal for reconstruction with CS. In both undersampled and reconstructed MOET images, the structures can be distinguished clearly. This is not the case for radial sampling due to streaking artifacts.

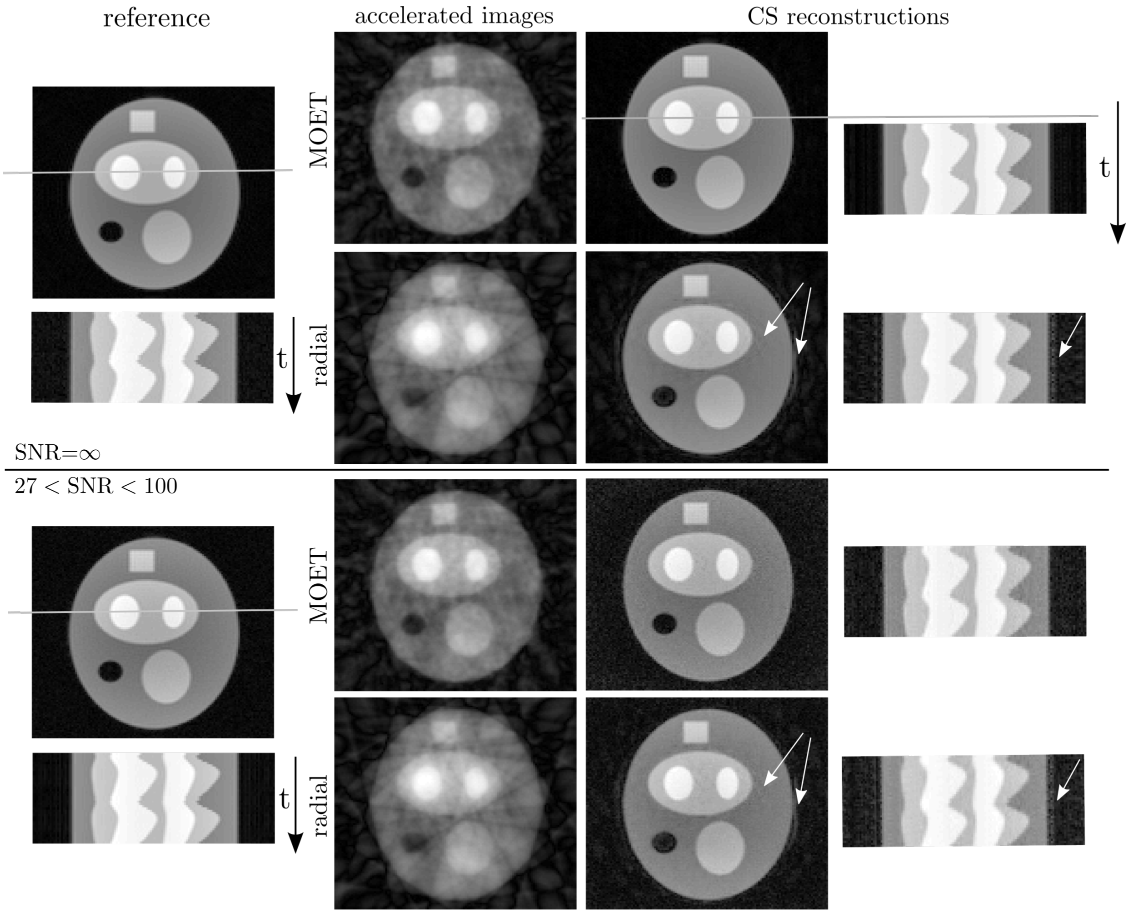

Figure 7.8: Compressed Sensing reconstructions of a periodically moving phantom with high sparsity in xf-space. Reconstructions were performed on radial and MOET undersampled data for infinite and realistic values of SNR. Radial images exhibit stronger residual artifacts in both cases.

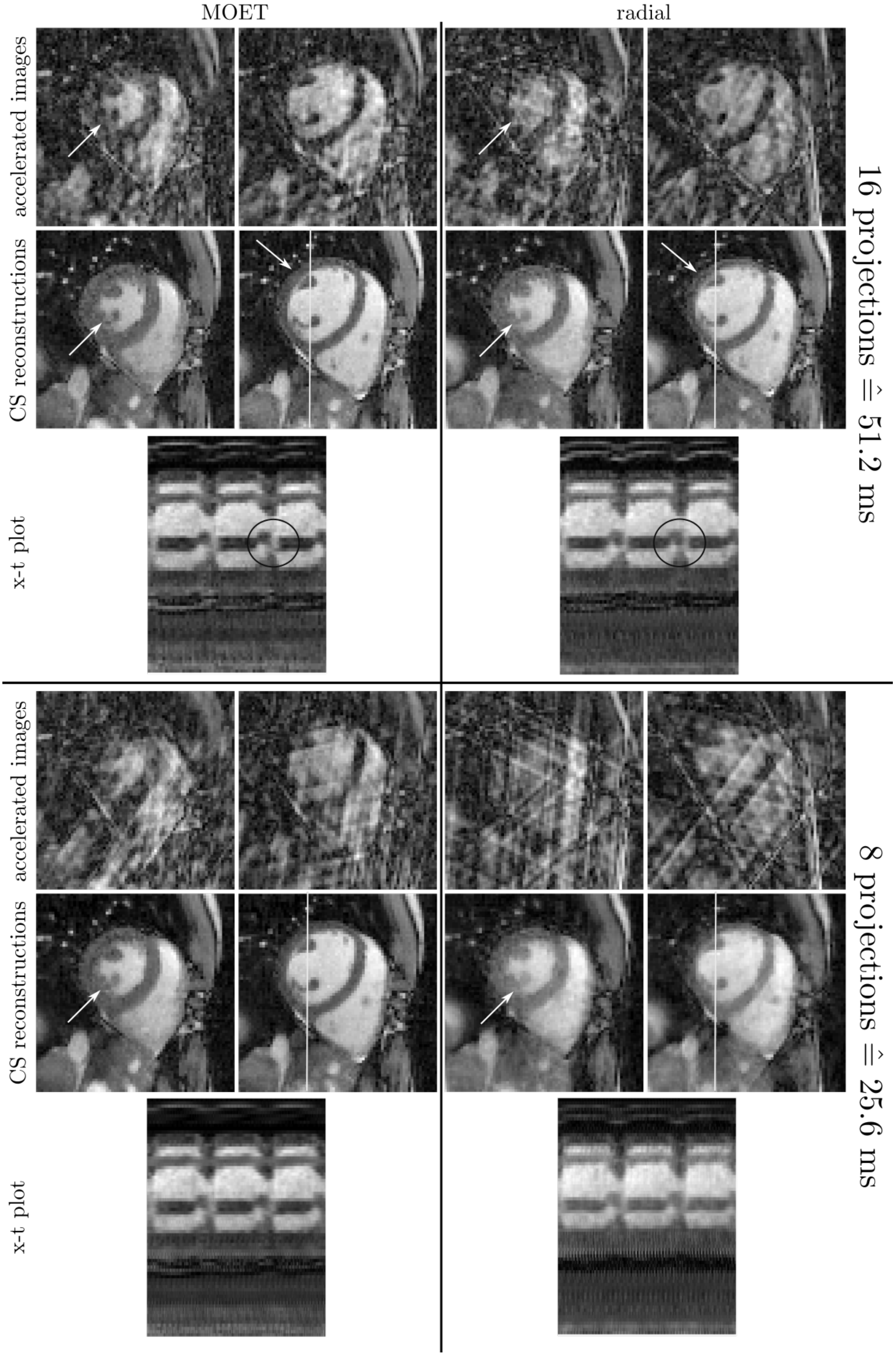

Figure 7.9: Undersampled cardiac images and CS reconstructions of both MOET and radial data using 16 and 8 projections per frame. The improved PSF of MOET sampling leads to less pronounced streaking artifacts when compared to the radial images. Reconstructions with MOET exhibit fewer residual artifacts and higher temporal accuracy.

data using both 8 (bottom) and 16 (top) projections per frame. For both levels of acceleration, the top row exhibits example aliased images for radial and MOET sampling in the diastole and the systole obtained by simple gridding reconstruction. Severe streaking artifacts are visible in radial undersampled images, while for MOET the aliasing artifacts are less pronounced. The corresponding CS reconstructions are shown below. For both acceleration factors, radial sampling leads to stronger residual aliasing artifacts after reconstruction, which can be observed in the individual frames as well as in the spatio-temporal xt-plot especially at indicated locations.

7.4 Discussion and Conclusion

In this chapter, a new sampling scheme for 2D MRI acquisitions was introduced, that leads to highly incoherent aliasing artifacts in undersampled images. Compressed sensing reconstructions were performed of both simulated and in-vivo MOET data and compared to corresponding reconstructions of radial data. Hereby, sparsity was exploited both directly in image space and in xf space for periodically moving objects (e.g. the beating heart).

Since MOET uses gradient waveforms of varying amplitude during acquisition, due to eddy currents and gradient delays it is not possible to predict the trajectory with sufficient accuracy. While gradient delays can be compensated for prospectively using for example the established method by Peters et. al. [98], this is not possible for the eddy current contributions. However, after correction of gradient delays the trajectory needs to be measured only once for each set of parameters which does not increase total acquisition time.

The advantage of MOET over radial sampling reconstructions is most apparent when used in compressed sensing reconstruction with a sparsity constraint directly in image space. Thanks to the high incoherence of MOET aliasing artifacts, even high acceleration factors lead to accurate results. In contrast, the streaking artifacts present in radial undersampled images hinder an accurate recovery even at lower acceleration factors. Besides the incoherency of the aliasing artifacts, another advantage of MOET sampling is the higher efficiency given by an increased coverage of k-space per unit time. For the example of a typical accelerated frame made up of 16 projections, MOET covers 15.9% of Cartesian k-space while for radial sampling this value decreases to 11.9%. This corresponds to nominal acceleration factors of R_M = 6.3 and R_M = 8.7 respectively.

Compressed sensing reconstructions were carried out on ungated cardiac radial and MOET data acquired during a breath hold to guarantee high sparsity in xf-space. A golden ratio projection reordering was implemented that permits the retrospective choice of different acceleration factors. Images were reconstructed from only 8 and 16 projections per frame corresponding to temporal resolutions of 25.6 ms and 51.2 ms. This type of sparsity constraint relies on high incoherency of the aliasing artifacts in xf-space instead of image space. Consequently, the advantage of MOET is smaller when compared to reconstructions expoiting direct image space sparsity, as the golden ratio projection reordering accounts for a large part of this incoherency. Nonetheless, the higher spatial incoherency leads to improved results with higher temporal accuracy and allows reconstructions with higher acceleration factors. Reconstructions with standard radial sampling exhibit more residual aliasing artifacts and slight temporal blurring. Differences in image quality are more obvious for higher acceleration factors.

While in this experiment a total of 4096 projections were acquired, this is no requirement for the compressed sensing reconstruction with sparsity constraint in xf-space. The reconstruction can be successfully performed even for a small number of cardiac cycles. Consequently, fewer projections can be acquired and both measurement time and duration of the breath hold can be reduced to less than 5 s, which is a small value compared to standard CINE acquisitions and may improve patient comfort.

While the MOET trajectory is effective for CS reconstructions, the implementation also poses some challenges. For each set of receiver bandwidth and FOV parameters, a separate trajectory measurement scan has to be performed once. This has to be done carefully, as errors in these trajectory measurements may lead to errors in the final reconstructed images. In this work, MOET was implemented using a bSSFP sequence to generate the typical contrast for dynamic cardiac imaging, but it is straightforward to implement MOET into any other sequence. Also, MOET can easily be extended for 3D imaging. Based on the simulations performed in this work, MOET is expected to be particular advantageous for applications with high sparsity in image space, such as angiography.

CHAPTER 8

Summary

Magnetic Resonance Imaging (MRI) is a non-invasive medical imaging technique, that is routinely used in clinical practice for detection and diagnosis of a wide range of different diseases. In MRI, no ionizing radiation is used, making even repeated application unproblematic. This is an important advantage over other common imaging methods such as X-rays and Computer Tomography. One major drawback of MRI, however, are long acquisition times and associated high costs of experiments. Since the introduction of MRI, several important technical developments have been made to successfully reduce acquisition times. In this work, novel approaches were developed to increase the efficiency of MRI acquisitions.

In Chapter 4, an improved radial turbo spin-echo (TSE) combined acquisition and reconstruction strategy was introduced. Cartesian turbo spin-echo sequences [3] are widely used especially for the detection and diagnosis of neurological pathologies, as they provide high SNR images with both clinically important proton density and T_2 contrasts. TSE acquisitions combined with radial sampling are very efficient, since it is possible to obtain a number of ETL images with different contrasts from a single radial TSE measurement [56–58]. Conventionally, images with a particular contrast are obtained from both radial and Cartesian TSE acquisitions by combining data from different echo times into a single image. In the radial case, this can be achieved by employing k-space weighted image contrast (KWIC) reconstruction. In KWIC, the center region of k-space is filled exclusively with data belonging to the desired contrast while outer regions also are assembled with data acquired at other echo times. However, this data sharing leads to mixed contrast contributions to both Cartesian and radial TSE images. This is true especially for proton density weighted images and therefore may reduce their diagnostic value.

In the proposed method, an adapted golden angle reordering scheme is introduced for radial TSE acquisitions, that allows a free choice of the echo train length and provides high flexibility in image reconstruction. Unwanted contrast contaminations are greatly reduced by employing a narrow-band KWIC filter, that restricts data sharing to a small temporal window around the desired echo time. This corresponds to using fewer data than required for fully sampled images and consequently leads to images exhibiting aliasing artifacts. In a second step, aliasing-free images are obtained using parallel imaging. In the neurological examples presented, the CG-SENSE algorithm [42] was chosen due to its stable convergence properties and its ability to reconstruct arbitrarily sampled data. In simulations as well as in different in vivo neurological applications, no unwanted contrast contributions could be observed in radial TSE images reconstructed with the proposed method. Since this novel approach is easy to implement on today's scanners and requires low computational power, it might be valuable for the clinical breakthrough of radial TSE acquisitions.

In Chapter 5, an auto-calibrating method was introduced to correct for stimulated echo contributions to T_2 estimates from a mono-exponential fit of multi spin-echo (MSE) data. Quantification of T_2 is a useful tool in clinical routine for the detection and diagnosis of diseases as well as for tissue characterization. Due to technical imperfections, refocusing flip angles in a MSE acquisition deviate from the ideal value of 180°. This gives rise to significant stimulated echo contributions to the overall signal evolution. Therefore, T_2 estimates obtained from MSE acquisitions typically are notably higher than the reference. To obtain accurate T_2 estimates from MSE acquisitions, MSE signal amplitudes can be predicted using the extended phase graph (EPG, [23, 24]) algorithm. Subsequently, a correction factor can be obtained from the simulated EPG T_2 value and applied to the MSE T_2 estimates. However, EPG calculations require knowledge about refocusing pulse amplitudes, T_2 and T_1 values and the temporal spacing of subsequent echoes. While the echo spacing is known and, as shown in simulations, an approximate T_1 value can be assumed for high ratios of T_1/T_2 without compromising accuracy of the results, the remaining two parameters are estimated from the data themselves. An estimate for the refocusing flip angle can be obtained from the signal intensity ratio of the second to the first echo using EPG. A conventional mono-exponential fit of the MSE data yields a first estimate for T_2. The T_2 correction is then obtained iteratively by updating the T_2 value used for EPG calculations in each step. For all examples presented, two iterations proved to be sufficient for convergence. In the proposed method, a mean flip angle is extracted across the slice. As shown in simulations, this assumption leads to greatly reduced deviations even for more inhomogeneous slice profiles. The accuracy of corrected T_2 values was shown in experiments using a phantom consisting of bottles filled with liquids with a wide range of different T_2 values. While T_2 MSE estimates were shown to deviate significantly from the spin-echo reference values, this is not the case for corrected T_2 values. Furthermore, applicability was demonstrated for in vivo neurological experiments.

In Chapter 6, a new auto-calibrating parallel imaging method called iterative GROG was presented for the reconstruction of non-Cartesian data. A wide range of different non-Cartesian schemes have been proposed for data acquisition in MRI, that present various advantages over conventional Cartesian sampling such as faster acquisitions, improved dynamic imaging and intrinsic motion correction. However, one drawback of non-Cartesian data is the more complicated reconstruction, which is ever more problematic for non-Cartesian parallel imaging techniques. Iterative GROG uses Calibrationless Parallel Imaging by Structured Low-Rank Matrix Completion (CPI) for data reconstruction. Since CPI requires points on a Cartesian grid, it cannot be used to directly reconstruct non-Cartesian data. Instead, Grappa Operator Gridding (GROG) is employed in a first step to move the non-Cartesian points to the nearest Cartesian grid locations. However, GROG requires a fully sampled center region of k-space for calibration. Combining both methods in an iterative scheme, accurate GROG weights can be obtained even from highly undersampled non-Cartesian data. Subsequently, CPI can be used to reconstruct either full k-space or a calibration area of arbitrary size, which can then be employed for data reconstruction with conventional parallel imaging methods.

In Chapter 7, a new 2D sampling scheme was introduced consisting of multiple oscillating efficient trajectories (MOET), that is optimized for Compressed Sensing (CS) reconstructions. For successful CS reconstruction of a particular data set, some requirements have to be met. First, every data sample has to carry information about the whole object, which is automatically fulfilled for the Fourier sampling employed in MRI. Additionally, the image to be reconstructed has to be sparse in an arbitrary domain, which is true for a number of different applications. Last, data sampling has to be performed in an incoherent fashion. For 2D imaging, this important requirement of CS is difficult to achieve with conventional Cartesian and non-Cartesian sampling schemes. Radial sampling is often used for CS reconstructions of dynamic data despite the streaking present in undersampled images. To obtain incoherent aliasing artifacts in undersampled images while at the same time preserving the advantages of radial sampling for dynamic imaging, MOET combines radial spokes with oscillating gradients of varying amplitude and alternating orientation orthogonal to the readout direction. The advantage of MOET over radial sampling in CS reconstructions was demonstrated in simulations and in in vivo cardiac imaging. MOET provides superior results especially when used in CS reconstructions with a sparsity constraint directly in image space. Here, accurate results could be obtained even from few MOET projections, while the coherent streaking artifacts present in the case of radial sampling prevent image recovery even for smaller acceleration factors. For CS reconstructions of dynamic data with sparsity constraint in xf-space, the advantage of MOET is smaller since the temporal reordering is responsible for an important part of incoherency. However, as was shown in simulations of a moving phantom and in the reconstruction of ungated cardiac data, the additional spatial incoherency provided by MOET still leads to improved results with higher accuracy and may allow reconstructions with higher acceleration factors.

CHAPTER 9

Zusammenfassung

Die Magnetresonanztomographie (MRT) ist ein wichtiges nicht-invasives medizinisches Bildgebungsverfahren, das im klinischen Alltag zur Entdeckung und Diagnose einer Vielzahl von Krankheiten verwendet wird. Im Gegensatz zu anderen Methoden wie Röntgen und Computertomographie kommt die MRT ohne den Einsatz ionisierender Strahlung aus, was selbst häufige Anwendungen ohne gesundheitliche Risiken erlaubt. Einer der größten Nachteile der MRT sind lange Messzeiten, die in Kombination mit der teuren Technik hohe Untersuchungskosten bedingen. Obwohl in der Vergangenheit durch die Entwicklung von sowohl verbesserter Hardware als auch neuen Rekonstruktionsverfahren bereits bedeutende Fortschritte in Bezug auf die Akquisitionsdauer erzielt werden konnten, ist eine weitere Beschleunigung nach wie vor ein wichtiges Forschungsgebiet im Bereich der MRT. Ziel dieser Arbeit war daher die Entwicklung neuer Ansätze zur Steigerung der Effizienz von MRT Experimenten.

In Kapitel 4 wurde eine kombinierte Akquisitions- und Rekonstruktionsstrategie für radiale Turbo Spin-Echo (TSE) Experimente vorgestellt. Im klinischen Alltag sind kartesische TSE Sequenzen zur Untersuchung diverser Krankheitsbilder weit verbreitet, da sie ein hohes SNR aufweisen und die Aufnahme der klinisch wichtigen Bilder mit Protonendichte- und T_2-Kontrast erlauben. Im Gegensatz zu kartesischem Abtasten, wo aus einem Datensatz lediglich ein Bild mit bestimmtem Kontrast erzeugt wird, sind radiale TSE Akquisitionen hocheffizient, da hier aus einem Datensatz mehrere Bilder mit verschiedenem Kontrast gewonnen werden können. In beiden Fällen wird in konventionellen Rekonstruktionsmethoden jedes Bild eines definierten Kontrasts durch das Zusammensetzen eines vollständig abgetasteten k-Raums mit Daten von verschiedenen Echozeiten erzeugt. Im radialen Fall geschieht dies durch die sogenannte "k-space weighted image contrast" (KWIC) Rekonstruktion. Hierbei wird das Zentrum des k-Raums ausschließlich mit zum gewünschten Kontrast gehörigen Daten gefüllt, während die äußeren Bereiche des k-Raums auch Daten von anderen Echozeiten enthalten. Obwohl der Kontrast von MRT Bildern hauptsächlich von den Daten im k-Raum Zentrum dominiert wird, führt die Kombination von Daten verschiedener Echozeiten in sowohl radialen als auch kartesischen TSE Bildern zu einem unerwünschten Mischkontrast. Dieser Effekt wird vor allem in protonendichtegewichteten Bildern sichtbar und kann somit deren diagnostischen Wert deutlich verringern.

Ein unerwünschter Mischkontrast kann verhindert werden, indem die Bandbreite des KWIC-Filters auf ein kleines zeitliches Fenster um die angestrebte Echozeit herum eingeschränkt wird. Um eine freie Wahl der Echozuglänge und hohe Flexibilität in der Bildrekonstruktion zu ermöglichen, wurde für die radiale TSE Akquisition ein angepasstes Abtastschema unter Verwendung des goldenen Winkels vorgestellt. Da bei einem KWIC-Filter mit reduzierter Bandbreite für jedes Bild weniger Daten zur Verfügung stehen als für einen voll abgetasteten k-Raum benötigt, weisen rekonstruierte Bildern Einfaltungsartefakte auf. Diese werden in einem zweiten Schritt durch die Anwendung paralleler Bildgebung beseitigt. In den gezeigten Beispielen wurde dazu der CG-SENSE Algorithmus verwendet, da er stabile Konvergenz aufweist und für die Rekonstruktion von Daten mit irregulären Abtastschema angewandt werden kann. Anschließend werden bestehende Korrelationen der Bilderserie zur Reduktion verbleibender Artefakte und zu einer Verbesserung des SNR ausgenutzt. Wie mittels Simulationen gezeigt und für neurologische Daten bestätigt, weisen radiale TSE Bilder, die mit dieser Methode rekonstruiert wurden, keinen sichtbaren Mischkontrast mehr auf. Die erreichte Bildqualität ist hierbar vergleichbar mit konventionellen Rekonstruktionsmethoden. Da die vorgestellte Rekonstruktion einfach auf heutigen Scannern implementiert werden kann und lediglich niedrige Rechenkapazitäten benötigt, könnte sie einen wichtigen Beitrag für den klinischen Durchbruch radialer TSE Akquisitionen darstellen.

In Kapitel 5 wurde eine selbstkalibrierende Methode zur Korrektur von aus Multi Spin-Echo (MSE) Bildern gewonnenen T_2 Karten vorgestellt. In der klinischen Anwendung spielt die Quantifizierung von T_2 unter anderem bei der Diagnose von Krankheiten sowie bei der Klassifizierung von Gewebe eine wichtige Rolle. Eine MSE Sequenz verwendet mehrere RF-Pulse, um ein einzelnes Spin-Echo wiederholt zu refokussieren. Idealerweise betragen die Flipwinkel der Refokussierungspulse hierbei exakt 180°, um einen exponentiellen Signalabfall zu erhalten. Aufgrund technischer Ungenauigkeiten weichen die Werte der Flipwinkel von Refokussierungspulsen jedoch grundsätzlich von 180° ab. Niedrigere Flipwinkel führen zu stimulierten Echos, die wesentlich zu den einzelnen Echoamplituden beitragen und den Signalabfall entlang des Echozugs deutlich verlängern können. Somit weisen auch T_2 Werte, die aus solchen Bilderserien berechnet werden, eine teilweise deutliche Erhöhung auf. Um exakte Werte zu erhalten, kann der MSE Signalverlauf mittels des "extended phase graph" (EPG) Algorithmus abgeschätzt und so ein Korrekturfaktor ermittelt werden. Hierzu müssen die Flipwinkel der Refokussierungspulse, T_1 und T_2 Werte sowie der zeitliche Abstand der Echos (ESP) bekannt sein. Wie in Simulationen gezeigt wurde, kann T_1 für hohe Werte des Quotienten T_1/T_2 abgeschätzt werden, ohne an Genauigkeit der T_2 Ergebnisse einzubüßen. Abschätzungen der verbleibenden benötigten Parameter können direkt aus den Daten selbst gewonnen werden. Während der Flipwinkel aus den Intensitäten der ersten beiden Echos berechnet wird, liefert ein mono-exponentieller Fit der MSE Bilderserie eine erste Näherung für T_2. Die Korrektur für die T_2 Werte kann anschließend aus den EPG Signalverläufen berechnet werden. Durch Aktualisierung von T_2 und erneuter Ausführung des EPG-

Algorithmus wird die Genauigkeit der Korrektur iterativ erhöht, wobei schon eine sehr geringe Zahl von Iterationen zu Konvergenz führt. Wie in Simulationen und in Phantomexperimenten für verschiedenste T_2-Werte gezeigt, weisen korrigierte T_2 Werte eine hohe Genauigkeit auf. Dies gilt auch für niedrigere nominelle Flipwinkel als 180° und ist somit von speziellem Interesse bei höheren Feldstärken B_0, wo Grenzwerte der spezifischen Absorptionsrate die Einstrahlung einer Vielzahl von RF-Pulsen hoher Amplitude verbietet.

In Kapitel 6 wurde iteratives GROG, eine neue selbstkalibrierende iterative parallele Bildgebungsmethode für die Rekonstruktion von nichtkartesischen Daten vorgestellt. Es sind eine Vielzahl nichtkartesischer Trajektorien für MRT Messungen bekannt, die zahlreiche Vorteile gegenüber kartesischer Bildgebung bieten. Dazu gehören unter anderem eine schnellere Akquisition, verbesserte dynamische Bildgebung sowie die Möglichkeit zur intrinischen Bewegungskorrektur. Ein Nachteil nichtkartesischer Daten jedoch ist eine aufwendigere Rekonstruktion, sowohl bei voll abgetasteten Datensätzen als insbesondere auch in der parallelen Bildgebung. Iteratives GROG verwendet Calibrationless Parallel Imaging by Structured Low-Rank Matrix Completion (CPI) zur Rekonstruktion fehlender Daten. Diese Methode benötigt Daten auf kartesischen Gitterpunkten und kann nicht direkt für nichtkartesische Experimente angewandt werden. Stattdessen werden die nichtkartesischen Daten zunächst mittels Grappa Operator Gridding (GROG) in einem ersten Schritt auf ein kartesisches Gitter verschoben. GROG basiert auf paralleler Bildgebung und benötigt einen voll abgetasteten Teil des k-Raums zur Kalibrierung. Erste Kalibrationsdaten können gewonnen werden, indem die nichtkartesischen Punkte ohne Änderung auf die nächsten kartesischen Gitterpunkte verschoben werden und eine CPI-Rekonstruktion eines zentralen k-Raum Bereichs durchgeführt wird. Anschließend wird GROG angewandt um exakte Werte der kartesischen Gitterpunkte zu erhalten und der Prozess wird iteriert. Nach Konvergenz können entweder Kalibrationsdaten gewünschter Größe für eine konventionelle parallele Bildgebungsmethode erzeugt oder artefaktfreie Bilder mit CPI rekonstruiert werden.

In Kapitel 7 wurde ein neues Abtastungsschema für die 2D Bildgebung vorgestellt, das aus Multiplen Oszillierenden Effizienten Trajektorien (MOET) besteht und optimierte Compressed Sensing (CS) Rekonstruktionen ermöglicht. Für eine erfolgreiche Anwendung von Compressed Sensing müssen einige Voraussetzungen erfüllt sein. Erstens muss jeder Datenpunkt Informationen über das ganze Objekt enthalten, was bei der MRT aufgrund der Datenakquisition im Fourier-Raum automatisch erfüllt ist. Weiterhin muss das gemessene Objekt in einer beliebigen Basis sparse sein. Dies ist für viele verschiedene Anwendungen in der MRT der Fall. Drittens muss für CS Rekonstruktionen die Datenakquisition im k-Raum einem inkohärenten Muster folgen. Diese wichtige Voraussetzung ist in der zweidimensionalen Bildgebung mit konventionellen kartesischen und nicht-kartesischen Abtastschemata nur schwer zu erreichen. Deshalb wird für CS Rekonstruktionen häufig eine radiale Trajektorie eingesetzt, trotz der kohärenten streaking-Artefakte in unterabgetasteten Bildern. MOET verwendet daher eine Kombination von radialen Projektionen zusammen mit oszillierenden Gradienten auf der zur Ausleserichtung orthogonalen Achse. So erhält man inkohärente Aliasing-Artefakte und bewahrt gleichzeitig die Vorteile der radialen Bildgebung für die dynamische MRT. Die Überlegenheit von MOET gegenüber radialer Bildgebung für CS Rekonstruktionen konnte in Simulationen sowie in der Herzbildgebung aufgezeigt werden. Dies gilt insbesondere für CS Rekonstruktionen direkt im Bildraum, wo MOET gute Resultate liefert während die kohärenten Artefakte bei radialer Bildgebung eine genaue Bildwiederherstellung verhindert. Bei Rekonstruktionen dynamischer Daten, wo Sparsität im xf-Raum ausgenutzt wird, ist der Vorteil von MOET weniger ausgeprägt, da hier bereits die zeitliche Anordnung der Projektionen einen wesentlichen Beitrag zur Charakteristik der Aliasingartefakte liefert. Wie in Simulationen und für die in vivo Herzbildgebung gezeigt werden konnte, erlaubt die zusätzliche räumliche Inkohärenz von MOET jedoch auch in diesem Fall eine höhere Genauigkeit sowie Rekonstruktionen von Daten höherer Beschleunigung.

A

Appendix

Parameters for the calculation of the correction factor r

In this appendix, the parameters for the calculation of the correction factor

$$r(T_2) = a + \frac{b}{T_2} + c \cdot T_2 \tag{A.1}$$

introduced in Chapter are listed for ETL = 24 and 32 and for clinically relevant range for refocusing flip angles and echo spacing. This correction factor connects T_2 estimates obtained from MSE acquisitions using a mono-exponential fit with their accurate values:

$$T_2 = r \cdot T_2^{MSE} \tag{A.2}$$

		Flipangle (°)								
	ESP (ms)	100	110	120	130	140	150	160	170	180
a	7-12	0.77	0.82	0.87	0.91	0.94	0.97	0.98	1.00	1.00
b	7	-2.38	-1.95	-1.54	-1.15	-0.79	-0.48	-0.22	-0.055	0.00
	8	-2.68	-2.22	-1.78	-1.35	-0.94	-0.57	-0.27	-0.067	0.00
	9	-2.96	-2.49	-2.02	-1.55	-1.09	-0.68	-0.32	-0.079	0.00
	10	-3.24	-2.75	-2.25	-1.75	-1.25	-0.78	-0.38	-0.092	0.00
	11	-3.50	-3.01	-2.49	-1.96	-1.42	-0.90	-0.43	-0.11	0.00
	12	-3.76	-3.26	-2.72	-2.17	-1.59	-1.01	-0.49	-0.12	0.00
		$10^{-4}\times$	$10^{-4}\times$	$10^{-5}\times$	$10^{-5}\times$	$10^{-5}\times$	$10^{-5}\times$	$10^{-6}\times$	$10^{-6}\times$	
c	7	-1.58	-1.08	-7.51	-5.12	-3.00	-1.64	-8.10	-1.56	0.00
	8	-1.29	-0.88	-6.12	-4.19	-2.47	-1.36	-6.79	-1.29	0.00
	9	-1.07	-0.72	-5.04	-3.48	-2.06	-1.15	-5.85	-1.09	0.00
	10	-0.88	-0.59	-4.17	-2.92	-1.75	-1.00	-5.13	-0.94	0.00
	11	-0.73	-0.49	-3.46	-2.47	-1.51	-0.88	-4.61	-0.83	0.00
	12	-0.60	-0.40	-2.87	-2.10	-1.32	-0.79	-4.22	-0.75	0.00

Table A.1: Fit parameters for an echo train length of 24

		Flipangle (°)								
	ESP (ms)	100	110	120	130	140	150	160	170	180
a	7-12	0.78	0.82	0.87	0.91	0.94	0.97	0.99	1.00	1.00
b	7	-2.52	-2.07	-1.63	-1.22	-0.84	-0.51	-0.24	-0.06	0.00
	8	-2.81	-2.34	-1.87	-1.42	-0.99	-0.60	-0.29	-0.07	0.00
	9	-3.09	-2.60	-2.10	-1.62	-1.14	-0.71	-0.34	-0.08	0.00
	10	-3.36	-2.86	-2.34	-1.82	-1.30	-0.81	-0.39	-0.102	0.00
	11	-3.61	-3.10	-2.57	-2.02	-1.47	-0.93	-0.45	-0.11	0.00
	12	-3.86	-3.35	-2.80	-2.23	-1.63	-1.04	-0.50	-0.12	0.00
		$10^{-5}\times$	$10^{-5}\times$	$10^{-5}\times$	$10^{-5}\times$	$10^{-6}\times$	$10^{-6}\times$	$10^{-6}\times$	$10^{-7}\times$	
c	7	-5.55	-3.77	-2.51	-1.62	-9.77	-5.21	-2.14	-3.89	0.00
	8	-3.86	-2.58	-1.71	-1.11	-6.82	-3.73	-1.56	-2.60	0.00
	9	-2.52	-1.64	-1.08	-0.72	-4.63	-2.69	-1.17	-1.72	0.00
	10	-1.42	-0.87	-0.57	-0.41	-2.96	-1.95	-8.87	-1.10	0.00
	11	-0.49	-0.23	-0.15	-0.16	-1.72	-1.46	-0.72	-0.69	0.00
	12	0.31	0.33	0.20	-0.04	-0.74	-1.09	-0.62	-0.42	0.00

Table A.2: Fit parameters for an echo train length of 32

Bibliography

[1] P. C. Lauterbur, “Image Formation by Induced Local Interactions: Examples Employing Nuclear Magnetic Resonance,” *Nature (London)*, vol. 242, pp. 190–191, 1973.

[2] J. Frahm, A. Haase, and D. Matthaei, “Rapid NMR imaging of dynamic processes using the FLASH technique.,” *Magnetic Resonance in Medicine*, vol. 3, no. 2, pp. 321–327, 1986.

[3] J. Hennig, A. Nauerth, and H. Friedburg, “RARE imaging: a fast imaging method for clinical MR.,” *Magnetic Resonance in Medicine*, vol. 3, no. 6, pp. 823–833, 1986.

[4] D. K. Sodickson and W. J. Manning, “Simultaneous acquisition of spatial harmonics (SMASH): Fast imaging with radiofrequency coil arrays,” *Magnetic Resonance in Medicine*, vol. 38, no. 4, pp. 591–603, 1997.

[5] M. A. Griswold, P. M. Jakob, R. M. Heidemann, M. Nittka, V. Jellus, J. Wang, B. Kiefer, and A. Haase, “Generalized autocalibrating partially parallel acquisitions (GRAPPA).,” *Magnetic Resonance in Medicine*, vol. 47, no. 6, pp. 1202–1210, 2002.

[6] K. P. Pruessmann, M. Weiger, M. B. Scheidegger, and P. Boesiger, “SENSE: sensitivity encoding for fast MRI.,” *Magnetic Resonance in Medicine*, vol. 42, no. 5, pp. 952–962, 1999.

[7] M. Lustig, D. Donoho, and J. M. Pauly, “Sparse MRI: The application of compressed sensing for rapid MR imaging.,” *Magnetic Resonance in Medicine*, vol. 58, no. 6, pp. 1182–1195, 2007.

[8] E. M. Haacke, R. W. Brown, M. R. Thompson, and R. Venkatesan, *Magnetic Resonance Imaging: Physical Principles and Sequence Design*. John Wiley & Sons Inc, 1999.

[9] M. A. Bernstein, K. F. King, and X. J. Zhou, *Handbook of MRI Pulse Sequences*. Academic Press, 2004.

[10] C. Cohen-Tannoudji, B. Diu, F. Laloe, and B. Dui, *Quantum Mechanics (2 vol. set)*. Wiley-Interscience, 2006.

[11] P. R. Moran, "A flow velocity zeugmatographic interlace for NMR imaging in humans," *Magnetic Resonance Imaging*, vol. 1, no. 4, pp. 197–203, 1982.

[12] J. Pauly, D. Nishimura, and A. Macovski, "A k-space analysis of small-tip-angle excitation," *Journal of Magnetic Resonance 1969*, vol. 81, no. 1, pp. 43–56, 1989.

[13] P. M. Joseph, L. Axel, and M. O'Donnell, "Potential problems with selective pulses in NMR imaging systems.," *Medical Physics*, vol. 11, no. 6, pp. 772–777, 1983.

[14] J. Pauly, P. Le Roux, D. Nishimura, and A. Macovski, "Parameter relations for the Shinnar-Le Roux selective excitation pulse design algorithm," *IEEE Trans Med Imaging*, vol. 10, no. 1, pp. 53–65, 1991.

[15] E. L. Hahn, "Spin Echoes," *Physical Review*, vol. 80, no. 4, pp. 580–594, 1950.

[16] A. Oppert, "FISP: a new fast MRI sequence," *Electromedia*, vol. 54, pp. 15–18, 1986.

[17] J. L. Duerk, J. S. Lewin, M. Wendt, and C. Petersilge, "Remember true FISP? A high SNR, near 1-second imaging method for T2-like contrast in interventional MRI at .2 T.," *Journal of Magnetic Resonance Imaging*, vol. 8, no. 1, pp. 203–208, 1998.

[18] R. R. Edelman, P. Wielopolski, and F. Schmitt, "Echo-planar MR imaging.," *Radiology*, vol. 198, no. 3, pp. 585–586, 1994.

[19] A. P. Crawley, M. L. Wood, and R. M. Henkelman, "Elimination of transverse coherences in FLASH MRI," *Magnetic Resonance in Medicine*, vol. 8, no. 3, pp. 248–260, 1988.

[20] Y. Zur, M. L. Wood, and L. J. Neuringer, "Spoiling of transverse magnetization in steady-state sequences.," *Magnetic Resonance in Medicine*, vol. 21, no. 2, pp. 251–263, 1991.

[21] J. H. Duyn, "Steady state effects in fast gradient echo magnetic resonance imaging.," *Magnetic Resonance in Medicine*, vol. 37, no. 4, pp. 559–568, 1997.

[22] O. Bieri and K. Scheffler, "Fundamentals of balanced steady state free precession MRI.," *Journal of Magnetic Resonance Imaging*, vol. 000, 2013.

[23] J. Hennig, "Echoes–how to generate, recognize, use or avoid them in MR-imaging sequences. Part I: Fundamental and not so fundamental properties of spin echoes," *Concepts In Magnetic Resonance*, vol. 3, no. 3, pp. 125–143, 1991.

[24] J. Hennig, "Echoes–how to generate, recognize, use or avoid them in MR-imaging sequences. Part II: Echoes in imaging sequences," *Concepts In Magnetic Resonance*, vol. 3, no. 4, pp. 179–192, 1991.

[25] H. Y. Carr and E. M. Purcell, "Effects of Diffusion on Free Precession in Nuclear Magnetic Resonance Experiments," *Physical Review*, vol. 94, no. 3, pp. 630–638, 1954.

[26] S. Meiboom and D. Gill, "Modified Spin-Echo Method for Measuring Nuclear Relaxation Times," *Review of Scientific Instruments*, vol. 29, no. 8, p. 688, 1958.

[27] C. H. Meyer, B. S. Hu, D. G. Nishimura, and A. Macovski, "Fast spiral coronary artery imaging.," *Magnetic Resonance in Medicine*, vol. 28, no. 2, pp. 202–213, 1992.

[28] D. C. Noll, J. D. Cohen, C. H. Meyer, and W. Schneider, "Spiral K-space MR imaging of cortical activation.," *Journal of Magnetic Resonance Imaging*, vol. 5, no. 1, pp. 49–56, 1995.

[29] J. G. Pipe, "Motion correction with PROPELLER MRI: Application to head motion and free-breathing cardiac imaging," *Magnetic Resonance in Medicine*, vol. 42, no. 5, pp. 963–969, 1999.

[30] G. H. Glover and J. M. Pauly, "Projection reconstruction techniques for reduction of motion effects in MRI.," *Magnetic Resonance in Medicine*, vol. 28, no. 2, pp. 275–289, 1992.

[31] D. G. Nishimura, J. I. Jackson, and J. M. Pauly, "On the nature and reduction of the displacement artifact in flow images.," *Magnetic Resonance in Medicine*, vol. 22, no. 2, pp. 481–492, 1991.

[32] S. Winkelmann, T. Schaeffter, T. Koehler, H. Eggers, and O. Doessel, "An Optimal Radial Profile Order Based on the Golden Ratio for Time-Resolved MRI," *IEEE Transactions on Medical Imaging*, vol. 26, no. 1, pp. 68–76, 2007.

[33] J. A. Fessler, "On NUFFT-based gridding for non-Cartesian MRI.," *Journal of Magnetic Resonance*, vol. 188, no. 2, pp. 191–195, 2007.

[34] N. Seiberlich, M. Griswold, P. Jakob, F. Breuer, M. Blaimer, and R. Heidemann, "Pseudo-Cartesian GRAPPA Reconstruction of Undersampled Non-Cartesian Data," in *Proceedings 14th Scientific Meeting International Society for Magnetic Resonance in Medicine*, p. 2463, 2006.

[35] J. I. Jackson, C. H. Meyer, D. G. Nishimura, and A. Macovski, "Selection of a convolution function for Fourier inversion using gridding [computerised tomography application].," *IEEE Transactions on Medical Imaging*, vol. 10, no. 3, pp. 473–478, 1991.

[36] G. Voronoi, "Nouvelles applications des parametres continus a la theorie des formes quadratiques. Premier memoire. Sur quelques propietes des formes quatratiques positives parfaites.," *Journal fuer die reine und angewandte Mathematik*, vol. 133, pp. 97–178, 1908.

[37] J. G. Pipe and P. Menon, "Sampling density compensation in MRI: rationale and an iterative numerical solution.," *Magnetic Resonance in Medicine*, vol. 41, no. 1, pp. 179–186, 1999.

[38] M. Bydder, A. A. Samsonov, and J. Du, "Evaluation of optimal density weighting for regridding," *Magnetic resonance imaging*, vol. 25, no. 5, pp. 695–702, 2007.

[39] P. B. Roemer, W. A. Edelstein, C. E. Hayes, S. P. Souza, and O. M. Mueller, "The NMR phased array.," *Magnetic Resonance in Medicine*, vol. 16, no. 2, pp. 192–225, 1990.

[40] J. W. Carlson, "An algorithm for NMR imaging reconstruction based on multiple Rf receiver coils," *Journal of Magnetic Resonance*, vol. 74, pp. 376–380, 1987.

[41] M. Hutchinson and U. Raff, "Fast MRI data acquisition using multiple detectors.," *Magnetic Resonance in Medicine*, vol. 6, no. 1, pp. 87–91, 1988.

[42] K. P. Pruessmann, M. Weiger, P. Börnert, and P. Boesiger, “Advances in sensitivity encoding with arbitrary k-space trajectories,” *Magnetic Resonance in Medicine*, vol. 46, no. 4, pp. 638–651, 2001.

[43] P. M. Jakob, M. A. Griswold, R. R. Edelman, and D. K. Sodickson, “AUTO-SMASH : A self-calibrating technique for SMASH imaging,” *Magnetic Resonance Materials In Physics Biology And Medicine*, vol. 7, no. 1, pp. 42–54, 1998.

[44] R. M. Heidemann, M. A. Griswold, A. Haase, and P. M. Jakob, “VD-AUTO-SMASH imaging.,” *Magnetic Resonance in Medicine*, vol. 45, no. 6, pp. 1066–1074, 2001.

[45] M. Bydder, D. J. Larkman, and J. V. Hajnal, “Generalized SMASH imaging.,” *Magnetic Resonance in Medicine*, vol. 47, no. 1, pp. 160–170, 2002.

[46] R. M. Heidemann, O. Ozsarlak, P. M. Parizel, J. Michiels, B. Kiefer, V. Jellus, M. Müller, F. Breuer, M. Blaimer, M. A. Griswold, and P. M. Jakob, “A brief review of parallel magnetic resonance imaging.,” *European Radiology*, vol. 13, no. 10, pp. 2323–2337, 2003.

[47] M. Blaimer, F. Breuer, M. Mueller, R. Heidemann, M. Griswold, and P. Jakob, “SMASH, SENSE, PILS, GRAPPA: how to choose the optimal method,” *Topics in magnetic resonance imaging TMRI*, vol. 15, no. 4, pp. 223–236, 2004.

[48] D. Larkman and R. Nunes, “Parallel magnetic resonance imaging,” *Physics in Medicine and Biology*, vol. 52, no. 7, pp. R15–55, 2007.

[49] J. R. Shewchuk, “An Introduction to the Conjugate Gradient Method Without the Agonizing Pain,” *Science*, vol. 49, no. CS-94-125, p. 64, 1994.

[50] D. L. Donoho, “Compressed sensing,” *IEEE Transactions on Information Theory*, vol. 52, pp. 1289–1306, Apr. 2006.

[51] E. J. Candes, J. Romberg, and T. Tao, “Robust uncertainty principles: exact signal reconstruction from highly incomplete frequency information,” *IEEE Transactions on Information Theory*, vol. 52, no. 2, pp. 489–509, 2006.

[52] L. Rudin, S. Osher, and E. Fatemi, “Nonlinear total variation based noise removal algorithms,” *Physica D: Nonlinear Phenomena*, vol. 60, no. 1-4, pp. 259–268, 1992.

[53] A. S. Stern, D. L. Donoho, and J. C. Hoch, “NMR data processing using iterative thresholding and minimum l(1)-norm reconstruction.,” *Journal of Magnetic Resonance*, vol. 188, no. 2, pp. 295–300, 2007.

[54] S. S. Chen, D. L. Donoho, and M. A. Saunders, “Atomic Decomposition by Basis Pursuit,” *SIAM Journal on Scientific Computing*, vol. 20, no. 1, pp. 33–61, 1998.

[55] M. Lustig, *Sparse MRI.* PhD thesis, Stanford University, 2008.

[56] M. I. Altbach, E. K. Outwater, T. P. Trouard, E. A. Krupinski, R. J. Theilmann, A. T. Stopeck, M. Kono, and A. F. Gmitro, “Radial fast spin-echo method for T2-weighted imaging and T2 mapping of the liver.,” *Journal of Magnetic Resonance Imaging*, vol. 16, no. 2, pp. 179–189, 2002.

[57] V. Rasche, D. Holz, and W. Schepper, “Radial turbo spin echo imaging.,” *Magnetic Resonance in Medicine*, vol. 32, no. 5, pp. 629–638, 1994.

[58] M. I. Altbach, A. Bilgin, Z. Li, E. W. Clarkson, T. P. Trouard, and A. F. Gmitro, “Processing of radial fast spin-echo data for obtaining T2 estimates from a single k-space data set.,” *Magnetic Resonance in Medicine*, vol. 54, no. 3, pp. 549–559, 2005.

[59] K. T. Block, M. Uecker, and J. Frahm, “Model-based iterative reconstruction for radial fast spin-echo MRI.,” *IEEE Transactions on Medical Imaging*, vol. 28, no. 11, pp. 1759–1769, 2009.

[60] H. K. Song and L. Dougherty, “k-space weighted image contrast (KWIC) for contrast manipulation in projection reconstruction MRI.,” *Magnetic Resonance in Medicine*, vol. 44, no. 6, pp. 825–832, 2000.

[61] “http://www.bic.mni.mcgill.ca/brainweb/.”

[62] R. K. Kwan, A. C. Evans, and G. B. Pike, “MRI simulation-based evaluation of image-processing and classification methods.,” *IEEE Transactions on Medical Imaging*, vol. 18, no. 11, pp. 1085–1097, 1999.

[63] D. L. Collins, A. P. Zijdenbos, V. Kollokian, J. G. Sled, N. J. Kabani, C. J. Holmes, and A. C. Evans, “Design and construction of a realistic digital brain phantom,” *IEEE Transactions on Medical Imaging*, vol. 17, no. 3, pp. 463–468, 1998.

[64] J. J. Van Vaals, M. E. Brummer, W. T. Dixon, H. H. Tuithof, H. Engels, R. C. Nelson, B. M. Gerety, J. L. Chezmar, and J. A. Den Boer, “"Keyhole" method for accelerating imaging of contrast agent uptake.,” *Journal of Magnetic Resonance Imaging*, vol. 3, no. 4, pp. 671–675, 1993.

[65] R. J. Theilmann, A. F. Gmitro, M. I. Altbach, and T. P. Trouard, “View-ordering in radial fast spin-echo imaging.,” *Magnetic Resonance in Medicine*, vol. 51, no. 4, pp. 768–774, 2004.

[66] M. Voelker, P. Ehses, B. Martin, F. Breuer, and P. M. Jakob, “High resolution T2 weighted Lung Imaging with a radial Turbo Spin-Echo Sequence,” in *Proc. Intl. Soc. Mag. Reson. Med. 18*, p. 2509, 2010.

[67] D. O. Walsh, A. F. Gmitro, and M. W. Marcellin, “Adaptive reconstruction of phased array MR imagery.,” *Magnetic Resonance in Medicine*, vol. 43, no. 5, pp. 682–690, 2000.

[68] J. A. Fessler, “http://web.eecs.umich.edu/˜fessler/code/.”

[69] P. M. Robson, A. K. Grant, A. J. Madhuranthakam, R. Lattanzi, D. K. Sodickson, and C. A. McKenzie, “Comprehensive quantification of signal-to-noise ratio and g-factor for image-based and k-space-based parallel imaging reconstructions.,” *Magnetic Resonance in Medicine*, vol. 60, no. 4, pp. 895–907, 2008.

[70] M. Buehrer, K. P. Pruessmann, P. Boesiger, and S. Kozerke, “Array compression for MRI with large coil arrays.,” *Magnetic Resonance in Medicine*, vol. 57, no. 6, pp. 1131–1139, 2007.

[71] F. A. Breuer, M. F. Mueller, R. M. Heidemann, M. A. Griswold, and P. M. Jakob, "The use of principal component analysis (PCA) for estimation of the maximum reduction factor in 2D parallel imaging," in *Proceedings 13th Scientific Meeting International Society for Magnetic Resonance in Medicine*, p. 2668, 2005.

[72] M. S. Hansen and T. S. Sø rensen, "Gadgetron: an open source framework for medical image reconstruction.," *Magnetic Resonance in Medicine*, vol. 69, no. 6, pp. 1768–76, 2013.

[73] B. J. Dardzinski, T. J. Mosher, S. Li, M. A. Van Slyke, and M. B. Smith, "Spatial variation of T2 in human articular cartilage.," *Radiology*, vol. 205, no. 2, pp. 546–550, 1997.

[74] S. W. Farraher, H. Jara, K. J. Chang, A. Ozonoff, and J. A. Soto, "Differentiation of hepatocellular carcinoma and hepatic metastasis from cysts and hemangiomas with calculated T2 relaxation times and the T1/T2 relaxation times ratio.," *Journal of Magnetic Resonance Imaging*, vol. 24, no. 6, pp. 1333–1341, 2006.

[75] T. Kurki, N. Lundbom, and S. Valtonen, "Tissue characterisation of intracranial tumours: the value of magnetisation transfer and conventional MRI.," *Neuroradiology*, vol. 37, no. 7, pp. 515–521, 1995.

[76] A. MacKay, C. Laule, I. Vavasour, T. Bjarnason, S. Kolind, and B. Mädler, "Insights into brain microstructure from the T2 distribution.," *Magnetic resonance imaging*, vol. 24, no. 4, pp. 515–525, 2006.

[77] F. J. Rugg-Gunn, P. A. Boulby, M. R. Symms, G. J. Barker, and J. S. Duncan, "Whole-brain T2 mapping demonstrates occult abnormalities in focal epilepsy.," *Neurology*, vol. 64, no. 2, pp. 318–325, 2005.

[78] K. P. Whittall, A. L. MacKay, D. A. Graeb, R. A. Nugent, D. K. Li, and D. W. Paty, "In vivo measurement of T2 distributions and water contents in normal human brain.," *Magnetic Resonance in Medicine*, vol. 37, no. 1, pp. 34–43, 1997.

[79] M. Weigel, S. Schwenk, V. G. Kiselev, K. Scheffler, and J. Hennig, "Extended phase graphs with anisotropic diffusion.," *Journal of Magnetic Resonance*, vol. 205, no. 2, pp. 276–285, 2010.

[80] R. M. Lebel and A. H. Wilman, "Transverse relaxometry with stimulated echo compensation.," *Magnetic Resonance in Medicine*, vol. 64, no. 4, pp. 1005–1014, 2010.

[81] R. Deichmann and A. Haase, "Quantification of T1 values by SNAPSHOT-FLASH NMR Imaging," *Journal of Magnetic Resonance*, vol. 96, pp. 608–612, 1992.

[82] K. Heberlein and X. Hu, "Auto-calibrated parallel spiral imaging.," *Magnetic Resonance in Medicine*, vol. 55, no. 3, pp. 619–625, 2006.

[83] R. M. Heidemann, M. A. Griswold, N. Seiberlich, G. Krüger, S. A. R. Kannengiesser, B. Kiefer, G. Wiggins, L. L. Wald, and P. M. Jakob, "Direct parallel image reconstructions for spiral trajectories using GRAPPA.," *Magnetic Resonance in Medicine*, vol. 56, no. 2, pp. 317–326, 2006.

[84] M. A. Griswold, R. Heidemann, and P. M. Jakob, “Direct parallel imaging reconstruction of radially sampled data using grappa with relative shifts,” in *Proc. Intl. Soc. Mag. Reson. Med. 11*, p. 2509, 2003.

[85] F. A. Breuer, H. Moriguchi, N. Seiberlich, M. Blaimer, P. M. Jakob, J. L. Duerk, and M. A. Griswold, “Zigzag sampling for improved parallel imaging.,” *Magnetic Resonance in Medicine*, vol. 60, no. 2, pp. 474–478, 2008.

[86] N. Seiberlich, F. Breuer, R. Heidemann, M. Blaimer, M. Griswold, and P. Jakob, “Reconstruction of undersampled non-Cartesian data sets using pseudo-Cartesian GRAPPA in conjunction with GROG.,” *Magnetic Resonance in Medicine*, vol. 59, no. 5, pp. 1127–1137, 2008.

[87] M. Lustig, M. Elad, and P. J. M, “Calibrationless Parallel Imaging Reconstruction by Structured Low-Rank Matrix Completion,” in *Proc. Intl. Soc. Mag. Reson. Med. 18*, p. 2870, 2010.

[88] P. J. Shin, P. E. Z. Larson, M. a. Ohliger, M. Elad, J. M. Pauly, D. B. Vigneron, and M. Lustig, “Calibrationless parallel imaging reconstruction based on structured low-rank matrix completion,” *Magnetic Resonance in Medicine*, p. doi:10.1002/mrm.24997, 2013.

[89] N. Seiberlich, F. A. Breuer, M. Blaimer, K. Barkauskas, P. M. Jakob, and M. A. Griswold, “Non-Cartesian data reconstruction using GRAPPA operator gridding (GROG).,” *Magnetic Resonance in Medicine*, vol. 58, no. 6, pp. 1257–1265, 2007.

[90] D. Achlioptas and F. Mcsherry, “Fast computation of low-rank matrix approximations,” *Journal of the ACM*, vol. 54, no. 2, pp. 9–es, 2007.

[91] D. L. Donoho, M. Lustig, and J. M. Pauly, “Rapid MR Imaging with "Compressed Sensing" and Randomly Under-Sampled 3 DFT Trajectories,” in *Proc 14th Ann Meeting ISMRM*, p. 695, Citeseer, 2006.

[92] M. Lustig, J. M. Santos, D. L. Donoho, and J. M. Pauly, “k-t SPARSE : High frame rate dynamic MRI exploiting spatio-temporal sparsity,” *Methods*, vol. 50, no. 5, pp. 2003–2003, 2003.

[93] M. Seeger, H. Nickisch, R. Pohmann, and B. Schölkopf, “Optimization of k-Space Trajectories by Bayesian Experimental Design,” *Methods*, p. 2627, 2009.

[94] J. C. Ye, S. Tak, Y. Han, and H. W. Park, “Projection reconstruction MR imaging using FOCUSS.,” *Magnetic Resonance in Medicine*, vol. 57, no. 4, pp. 764–775, 2007.

[95] R. W. Chan, E. A. Ramsay, E. Y. Cheung, and D. B. Plewes, “The influence of radial undersampling schemes on compressed sensing reconstruction in breast MRI.,” *Magnetic Resonance in Medicine*, vol. 000, no. 2, pp. 1–15, 2011.

[96] O. Bieri, M. Markl, and K. Scheffler, “Analysis and compensation of eddy currents in balanced SSFP.,” *Magnetic Resonance in Medicine*, vol. 54, no. 1, pp. 129–137, 2005.

[97] J. H. Duyn, Y. Yang, J. A. Frank, and J. W. Van Der Veen, “Simple correction method for k-space trajectory deviations in MRI.,” *Journal of Magnetic Resonance*, vol. 132, no. 1, pp. 150–153, 1998.

[98] D. C. Peters, J. A. Derbyshire, and E. R. McVeigh, “Centering the projection reconstruction trajectory: reducing gradient delay errors.,” *Magnetic Resonance in Medicine*, vol. 50, no. 1, pp. 1–6, 2003.

List of Publications

1. **Neumann D.**, Blaimer M., Jakob, P.M., Felix F.A. *Simple Recipe for Accurate T2 Quantification with Multi Spin-Echo Acquisitions*. Magnetic Resonance Materials in Physics, Biology and Medicine 2014; Submitted for Publication.
2. **Neumann D.**, Breuer F.A., Völker M., Brandt T., Griswold, M.A., Jakob, P.M., Blaimer M. *Reducing Contrast Contamination in Radial Turbo Spin-Echo Acquisitions by Combining a Narrow-Band KWIC Filter With Parallel Imaging*. Magnetic Resonance in Medicine 2014; doi:10.1002/mrm.25081.
3. Okanovic M., Völker M., **Neumann D.**, Blaimer M., Breuer F.A., Jakob P.M. *Neuroimaging with reduced RF power using a radial hybrid sequence*. Proceedings 30th Scientific Meeting European Society for Magnetic Resonance in Medicine and Biology 2013;409.
4. **Neumann D.**, Breuer F.A., Jakob P.M., Griswold M.A. *Improved Compressed Sensing Reconstructions with MOET*. Proceedings 21st Scientific Meeting International Society for Magnetic Resonance in Medicine 2013;3710.
5. **Neumann D.**, Seiberlich N., Breuer F.A., Lee G., Ehses P., Duerk J.L., Jakob P.M., Griswold M.A. *MOET: Multiple Oscillating Efficient Trajectories*. Proceedings 20th Scientific Meeting International Society for Magnetic Resonance in Medicine 2012;2263.
6. Riffe M.J., **Neumann D.**, Blumenthal C., Lee G., Seiberlich N., Griswold M.A. *Wireless Magnetic Field Monitoring*. Proceedings 20th Scientific Meeting International Society for Magnetic Resonance in Medicine 2012;2749.
7. Basse-Lüsebrink T.C., Kampf T., Fischer A., Sturm V.J.F., **Neumann D.**, Köstler H., Hahn D., Stoll G., Jakob P.M. *SAR-reduced spin-echo-based Bloch-Siegert* B_1^+ *mapping: BS-SE-BURST*. Magnetic Resonance in Medicine 2012;68(2):529-536.

8. **Neumann D.**, Breuer F.A., Jakob P.M., Lee G., Griswold M.A., Seiberlich N. *Reconstructing Undersampled Non-Cartesian Data with Calibrationless Parallel Imaging*. Proceedings 19th Scientific Meeting International Society for Magnetic Resonance in Medicine 2011;2888.
9. Breuer F.A., Fischer A., Seiberlich N., Ehses P., Blaimer M., **Neumann D.**, Jakob P.M., Griswold M.A. *Improved Compressed Sensing reconstruction in dynamic contrast enhanced MR Angiography by means of Principal Component Analysis (PCA)*. Proceedings 19th Scientific Meeting International Society for Magnetic Resonance in Medicine 2011;4379.
10. **Neumann D.**, Choli M., Blaimer M., Bock M., Breuer F.A., Jakob P.M. *Reduced SAR with BASE Sequence at 7 Tesla*. Proceedings 18th Scientific Meeting International Society for Magnetic Resonance in Medicine 2010;2888.
11. Choli M., Breuer F.A., **Neumann D.**, Bock M., Hillenbrand C.M., Loeffler R.B., Jakob P.M. *Reduced SAR with Combined Acquisition Technique (CAT) Hybrid Imaging Sequence at 7 Tesla*. Proceedings 18th Scientific Meeting International Society for Magnetic Resonance in Medicine 2010;3030.

DANKSAGUNG

An dieser Stelle möchte ich allen Personen meinen Dank aussprechen, die zum erfolgreichen Abschluss meiner Promotion beigetragen haben:

- meinem Doktorvater Prof. Peter Jakob für die Möglichkeit, an seinem Lehrstuhl zu promovieren und für die ausgezeichnete Betreuung und Unterstützung
- Felix Breuer und Martin Blaimer für die tolle Zusammenarbeit und umfangreiche Hilfe
- Mark Griswold für die Möglichkeit, ein sehr schönes und ereignisreiches Jahr in Cleveland zu verbringen und für die Unterstützung und gute Zusammenarbeit
- Nicole Seiberlich und Vikas Gulani für die Gastfreundschaft und Hilfe während meines Aufenthaltes in Cleveland
- den weiteren Keller-Büro-Kollegen Matthew Riffe, Gregory Lee, Karan Dara, Anagha Deshmane, Lisa Bauer, Katie Wright und Dan Ma
- meiner Frau Paola Ponce, meinen Eltern und meinen Geschwistern, die mir immer ein großer Rückhalt waren und sind
- meiner Gelegenheits-Taxi-Fahrerin Sabine Voll, die mich treffsicher immer an der steilsten Stelle aufgesammelt hat
- unserem Hochzeits-DJ Ebi Munz
- Philipp Ehses und Morwan Choli
- dem Korrektur-Leser Thomas Benkert
- meinen langjährigen Bürokollegen aus B036: Fabian Gutjahr, Patrick Vogel, Kathrin Hemberger und Gunthart Lykowski
- dem all-wöchentlichen Mensa-Team Stefan Rützl, Christoph Stolzenberger und Martin Kullmann
- dem Tischfußball-Team
- allen meinen Freunden
- der ganzen EP5 und dem MRB für die schöne gemeinsame Zeit

11. FEBRUAR 2014